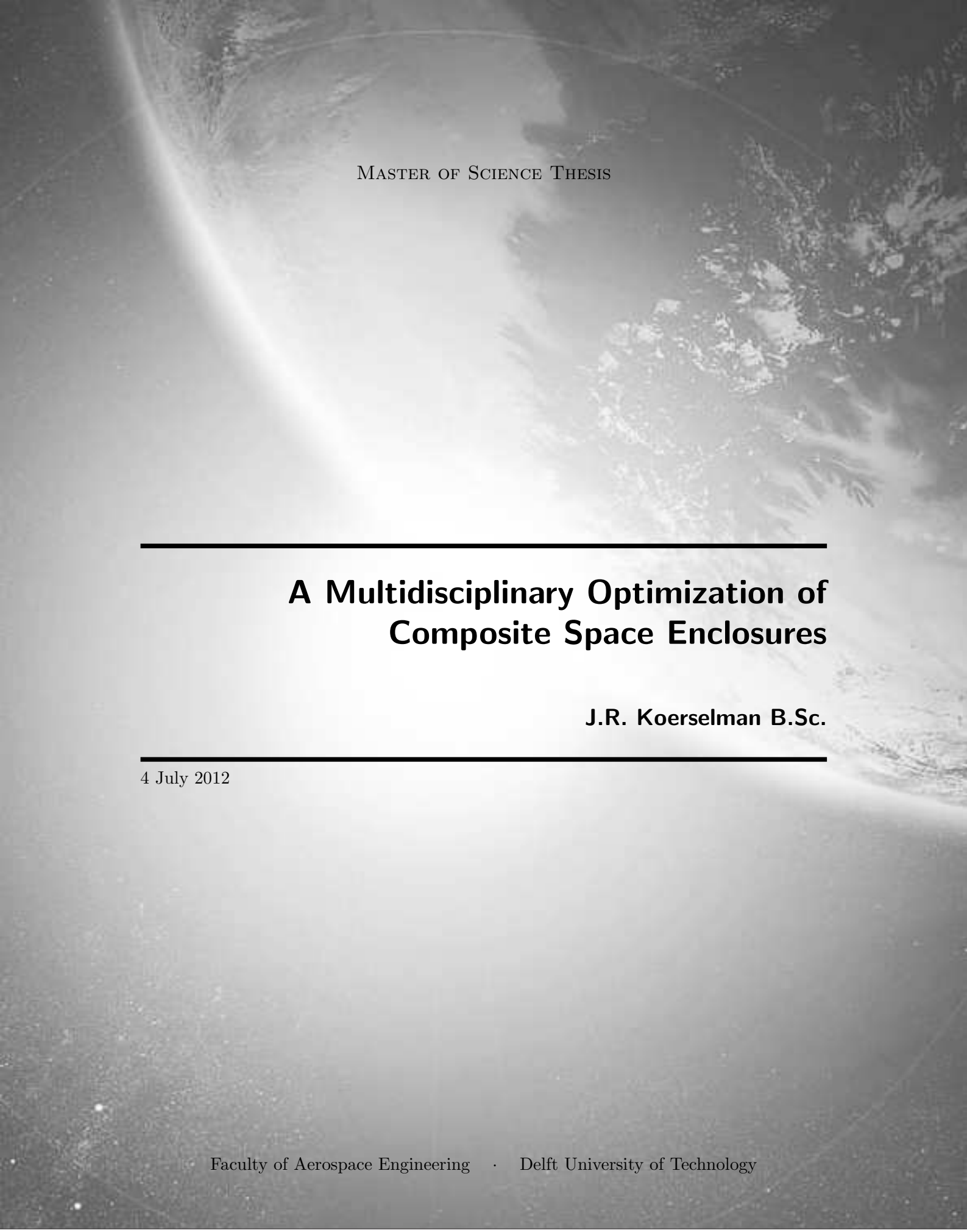

Master of Science Thesis

A Multidisciplinary Optimization of Composite Space Enclosures

J.R. Koerselman B.Sc.

4 July 2012

Faculty of Aerospace Engineering · Delft University of Technology

A Multidisciplinary Optimization of Composite Space Enclosures

Master of Science Thesis

For obtaining the degree of Master of Science in Aerospace Engineering at Delft University of Technology

J.R. Koerselman B.Sc.

4 July 2012

Faculty of Aerospace Engineering · Delft University of Technology

Delft University Of Technology
Department Of
Design, Integration and Operations of Aircraft and Rotorcraft

The undersigned hereby certify that they have read and recommend to the Faculty of Aerospace Engineering for acceptance a thesis entitled **"A Multidisciplinary Optimization of Composite Space Enclosures"** by **J.R. Koerselman B.Sc.** in partial fulfillment of the requirements for the degree of **Master of Science**.

Dated: 4 July 2012

Head of department: _____
prof.dr.ir. R. Benedictus

Supervisor: _____
dr.ir. R. Vos

Reader: _____
dr. J. Guo

Summary

A design methodology for composite space enclosures was generated. As a result a panel of an electronics housing structure, as part of a general satellite traversing both GEO and LEO, was designed and optimized. A mass saving of 18% was achieved over a conventional aluminum panel, while assuring structural integrity for acceleration loads, avoiding vibrational resonance with other satellite components, allowing electrical conductance, providing sufficient radiation protection from the harsh space environment and at the same time assuring manufacturability. The optimized structure was composed of layers of carbon fiber composite and tungsten foils. For radiation purposes the layers were placed asymmetric around the geometric midplane, resulting in shape distortions due to residual thermal stresses from the curing process. These shape distortions were kept to a minimum. The validity of the theoretical models was assessed by means of testing for shape distortions, radiation attenuation, bonding strength and electrical resistivity. The bonding of the tungsten with the prepreg material was found to be problematic, but an improvement in lap shear strength was found with respect to methods proposed in the literature. A chemical etching surface treatment with a reduced etching time of one minute was proposed for the tungsten foils.

Acknowledgments

I wish to express my gratitude to my direct supervisors Mr. Brander and Dr. Vos for helping me through this project. Moreover I am grateful for all the help and insight my other colleagues at Aalto University have provided me with. Also I wish to thank my colleagues at partner companies CSL, Tecnalia, Sensor Center Oy and Yuzhnoye for the good cooperation and valuable feedback.

Furthermore I wish to thank my friends, family and girlfriend for providing me with the mental support during the course of this project.

The research leading to these results has received funding from the European Community's Seventh Framework Programme (FP7/2007-2013) under Grant Agreement no. 262746.

Delft, The Netherlands
4 July 2012

J.R. Koerselman B.Sc.

Contents

List of Figures

List of Tables

Nomenclature

Latin Symbols

A	Activity	[Ci]
A	Atomic Weight	[u]
A	Cross-Sectional Area	$[\mathrm{m}^2]$
a	Acceleration	$[\mathrm{m\,s}^{-2}]$
b	Number of Possible Ply Angles	[–]
C	Shell Correction Factor	[–]
C	Capacitance	[F]
c	Speed of Light	$[\mathrm{m\,s}^{-1}]$
d	Deviation	[–]
E	Effective Thickness	[m]
E	Energy	[eV]
E	Young's Modulus	$[\mathrm{N\,m}^{-2}]$
e	Error	[–]
F	Force	[N]
f	Frequency	[Hz]
f	Photofraction	[–]
G	Electrical Conductance	[S]
G	Shear Modulus	$[\mathrm{N\,m}^{-2}]$
g	Fermi Density Correction Factor	[–]
g	Geometric Efficiency	[–]
g	Gravitational Acceleration	$[\mathrm{m\,s}^{-2}]$

H	Hardness	$[\mathrm{N\,m^{-2}}]$
h	Height	[m]
h	Planck's Constant	$[\mathrm{J\,s}]$
I	Electrical Current	[A]
I	Intensity	$[\mathrm{J\,s^{-1}\,m^{-2}}]$
I	Mean Excitation Energy	[eV]
i	Inclination Angle	$[^\circ]$
J	Poisson Ratio Factor	$[\mathrm{m^2\,N^{-1}}]$
k	Number of Composite Layers	[–]
L_1	Higher-order Bloch Correction Factor	[–]
L_2	Barkas Polarization Correction Factor	[–]
L_t	Time Resolution Factor	[–]
l	Length	[m]
m	Mass	[kg]
N	Line Load	$[\mathrm{N\,m^{-1}}]$
N_t	Time Resolution Count Number	[–]
N_A	Avogadro's Number	$[\mathrm{mol^{-1}}]$
n	Number of Plies	[–]
p	Pressure	[Pa]
p	Statistical P-value	[–]
Q	Transmissibility Factor	[–]
Q	Charge	[C]
Q	Transformed Reduced Stiffness	$[\mathrm{N\,m^{-2}}]$
R	Electrical Resistance	$[\Omega]$
R	Resolution	[–]
R_a	Mean Arithmetic Surface Roughness	[m]
R_E	Earth's Radius	[m]
R_T	Transmissibility Ratio	[–]
r	Distance	[m]
r	Radius	[m]
S	Stopping Power	$[\mathrm{eV\,cm^2 g^{-1}}]$
T	Temperature	[K]
t	Thickness	[m]
t	Time	[s]
u, v, w	Deflections	[m]
V	Voltage	[V]
v	Volume	$[\mathrm{kg\,m^{-3}}]$
v	Velocity	$[\mathrm{m\,s^{-1}}]$

W	Angular Correction Factor	$[-]$
w	Width	$[\mathrm{m}]$
x, y, z	Dimensional Coordinates	$[-]$
x_c	Configuration Vector	$[-]$
x_l	Lay-Up Orientation Vector	$[-]$
Z	Atomic Number	$[-]$
z	Charge Number	$[-]$

Greek Symbols

α	Linear Coefficient of Thermal Expansion	$[\mathrm{K}^{-1}]$
β	Relative Particle Velocity	$[-]$
γ	Lorentz Factor	$[-]$
Δ	Difference	$[-]$
δ	Deflection	$[\mathrm{m}]$
δ	Density Factor	$[-]$
ϵ	Intrinsic Detector Efficiency	$[-]$
ϵ	Strain	$[-]$
ϵ_0	Vacuum Permittivity	$[\mathrm{F\,m}^{-1}]$
ζ	Damping Ratio	$[-]$
η	Gamma Decay Fraction	$[-]$
θ	Apex Angle	$[^\circ]$
θ	Fiber Lay-Up Angle	$[^\circ]$
λ	Longitude	$[^\circ]$
λ	Wavelength	$[\mathrm{m}]$
μ	Mean	$[-]$
μ	Specific Attenuation Coefficient	$[\mathrm{m}^{-1}]$
μ	Viscosity	$[\mathrm{m}]$
ν	Poisson's Ratio	$[-]$
ν	True anomaly	$[^\circ]$
Π	Potential Energy	$[\mathrm{J}]$
ρ	Density	$[\mathrm{g\,m}^{-3}]$
ρ	Electrical Resistivity	$[\Omega\,\mathrm{m}]$
σ	Cross section	$[\mathrm{m}^2]$
σ	Electrical Conductivity	$[\mathrm{S\,m}^{-1}]$
σ	Standard Deviation	$[-]$
σ	Stress	$[-]$
τ	Shear Strength	$[\mathrm{N\,m}^{-2}]$

ϕ	Scattering Angle	[°]
Ω	Input Frequency	[rad s^{-1}]
Ω	Right Ascension of the Ascending Node	[°]
Ω	Solid Angle	[sr]
ω	Argument of Perigee	[°]
ω_n	Undamped Frequency	[rad s^{-1}]

Subscripts

$_\gamma$	Photon
$_c$	Critical
$_{eq}$	Equivalent
$_e$	Electron
$_f$	Fiber
$_l$	Longitudinal
$_m$	Matrix
$_{ply}$	Ply
$_p$	Particle
$_{se}$	Even number of plies, symmetric around the geometric midplane
$_{sh}$	Shrinkage
$_{so}$	Odd number of plies, symmetric around the geometric midplane
$_{tot}$	Total
$_t$	Target or Transverse
$_{ult}$	Ultimate

Abbreviations

AED	Advanced Equipment Design
AFM	Atomic Force Microscopy
CLT	Classical Lamination Theory
CME	Coronal Mass Ejection
CMF	Compound Mass Fraction
CMOS	Complementary Metal-Oxide-Semiconductor
CSL	Centre Spatial de Liège
CTE	Linear Coefficient of Thermal Expansion
DLC	Diamond-like Carbon
EDS	Energy Dispersive Spectroscopy

EMF	Elemental Mass Fraction
ESF	Elemental Stoichiometric Fraction
FEPE	Full-Energy Peak Efficiency
FF	Fiber Failure
FWHM	Full Width Half Maximum
GCR	Galactic Cosmic Ray
GEO	Geostationary Orbit
GSO	Geosynchronous Orbit
IFF	Inter-Fiber Failure
LEO	Low Earth Orbit
LET	Linear Energy Transfer Coefficient
MEK	Methyl Ethyl Ketone
MoS	Margin of Safety
NID	Non-Ionizing Dose
PCB	Printed Circuit Board
PSD	Power Spectral Density
RF	Reserve Factor
RSS	Root Sum Square
SCR	Sun Cosmic Ray
SEB	Single-Event Burnout
SEGR	Single-Event Gate Rupture
SEL	Single-Event Latchup
SEM	Scanning Electron Microscope
SEU	Single-Event Upset
SF	Safety Factor
SoI	Silicon on Insulator
SPE	Solar Particle Event
ST	Surface Treatment
TID	Total Ionizing Dose
TRB	Trapped Radiation Belt

Other Symbols

$\hat{}$	Fraction
$\bar{}$	Areal

Chapter 1

Introduction

As a result of the trend in space engineering towards cost reduction the application of non-space-qualified electronics in satellites has become common practice [1, 2]. Ionizing particles in the harsh space environment could damage the non-radiation-hardened electronic devices, potentially impairing the satellite's main functions [3]. In order to provide the devices with sufficient protection an electronics housing structure should attenuate the incident radiation. Traditionally, the electronics housing structures are made of aluminum. However, as has been shown in other aerospace applications, the application of composite materials could potentially lead to large mass savings. With the high costs of sending a unit mass of payload into orbit the mass should be minimized. Therefore the application of composite materials in electronics housing structures was proposed. In this thesis the radiation attenuation properties of such composite structures is investigated.

The main objective of this research is to generate a design methodology for composite space enclosures and to apply the methodology to optimize the mass of the top panel of an electronics housing structure for satellites. The proposed design methodology includes constraints with respect to radiation attenuation, natural frequency, structural integrity and electrical resistivity, while at the same time limiting the shape distortions caused by thermal loading.

For the assessment of the practical applicability of the proposed design methodology an old design case was investigated. The considered design case was part of ESA's Advanced Equipment Design (AED) studies [1, 4–6]. Part of the work presented in this thesis was a continuation on the AED-studies, which were aimed at investigating the practical applicability of composite materials for spaceborne electronics housing structures. Thermal and structural aspects were considered, whereas radiation attenuation properties were only investigated briefly. More advanced and novel unsymmetric laminate configurations were proposed in this thesis for the optimization of the radiation attenuation. With the implementation of the more advanced configurations manufacturing problems occur, such as post-cure shape distortions. This is investigated in more detail in this thesis. Also a focus is put on the bonding characteristics between the composite materials and the co-cured metallic foils, which were implemented for improvement of radiation attenuation properties.

Since the design methodology was created for general electronics housing structures the exact forces were ill-defined for the complete box. In this thesis only flat panels were considered. The dimensions and forces through accelerations were obtained from the preceding AED-studies. The dimensions of the top panel were respectively 246.5 and 412 mm in x- and y-directions, whereas the z-axis was taken to be in out-of-plane direction. A set of wedge locks and Printed Circuit Boards (PCB), running in x-direction, is included in the structural model. A similar box structure is shown in Figure 1.1, showing the placement of the PCBs (in green) and the wedge locks (in purple). The black top panel was optimized.

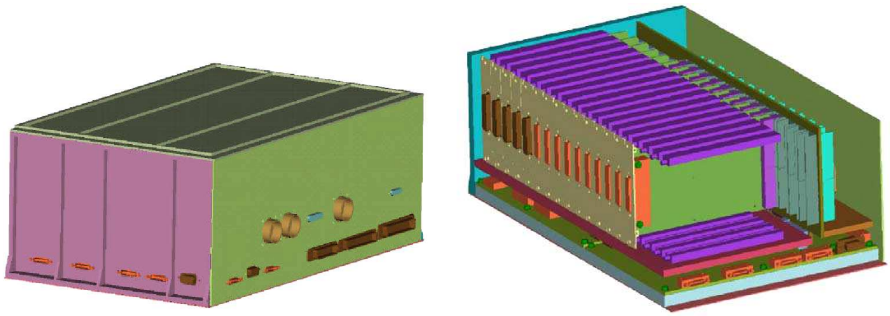

(a) (b)

Figure 1.1: AED electronics housing structure: A (a) closed and (b) open configuration. The black top panel was redesigned and optimized. After [7].

This research has been performed as part of the SIDER project. The main objective of the SIDER project is "to develop technologies and tools required to obtain lightweight, safe, robust and reliable structures" [8]. The research presented here was done for Aalto University and in cooperation with partner companies Tecnalia, Sensor Center Oy, Yuzhnoye and Centre Spatial de Liège. It should be noted however that the contents of the thesis are just a reflection of the author's views and the Community is not liable for any use that may be made of the information contained therein. For more information on the SIDER project the reader is referred to the webpage: http://www.sider-project.eu.

The background of the optimization problem and the bonding strength between dissimilar materials are discussed in Chapter 2. In Chapter 3 the design methodology is discussed. Furthermore a validation of the theoretical models is provided by means of testing. In Chapter 4 the design methodology is applied to the practical case and the optimization results are presented. Furthermore a comparison is made between the composite structure and a conventional aluminum structure.

Chapter 2

Scope

In this chapter the background of the mass optimization problem is discussed. In the first section the background of radiation environment and its possible effects are addressed. It also covers the literature review on the shielding problem and provides the reader with the insight of what shielding concepts have been applied in the past. Thereafter the bonding of dissimilar materials is addressed, since the bonding is an important prerequisite for the manufacturing of laminates.

2.1 Radiation Environment

The radiation to which the electronics inside a satellite are exposed and its effects are dependent on the environment the satellite traverses. Upon interaction with the target material different mechanisms will occur for different incident particles. One incident particle, a primary, in the shielding material might result in the generation of a large quantity of secondary particles (secondaries), which could all potentially damage the electronics. The type and number of secondary particles depends on the target material, which as such should be optimized, to limit the damage to the semiconductors. The possible effects on the electronics are discussed in Section 2.1.1. In order to get a general understanding of the involved processes the radiation sources are discussed in Section 2.1.2 and the mission parameters are introduced in Section 2.1.3.

2.1.1 Damage Effects

Due to a trend in cost reduction in space missions and a reduction in number of manufacturers of radiation-hardened electronics an increasing amount of non-space-qualified commercial off-the-shelf electronics devices are used. Decreased power production by the solar arrays, failure of sensitive electronics and increased background noise in sensors are some of the effects of the radiation on the satellites. Complementary Metal-Oxide-Semiconductor (CMOS) devices and Silicon on Insulator (SoI) devices, where the silicon

is dielectrically isolated, are the most common devices. Typical bulk CMOS is shown in Figure 2.1. The radiation effects are divided in ionization and lattice displacement effects.

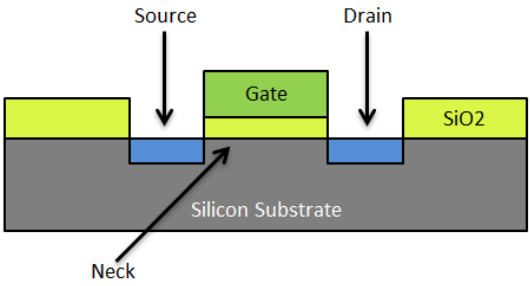

Figure 2.1: Bulk CMOS, where the gate is dielectrically isolated with a silicon oxide layer.

Ionization Effects

Charged particles are able to cause ionization, which can either give rise to single-event effects or cumulative effects. By means of direct ionization electron-hole pairs are freed along the incident particle's path [2].

Single-Event Effects The effect of irradiation on the electronics depends on the localization and the amount of injected charge during irradiation. Irradiation can lead to non-destructive effects and destructive effects. Single-Event Upsets (SEU) or so-called soft errors will not interfere with any operations and will only alter a logical value within the device. The probability of this event is a function of the critical charge parameter ($Q_c = C \cdot V$) and as such dependent on capacitance C and voltage V. Modern devices have lower supply voltages, thus increasing the susceptibility to SEUs [9].

In the case of Single-Event Latchup (SEL) the device will malfunction, draw excessive current from the system and will not operate until the power is switched off and on again. SoI devices are hardened by design from SELs. In case of Single-Event Burnout (SEB) the device fails permanently. The device is destroyed thermally due to excessive currents [10]. Single-Event Gate Rupture (SEGR) is caused by heavy ions hitting the neck regions of electronic devices, leading to a flow of electrons towards the drain, short-circuiting the oxide field [11].

Cumulative Effects Both protons and electrons can also affect the functionality of electronics by accumulation of long-term ionizing damage. The incident particles create electron-hole pairs in the gate insulation layers, leading to photocurrents during recombination. Furthermore the freed electrons have a higher mobility than the holes. As such the electrons can exit the oxide, leaving the holes behind and resulting in a reduced semiconductor effectiveness. With the reduction in feature size and hence a reduction in oxide layer thickness the charge that can be trapped is limited. Therefore the Total Ionizing Dose (TID) hardness has increased with advancements in technology. However, at the thicker oxide layer at the field, charge does still get trapped, possibly resulting in leakage currents and altered threshold voltage levels.

Lattice Displacement Effects

Lattice displacement damage (or Non-Ionizing Dose, NID) is caused by the physical displacement of atoms in the crystal lattice to an interstitial position, leaving a vacancy behind. This leads to Frenkel defects, reducing minority carrier lifetime, changing the majority carrier charge density and reducing carrier mobility [12]. Lattice displacements can be caused by protons, neutrons, heavy ions, alpha particles and high-energy photons. By means of indirect ionization the incident particle breaks up the target material, leading to the generation of secondaries (photons, electrons, positrons, neutrons, alpha particles and light ions) and as such a cascade of further collisions. The target material recoil fragments will ionize and as such become the main cause of damage production in semiconductors.

2.1.2 Radiation Sources

In the traversed orbits different radiation environments are experienced. Three main sources can be distinguished for the space radiation: Trapped Radiation Belts (TRB), Sun Cosmic Rays (SCR) and Galactic Cosmic Rays (GCR).

Trapped Radiation Belts

The Earth's Trapped Radiation Belts, also commonly referred to as Van Allen Radiation Belts, are two tori of huge flows of electrons and protons surrounding the Earth, caught by the Earth's dipole magnet field [13]. The belts are shown schematically in Figure 2.2. The inner belt consists of both protons and electrons, whereas the outer belt consists of mostly electrons, as is shown in Table 2.1. Even though the inner belt officially starts at 100 km, the real effect is experienced from 1,000 km altitude on [14, 15]. The offset from the Earth's surface is caused by the dense atmosphere below 100 km, leading to high particle energy losses. In Table 2.1 the distance from the Earth's center is given in Earth Radii ($R_E = 6,371$ km). Low-Earth Orbits (LEO) traverse the inner proton-rich radiation belt, whereas Geostationary Orbits (GEO) traverse the outer electron-rich radiation belt.

Moreover the offset of the Earth's magnetic field from the Earth's axis of rotation (of approximately 10.8°) leads to a geomagnetic drop and an increase in proton flux in front of Brazil's coast line [16]. This anomaly is known as the South Atlantic Anomaly and affects high-inclination LEOs.

Van Allen Belt	Composition	Energy [MeV]	Distance from the Earth [R_E]
Inner belt	Protons	$0.1 - 400$	$1.02 - 2.4$
	Electrons	< 0.78	
Outer belt	Electrons	$0.04 - 7$	$2.8 - 12$

Table 2.1: Trapped radiation belt composition. Data obtained from [13, 17–19].

Due to Lorentz forces the entrapped particles experience three basic motions [20]: Firstly gyration around magnetic field lines can be identified, based on the conservation of relativistic magnetic moment. Secondly a bounce along the field lines, caused by the convergence of the field lines towards the poles is found. Furthermore a drift of the charged

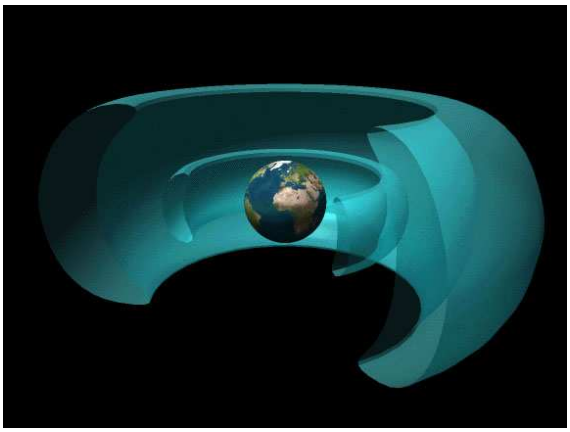

Figure 2.2: The trapped radiation belts are two distinct belts surrounding the Earth. The inner belt consists of mostly protons, whereas the outer belt consists of electrons.

particles is experienced, leading to the creation of the so-called ring current. Electrons turn counterclockwise and protons drift clockwise, viewed from the North pole, as can be seen from Figure 2.3. The periods of the motions, for a 3 MeV electron, are respectively $2.14 \cdot 10^{-4}$, 0.19 and 504 s.

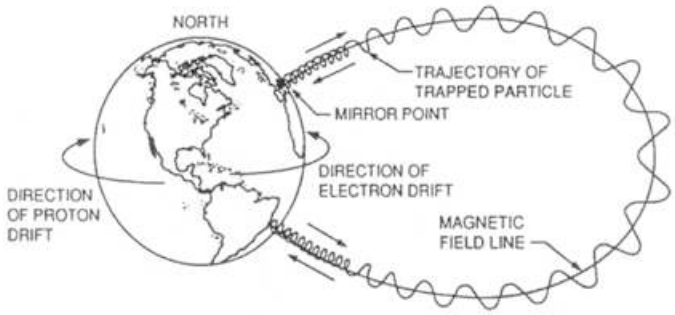

Figure 2.3: The motion of charged particles trapped in one of the Van Allen radiation belts. After [21].

Sun Cosmic Rays

Sun Cosmic Rays are caused by Solar Particle Events (SPE), which occur approximately 50 times per eleven-year solar cycle and usually take place during its declining phase [19, 22]. Solar particle events are divided into Solar flares and Coronal Mass Ejections (CME), which are tabulated into Table 2.2 and shown in Figure 2.4. When energy storage in the solar magnetic field becomes excessive a burst of energy is suddenly released. CMEs are large eruptions of proton-rich plasma (a gas of free ions and electrons) that drive a shock wave outwards and accelerate particles to ultrasonic speeds of $50 - 1200\,\mathrm{km\,s^{-1}}$ in the process [20].

Due to magnetic shielding, which is a resultant of the orientation of the Earth's magnetic field lines, Sun Cosmic Rays are deflected away from the Earth's equator and drawn

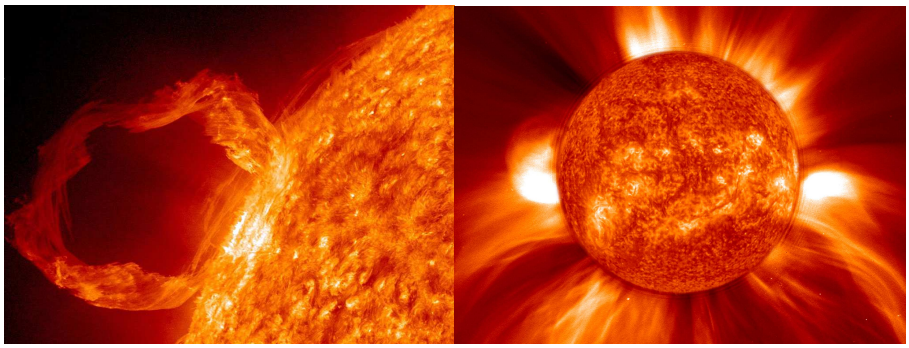

(a) (b)

Figure 2.4: Solar particle events are divided into electron-rich Solar flares (a) and proton-rich Coronal mass ejections (b). (Courtesy NASA/GSFC & SOHO/EIT/LASCO)

SPE	Composition	Fluence [cm^{-2}]	Period
Solar Flares	Electrons	$10^7 - 10^8$	< 5 hours after the initial phase
CMEs	96.4% Protons 3.5% Alpha particles 0.1% Heavy Ions	10^9	In the order of days

Table 2.2: Solar particle event composition. Data obtained from [19, 23].

towards the poles, resulting in the Aurora, as observed on the Earth. Hence the magnetic shielding for LEOs is high at the equator but low at higher latitudes. For GEOs the magnetic shielding is smaller than for LEOs, due to the weaker magnetic field at large altitudes.

Galactic Cosmic Rays

Galactic Cosmic Rays originate from outside of the Solar system and their composition is proportional to solar system material: 98 percent hadrons and 2 percent leptons. The hadrons are subdivided in protons, alpha particles and heavy ions, as shown in Table 2.3 [19, 24].

Type	Percentage	Composition	Relative Fraction
Hadrons	98%	Protons	87%
		Alpha particles	12%
		Heavy ions	1%
Leptons	2%	Electrons	100%

Table 2.3: Galactic cosmic ray composition

The GCR flux is inversely proportional to the solar activity, due to a reduction in attenuation by solar winds at solar minimum. Similarly as SCRs, GCRs are affected by the magnetic shielding. However, the influence of GCRs on the total absorbed dose is

negligible, w.r.t. the other sources, just as the effect of shielding on GCRs in general, as can be seen from Figure 2.5. Therefore GCRs will be omitted from further research. Note that the ISS mission has different orbital parameters (355 km altitude, 51.6° inclination) than the proposed LEO, which will be discussed in the next section, but a similar trend can be found.

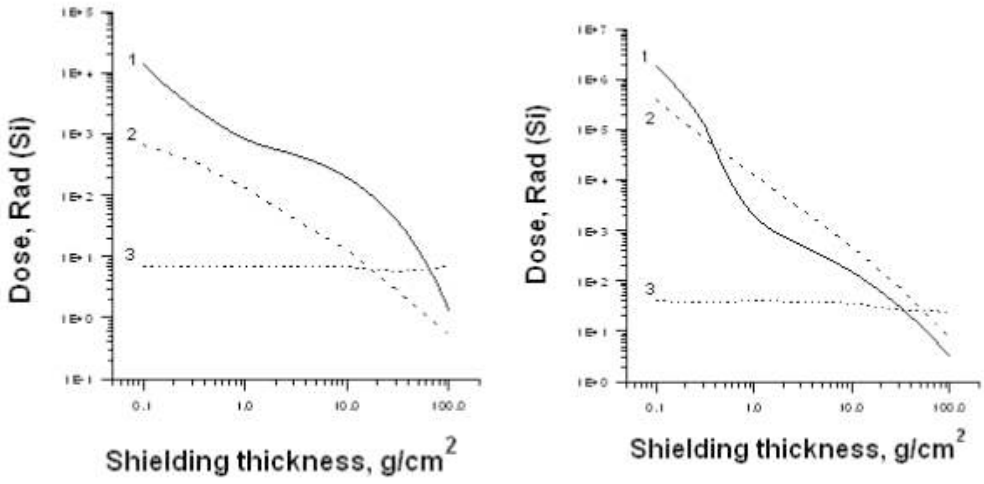

(a) (b)

Figure 2.5: Absorbed dose versus shield thickness for (a) a 10-year ISS mission and (b) a GSO mission. Radiation sources 1-3 are respectively TRB, SCR and GCR. After [13].

2.1.3 Mission Parameters

For the SIDER project two missions were proposed: One 18-year GEO mission at 36° longitude and one 7-year LEO mission. The considered orbits are summarized in Table 2.4. GEOs are variations to a Geosynchronous orbit (GSO), commonly used for telecommunication purposes. They are characterized by their orbital periods, which equal the Earth's sidereal rotation period [13]. GEOs differentiate themselves by their 0° inclination angle, such that they appear to remain stationary to ground observers.

The LEO considered in this thesis is a 60° prograde inclination orbit at 1,600 km altitude. At altitudes below 1,000 km the radiation environment is less severe (scales with distance to the power of five), but a penalty for higher atmospheric drag and limited coverage has to be paid [25]. As a circular orbit the LEO does not have a uniquely determined perigee, hence the argument of perigee ω and true anomaly ν were assumed to be zero-valued. Also the right ascension of the ascending node Ω with respect to reference direction γ_{50} was assumed to be zero, with the mission starting on January 1 2011.

With the omission of GCRs and the relatively low SCR electron flux only TRBs and SCR protons were considered for further analysis. This is summarized in Table 2.5.

The orbital parameters were implemented into the Geant4-based MULASSIS simulation tool. Geant4 is a particle simulation tool developed by CERN and is known for its high

Orbit	Duration [years]	Altitude [km]	Inclination i [°]	Longitude λ [°]
LEO	7	1,600	60	$\lambda(t)$
GEO	18	35,794	0	36

Table 2.4: Mission parameters

Radiation	Particle	Energy [MeV]
TRB	Electrons	$0.04 - 7$
TRB	Protons	$0.1 - 400$
SCR	Protons	$0.1 - 1000$

Table 2.5: Radiation environment contributions

accuracy. In accordance with ECSS standards, for the modeling of the TRBs the AP-8 proton model and AE-8 electron model are applied at solar maximum [17]. The obtained fluences for the first orbit for the LEO and GEO missions are plotted in Figures 2.6 and 2.7, respectively. It was verified that for the proposed missions the LEO traverses a proton-rich environment, whereas the GEO traverses the electron-rich outer radiation belt. Similarly for the long-term solar particle fluences the ESP-Psychic model for worst case events is used, with a confidence level of 95%.

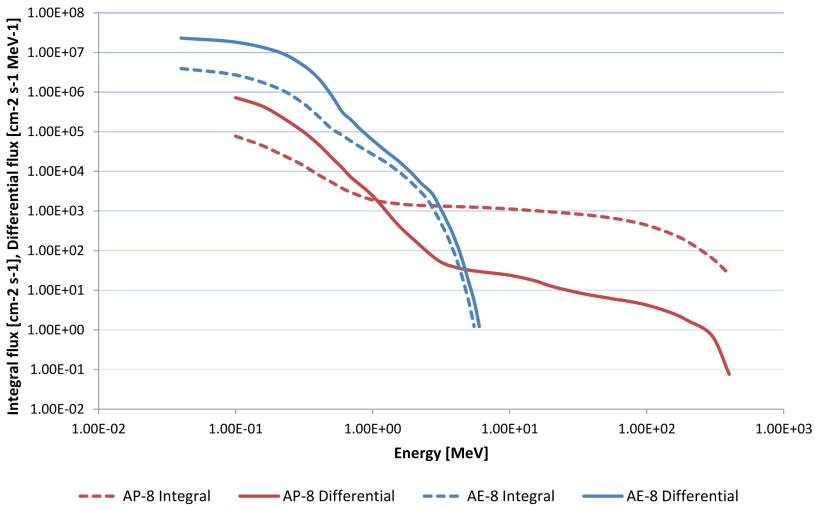

Figure 2.6: TRB particle fluence in LEO. High-energy protons, indicated in red, were found in LEO.

2.1.4 Previously Applied Configurations

The concept of radiation shielding has been researched in the last two decades. Whereas currently aluminum shielding is applied the research on laminates started with Mangeret et al. [26]. Mangeret et al. showed that low-Z materials (materials with low atomic numbers Z) attenuate protons better than their high-Z counterparts. Electrons and photons were attenuated more effectively by high-Z materials. Bilayer concepts, having a high-Z

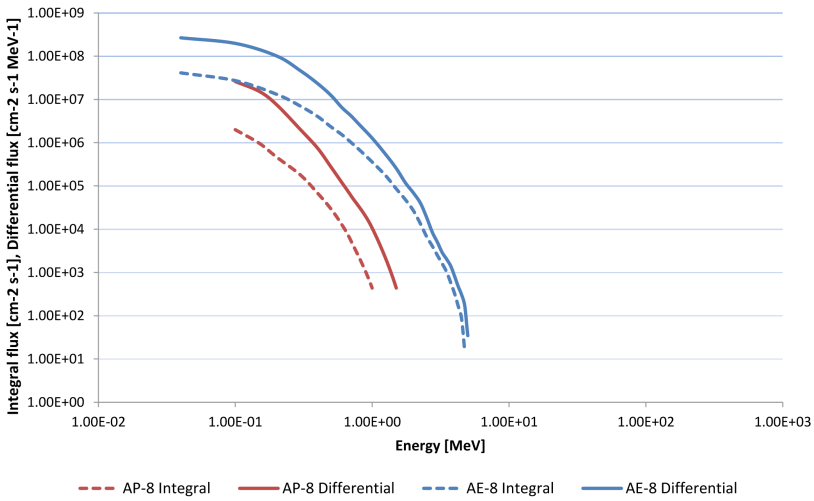

Figure 2.7: TRB particle fluence in GEO. Large quantities of electrons, indicated in blue, were found in GEO.

layer on the outside and a low-Z layer on the inside showed to be more effective than the individual materials, in case both protons and electrons needed to be attenuated. For a GSO a trilayer concept, with a high-Z layer located in between two low-Z layers proved to be even more effective, leading to a mass reduction of 40% w.r.t. an aluminum reference. The optimum thickness of the high-Z layer depends on the radiation environment, such that for electron-rich orbits a larger quantity of high-Z materials is required.

Fan et al. showed that for electron-rich environments the radiation dose could be reduced by as much as 60% using a trilayer concept, whereas the implementation of a thin high-Z layer only had a minor negative effect for proton-rich orbits [27]. Note that absorbed dose decreases logarithmically with target depth. Fan et al. were among the first ones to investigate the configuration where the high-Z layer was placed aft of the geometric midplane. The effectiveness of this offset was later also proven by others [28–30]. Based on these findings Abusafieh et al. found a mass saving of 25% w.r.t. an aluminum reference, for a trilayer of composite materials and tantalum in GSO [31].

As part of the AED-studies, on which this thesis was built, it was found by Garcia et al. that a trilayer configuration, featuring carbon fiber composites and tungsten, also the proton attenuation could be improved w.r.t. aluminum, due to the lower atomic number of carbon. Also the proton attenuation was found to be almost independent of location of the metallic high-Z layer [1, 5].

A combination of all discussed factors has not yet been investigated. The AED-studies focused on symmetric composite laminates and the practical applicability was shown. However, unsymmetric laminates, which tend to be more effective for electron attenuation, have not been applied in practice. Therefore the manufacturability and effectiveness of such composite laminates is investigated in this thesis.

2.2 Bonding Strength

For the manufacturing of laminates it is essential to have a good bonding strength between the different materials. Therefore the bonding strength of carbon fiber composites and metallic foils were investigated. In order to successfully bond two dissimilar materials (hic: tungsten and carbon fiber prepreg) the metal surface was roughened for an increase in effective contact area and for the removal of contaminations and thus better adhesion. This section describes different surface treatment methods for tungsten foils. The proposed surface treatments were tested to optimize the bonding strength between the adherents. The manufacturing process of the test samples are treated first, after which the test results are given and discussed.

2.2.1 Test Setup

The adhesive bond between the adherents was not allowed to be the weakest link of the joint and was therefore tested. Due to limited resources initial comparative testing was limited to shear tests. One of the easiest and cheapest tests in order to determine the mode II strength of an adhesive joint is the single-lap shear test (ASTM D5868-01) [32]. Comparative analysis between the different surface treatments gives an idea of the overall strength of the joint. The single-lap shear tests measures a mix of mode I and mode II, due to the asymmetry of the test specimen, resulting in an offset between the applied load and the center line. Load path eccentricity occurs, leading to out-of-plane bending moments and high peel stresses.

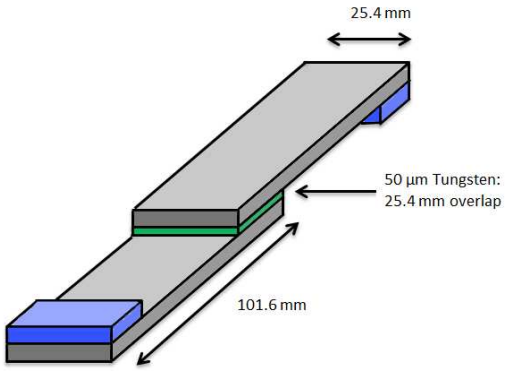

Figure 2.8: Lap shear test setup. Additional coupon parts (indicated in blue) were bonded to the ends of the specimen to reduce force eccentricity. As such the test method deviated from the ASTM standards.

The test samples were composed of two rectangular coupons, having a width w of 25.4 mm, a length of 101.6 mm and a thickness of 2.54 mm, as is shown in Figure 2.8. They were bonded together over a distance l of 25.4 mm, where a tungsten foil was co-cured in the overlap-region. The lap-shear strength τ is given as a function of maximum applied force F by Equation 2.1.

$$\tau = \frac{F}{w \cdot l} \tag{2.1}$$

A total of six configurations were tested, out of which one was a reference test without tungsten foil. Five samples were tested for each configuration, in accordance with the ASTM standard. Each composite coupon was required to have a thickness of 2.54 mm. As such a total of 8.91 layers of prepreg was needed to acquire the correct thickness. This number was rounded off to nine layers, leading to a total nominal thickness of 2.57 mm, instead of the prescribed 2.54 mm. The specimen loading rate was given to be 13 mm/min.

2.2.2 Manufacturing

The manufacturing procedure of the composite laminates was prescribed by the prepreg manufacturer. For the manufacturing of any of the test samples a flat mold was used, which can be seen from Figure 2.9. Before manufacturing the mold was degreased with Butanone (also known as Methyl Ethyl Ketone, MEK) and white cloth, after which a ZYVAX water shield release agent was applied with white cloth. After application of the release agent the plate was wiped with white cloth after two minutes. This procedure was repeated after a 15-minute interval.

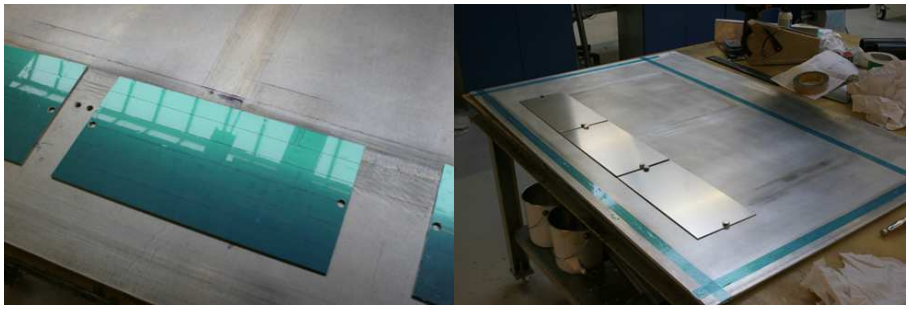

(a) (b)

Figure 2.9: (a) Additional tape was added to the 2.5 mm aluminum plates to obtain the required height and (b) were thereafter bolted to the plate to constrain their movement during the curing process.

Due to the non-flat shape of the lap shear test specimens additional plates were required for the mold, which were treated in similar fashion as the flat mold itself. This is shown schematically in Figure 2.10. The additional plates were bolted onto the flat mold to keep the plates in place.

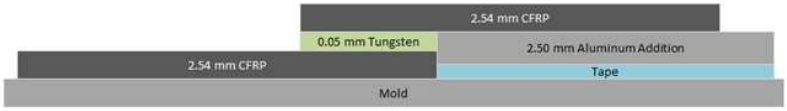

Figure 2.10: Schematic overview of the mold structure, featuring additional tape in order to achieve the required coupon thickness.

For the additions aluminum plates of 2.50 mm were used and 0.15 and 0.05 mm tape was used for respectively the tungsten configurations and the pure composite configuration, as can be seen from Figure 2.9. This lead to plate thicknesses of respectively 2.65 and 2.55 mm, whereas 2.62 and 2.57 mm was required.

Unidirectional carbon fiber prepreg layers were used for the composite structures. The orientation of each individual layer could be varied. All orientations are given in degrees w.r.t. the primary coordinate axis. Throughout this thesis the following stacking sequence writing convention is applied: Subscript s denotes that the stacking sequence is repeated symmetrically around the geometric midplane. The additional subscripts e and o indicate whether the laminate has an even or odd number of layers. E.g. $(0/90)_{se}$ equals a $(0/90/90/0)$ laminate, whereas $(0/90)_{so}$ indicates a $(0/90/0)$ laminate. A numerical subscript denotes the number of prepreg layers in the specified direction. E.g. $(0_2/90)$ refers to a $(0/0/90)$ laminate. Letters S, W and Gd refer to respectively foils of steel 1.4310, tungsten and gadolinium and the superscript indicates the respective foil thickness in µm.

In accordance with the ACG standard all prepreg laminates were vacuum bagged for 30 minutes after placement of three additional plies, in order to remove any entrapped air [33]. After ply stacking, including optional metallic layers, the laminates were cured in the autoclave at 120 °C for one hour, with a vacuum pressure difference of −0.88 bar and an autoclave pressure of 5.8 bar. The pressure was limited by the autoclave's capabilities.

The prepreg plies were cut into parts of 200×150 mm, leaving a margin for manufacturing errors, having the required ply orientations of $(0/45/-45/90/0)_{so}$. After curing in the autoclave the excess resin was removed. Manufacturing was done in two batches of three configurations. Excess coupon material in longitudinal direction was removed and was adhered with 3M Scotch Weld DP190 epoxy adhesive to the edge of the test specimen, in order to reduce the force eccentricity during the lap shear test. Note that the testing procedure as such deviates from the ASTM standard. Gauze was added in the adhesive layer, in order to achieve a homogeneous adhesive thickness. The adhesive was allowed to dry for three days, with stacks of weights placed on both sides of 10 kg each. Thereafter the sheets were cut, into strips of 2.54 mm wide, from the center of the cured laminates to provide homogeneous sample properties. A lap shear test sample is shown in Figure 2.11.

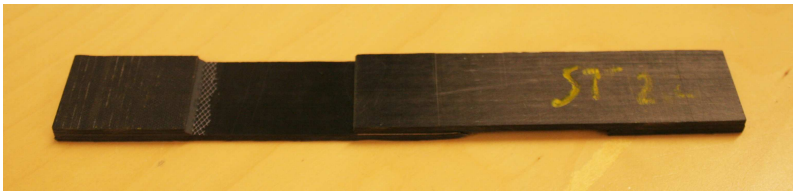

Figure 2.11: A lap shear test sample, with the tungsten layer positioned in between the carbon fiber composite coupons. Additional coupon material was added to the ends, in order to reduce force eccentricity.

2.2.3 Surface Treatments

Five different surface treatments were investigated and will be discussed in further detail in this section. Chemical etching with three different immersion times were tested, just as a Diamond-like Carbon coating and a grit blasting procedure. Also a pure composite material reference configuration was tested.

Grit blasting

In the AED-studies a grit blasting surface treatment was used for steel foils and was assumed to be applicable to tungsten too [6]. The applicability of this treatment on tungsten was assessed in this thesis. The grit blasting treatment was based on of seven steps:

1. Cleaning of the foil with Scotch Brite and MEK.
2. Wiping of the foil with white cloth and MEK.
3. Cleaning of the foil with Scotch Brite and distilled water.
4. Wiping of the foil with white cloth and distilled water.
5. Grit blasting of the foil.
6. Wiping of the foil with white cloth and MEK.
7. Applying of the primer for better adhesion.

A water break test was done to check the quality of the degreasing process, after which it was dried in a convection oven at 110 °C for one hour. The grit blasting was done with white F100 (large grit) Duralum aluminum oxide Al_2O_3 grit, at a pressure of 5 bar, under an angle of 45° and at a distance of 15 cm.

The original primer BR-127 was replaced for a primer with a lower volatile organic content: BR 6747-1 [34]. For this research the primer was applied with a brush, after stirring the primer for ten minutes in order to achieve a homogeneous substance. Thereafter the tungsten laminate was once more dried in the oven for one hour at 110 °C.

Chemical Etching

The second proposed surface treatment for tungsten was based on chemical etching [35, 36]. The tungsten-dedicated etching mixture quickly dissolves the tungsten, highly increasing the surface roughness [37]. The surface treatment consists of seven steps:

1. Degrease the foil in a vapor bath of trichloroethylene.
2. Abrade the foil surface with medium grit emery paper.
3. Degrease again, similarly to step 1. Prepare the solution described beneath, using fluoropolymer resins, polyethylene or polypropylene equipment. Blend the hydrofluoric acid and the nitric acid with the deionized water. Slowly add the sulfuric acid, stirring it constantly with a rod made out of either polytetrafluoroethylene or polyethylene. Add a few drops of 20% hydrogen peroxide.
4. Immerse the foil for $1 - 5$ minutes in the created solution at room temperature.
5. Rinse the foil under tap water.

6. Finish rinsing in distilled water.
7. Dry the foil in an oven at $71 - 82\,^{\circ}\mathrm{C}$ for $10 - 15$ minutes.

The composition of the etching solution is summarized in Table 2.6.

Solution Component	Mass Fraction [%]
Sulfuric acid (specific gravity 1.84)	50
Nitric acid (specific gravity 1.41)	30
Deionized water	15
Hydrofluoric acid, (60%wt concentration)	5

Table 2.6: Chemical etching solution

For this surface treatment a vapor bath was required, which was unavailable to the author. Therefore the proposed degreasing method was replaced by the degreasing method as was used for the grit blasting treatment. Steps 3-7 were done at the chemistry department of Aalto University.

Diamond-like Carbon Coating

The final investigated surface treatment was the Diamond-like Carbon (DLC) coating, which was applied by company DIARC-Technology Inc [38]. Note that the commercial DIARC-coating is not a pure DLC. The Diamond-like Carbon coating technology makes use of a thin film (1 µm) of amorphous diamond to increase the surface properties. The material is best known for its high hardness and tribological properties, such as high wear resistance and low friction. The properties of the DLC coating depend on its composition and thus the ratio between the sp^2 and sp^3 hybridized bonds, which are characteristic for respectively graphite and diamond. The adhesive strength is furthermore dependent on the thickness of the Diamond-like Carbon layer. With an increase in DLC thickness an increase in critical load can be achieved, up till the critical coating thickness, where the internal stresses will become dominating and will decrease the adhesive strength for thicker coating thicknesses [39].

2.2.4 Results and Discussion

The test results for the different Surface Treatments (ST) are tabulated by their respective mean μ and standard deviation σ as $(\mu \pm \sigma)$ and their respective failure mode(s) in Table 2.7.

Out of the six tested configurations, where ST1 was the reference test (14.70 ± 0.29 MPa), the DLC gave the highest mean shear strength (17.91 ± 1.48 MPa). The results will be discussed in more detail in the coming paragraphs. During testing four failure modes were identified, which are shown in Figure 2.12: Interfacial failure between the tungsten substrate and the composite material, cohesive failure in the composite's thin external resin layer, partial cohesive failure in the first ply of the composite and in the composite's thin resin layer and adherent (tungsten) failure. Note that multiple failure modes tend to occur simultaneously and occurrence of pure failure modes is rare.

ST	Test Configuration	Details	$\mu \pm \sigma$ [MPa]	Main Failure Mode(s)
ST1	Pure composite		14.70 ± 0.29	Cohesive
ST2	Grit blasting		15.15 ± 1.66	Partial Cohesive
ST3	Chemical etching	5-min	11.89 ± 0.64	Cohesive/Interfacial
ST4	Chemical etching	3-min	16.68 ± 1.21	All
ST5	Chemical etching	1-min	16.86 ± 1.70	(Partial) Cohesive
ST6	Diamond-like carbon		17.91 ± 1.48	Adherent/Partial

Table 2.7: Lap shear test matrix

Adverse Etching Effects

The second-highest lap shear strength was found for the chemical etching procedure ST5 (16.86 ± 1.70 MPa). The procedure was done for multiple immersion times. It was shown that a shorter immersion time, w.r.t. the five-minute immersion time given in the literature, led to a statistically significant higher shear strength ($p = 0.001$).

The reduced adhesion strength for larger immersion times was initially ascribed to an excessive increase in surface roughness. For small immersion times the surface roughness increases, increasing the effective wetted area of the tungsten. Past the critical immersion time the surface roughness would have increased to such extent that the resin would be unable to penetrate the adherent fully, leading to void formation below the resin and inherently inhibiting the wetting. This is commonly referred to as over-etching. The presence of voids potentially reduces the adhesion strength [40]. The wetting is also dependent on the resin viscosity and its time in fluid state [41]. Critical arithmetic average surface roughness values, R_a, range between 1 and 2 µm [42]. Low-viscosity resins, such as the MTM57 ($\mu \approx 2.0$ Pa s) can more easily penetrate the generated pores and will therefore have a critical surface roughness value of approximately $1.5 - 2$ µm [33].

In order to validate the assumption of over-etching the surface roughness was measured for tungsten foils with different immersion times (0, 30 60, 180 and 300 s) using a Surtronic 3 profilometer. For all foils, having dimensions of 20×70 mm, five roughness measurements were taken per side, over a distance of 0.25 mm. The test setup is shown in Figure 2.14 with one of the foils. The foils were held in place manually to avoid sliding.

The results are plotted in Figure 2.13. There appears to be no influence of the etching time on the surface roughness. Since most etching would occur at the grain boundaries the surface roughness was expected to be locally highly increased. Naturally mechanical surface roughness tests are limited by the stylus dimensions. Due to the possibly small lateral width of the grooves, in comparison with the stylus radius (10 µm), the stylus was unable to record the actual morphology correctly. Therefore another measurement method was proposed: Atomic Force Microscopy (AFM). Small samples of 15×15 mm each were cut out of the original foils and measured using a Veeco Dimension 5000 with a Nanoscope 5 controller. For the measurements the machine was equipped with a NSC15 Micromasch probe, with a n-type silicon tip having a nominal tip radius of 10 nm. All measurements were done in tapping mode by adjusting the control system gains and the setpoint amplitude sample-wise. Tip velocities were in the range of $2.45 - 16$ µm s^{-1} and tip quality was assessed by using a delta-function grating TGT01 Micromasch reference sample.

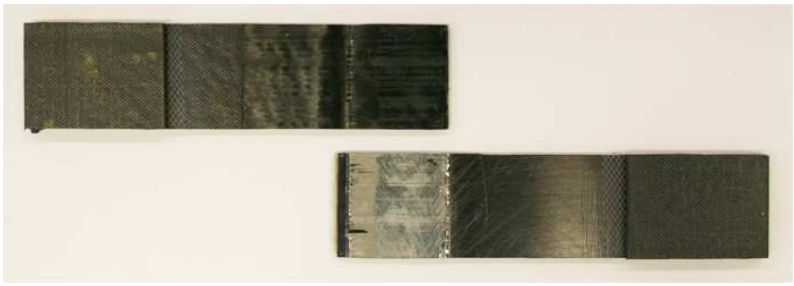

(a)

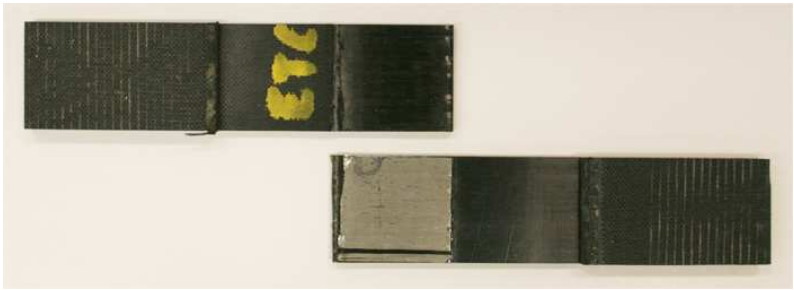

(b)

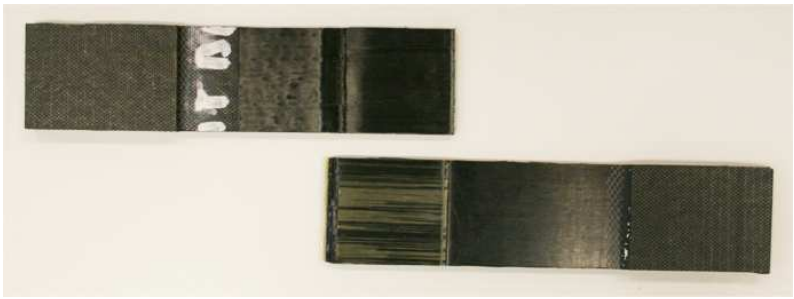

(c)

(d)

Figure 2.12: Failure modes of the lap shear test samples. (a) Interfacial failure in ST3, between the composite and the tungsten (b) Cohesive failure in the thin resin layer of the composite in ST5. (c) Partial cohesive failure in ST2, where partial composite failure and partial interfacial failure have occurred. (d) Adherent failure of the tungsten in ST4.

In tapping mode the tip oscillates at high frequency close to the surface. The surface roughness was obtained by measuring the change in feedback signal of the tip position.

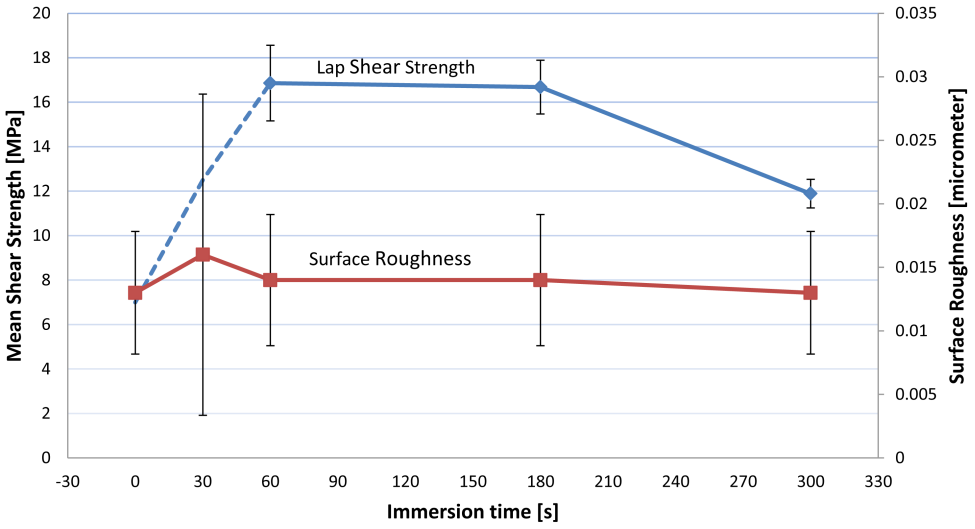

Figure 2.13: The influence of the etching time on surface morphology and lap shear strength. The dashed line gives the expected trend, such that the lap shear strength has exceeded its critical value.

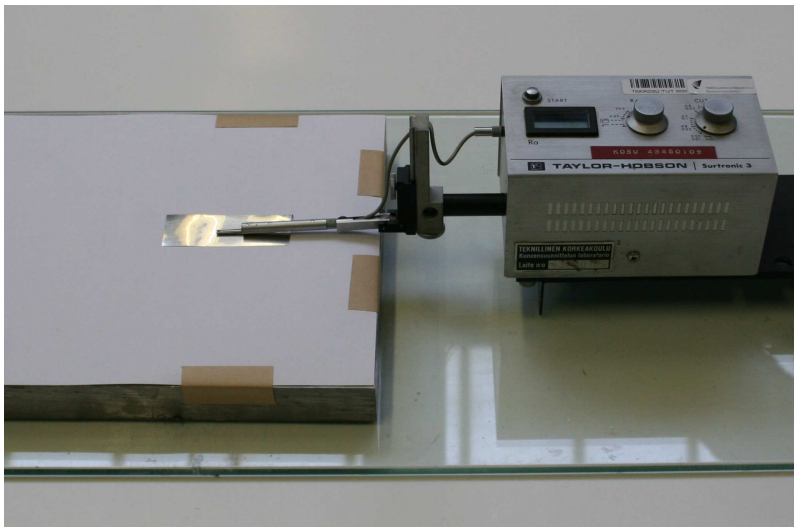

Figure 2.14: Surface roughness test setup featuring a Surtronic 3 device. Measurements were taken over a distance of $0.25\,\mathrm{mm}$.

In order to obtain a constant oscillation amplitude the tip was moved vertically, depending on the tip-surface repulsive and attractive forces. The closer the tip gets to the sample surface the larger the short-range atomic forces become, effectively altering the oscillation amplitude. Since only small parts of the foils could be investigated at the same time no representative surface roughness measurements could be taken, hence limiting the analysis to qualitative analysis only.

Figures 2.15, 2.16 and 2.17 show the influence of the etching time on the surface roughness. AFM images were taken of an area of 8×8 µm. From Figure 2.15 it can already be seen that the initial degreasing, which was done in similar fashion as for the grit blasting

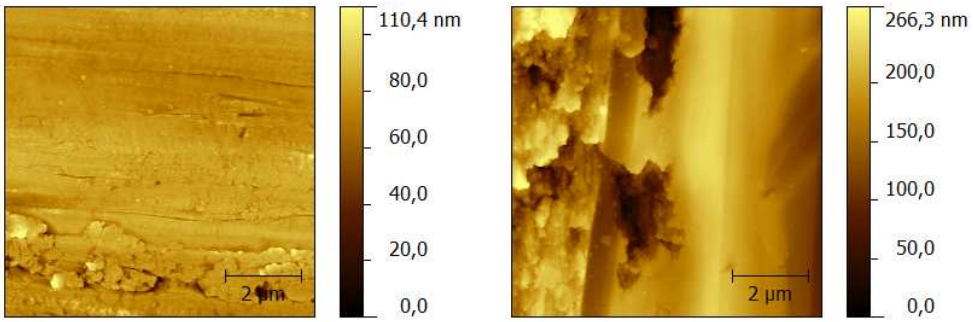

(a) (b)

Figure 2.15: AFM height images of the unetched tungsten foils (a) as was received from the manufacturer and (b) after the degreasing with MEK.

procedure, influenced the surface roughness. Fracture surfaces were identified, which could also be ascribed to handling errors in between the different process steps.

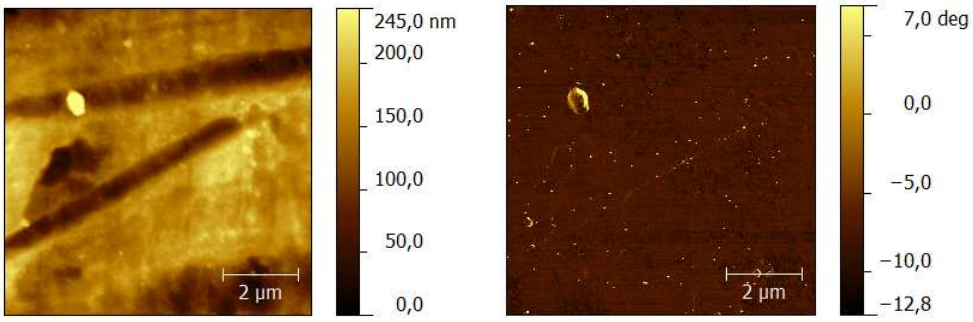

(a) (b)

Figure 2.16: AFM images of the etched tungsten foils for an etching time of 180 s. Both (a) height plot and (b) phase plot are given.

For the etched samples, it was found that the larger grooves, that were generated by the initial abrading, did not experience a significant increase in roughness, whereas the otherwise smooth surface did become rougher with increasing etching time. This can be seen from Figures 2.15, 2.16 and 2.17. It was found that the abrading and etching indeed only led to minor mean arithmetic surface roughness values, when compared to the required $1 - 2$ µm. Therefore the initial assumption of over-etching was discarded.

However, another possible cause for the reduced bond strength was found. From Figures 2.16 and 2.17 it can bee seen that for longer etching times a larger amount of impurities were located around the larger grooves, possibly causing the large bonding strength decrease between the 180 s and 300 s etching times. The chemical composition of the impurities could not be verified by AFM analysis. Whether this material was an oxide layer or whether it were remainders of the etching solution should be verified.

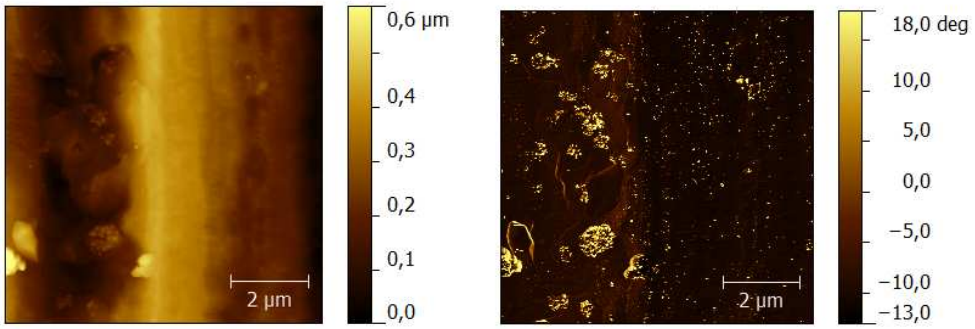

(a) (b)

Figure 2.17: AFM image of the etched tungsten foils, with an etching time of 300 s. Both (a) the height plot and (b) the phase plot suggest an increase of impurities around the grooves.

As the presence of impurities was assumed for foils with larger etching times a surface treatment with an etching time of one minute was proposed for further research. This surface treatment gives a higher lap shear strength than was found for the methods discussed in the literature (five-minute etching and grit blasting).

Coating Deposition Effects

The Diamond-like Carbon coating performed best in the lap shear tests. The application of this treatment is limited by the part size, shape and costs and can therefore not be applied on large scale. The DLC treatment was by far the most expensive option, but was tested to prove its high performance. An unexpected failure mode was found for three of the DLC samples. The tungsten foil itself failed, rather than the tungsten-composite interface. A clean cut was found in in-plane direction, as is shown in Figure 2.18. Tungsten was found on both sides of the fracture surface.

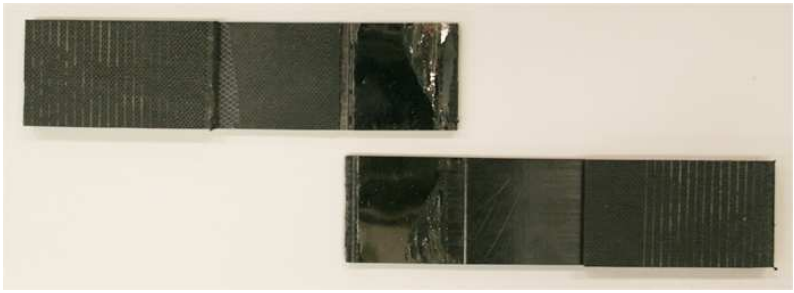

Figure 2.18: A special case of adherent failure was found for the DLC, where the tungsten adherent failed itself, over almost its entire surface.

Similar behavior was found for a tensile strength test specimen. During manufacturing and cutting of the test sample the $(0/45/-45/90/W^{50})_{so}$ laminate, featuring a single DLC-coated tungsten foil, failed cleanly over the entire tungsten foil area. Two half samples, both containing part of the tungsten foil, were left, as is shown in Figure 2.19.

Note that the two halves experienced shape distortions due to the residual stresses, since both halves were asymmetric after failure. Visual inspection revealed that the majority of the tungsten was located on one side, only leaving a thin tungsten layer on the other side. The part with the majority of the tungsten foil is shown in the back of Figure 2.19.

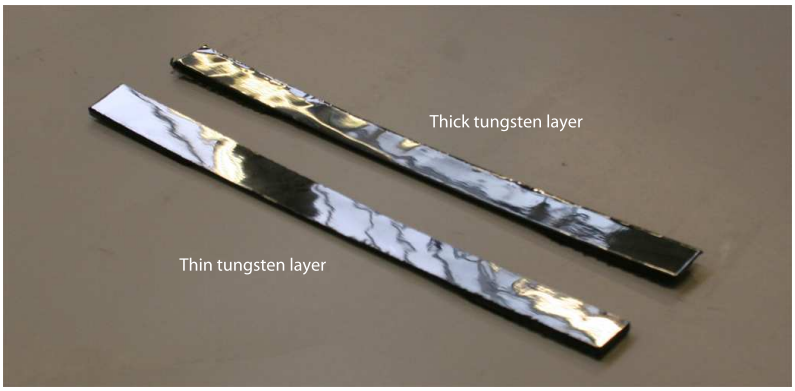

Figure 2.19: In-plane DLC-coated tungsten failure experienced during manufacturing in a tensile strength test sample.

Upon deposition of the DLC coating residual compressive stresses are generated in the coating layer. In order to counterbalance the compressive stresses tensile stresses were located in the tungsten substrate. If the tungsten is unable to counterbalance the compressive stresses, due to a too low ultimate tensile strength, the substrate will fail [43]. The exact fracture locus is dependent on the combination of stress contributions of the cold-rolling process, the coating deposition process and the curing cycle and its resultant thermal stresses. Furthermore tungsten defects can lead to fracture onset.

In the pure tungsten foil pores and defects were found. If the coating is applied over those defects the stress field around the defect is altered. Post-cure thermal stresses can cause fracture propagation at those locations and peeling of the coating. The peeling could possibly be caused by blister formation. In case of large driving forces for debonding fracture will occur within the substrate, rather than at the coating-substrate interface [44, 45]. Along with the coating also part of the substrate is peeled off, resulting in a step-like shape in the substrate surface, at the location of the defect. This was also found by AFM inspection. The substrate peeling was found to start at the defects and end at a certain distance. This is shown in Figure 2.20. Note that Figure 2.20 is made for the part with the thin tungsten layer. As such the remainder of the peeled-off material is given here as an increase in height. The directionality of the step-wise height differences, which all were oriented in the same direction, could be caused by the directionality of the grains in the tungsten. In the cold-rolling process the grains were elongated in rolling direction, leading to anisotropy.

The exact depth at which the fracture occurs is unknown. Further investigation on the fracture mechanics and the failure modes is required. With the manufacturing steps described in this thesis the DLC coating was assumed not to be applicable to tungsten foils and was therefore discarded for real applications. With possible alterations in the manufacturing process, such as a reduced DLC coating thickness or lower curing temperatures in order to reduce compressive stresses in the coating layer, the adhesion strength of this coating could potentially be improved.

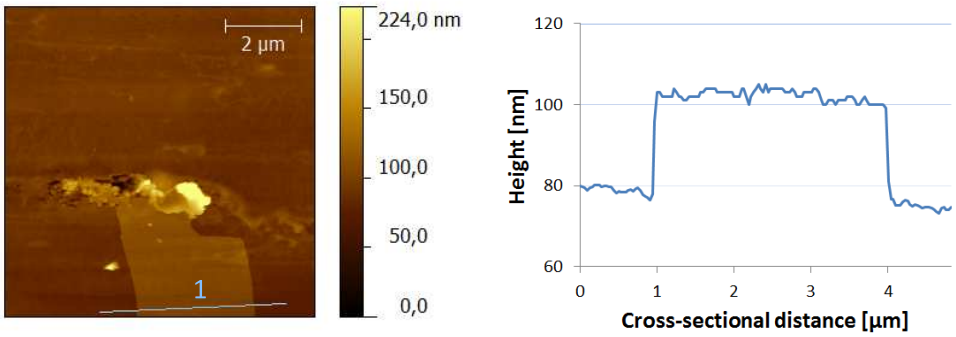

(a) (b)

Figure 2.20: AFM image of the failed DLC-coated tungsten foils. (a) The substrate peeling was initiated around a defect, causing a step-wise decrease in height. (b) A cross section over line 1 validated the step-shape.

Grit Embedment

The lowest lap shear strength was found for the grit blasting treatment ST2 (15.15 ± 1.49 MPa). Apart from the low mean shear strength large standard deviations were obtained due to the uncontrollability of the treatment and the application of the primer. The non-homogeneity and the resulting stress distribution give rise to the occurrence of partial cohesive failures.

Radiation test samples were manufactured, using the same grit blasting technique, as will be discussed in more detail in Section 3.4. Visual inspection of the grit blasted foils showed a larger thickness for the tungsten foil than for the steel foil, whereas the initial thickness was equal for both (0.05 mm). However, for reliability of the radiation results the exact thickness and composition of each layer should be known. The influence of the grit blasting procedure is dependent on several factors: Grit size, substrate and grit material and their respective hardness, blasting pressure (or particle momentum), distance and angle, operator skills and number of passes. Due to the large number of parameters the effect of the grit blasting is hard to estimate. Parametric investigation is required for the specific materials used.

Based on the apparent thickness difference weight measurements were performed. Nine tungsten foils (20×20 mm), which were part of the same grit blasting batch as the radiation test samples, were weighed, with an AS 220/X scale (error $e = 1$ mg, deviation $d = 0.1$ mg). Moreover their surface area was measured ($e = 0.01$ mm). Similar analysis was done for the steel foil. The results are shown in Figure 2.21. A mass gain of 19.84% was found for the tungsten foils, whereas the steel experienced a mass loss of 3.88%, as was expected due to the abrasion. In Figure 2.21 the mass was normalized by the factor A/ρ, where A is the surface area, in order to achieve equivalent foil thicknesses. The tungsten's mass increase can be explained by the embedment of grit particles.

F100 alumina grit, with a Knoop hardness of 2,000, will tend to produce plastic deformation in the softer tungsten material, with an estimated Knoop hardness of 318 [46]. Polished surfaces like the tungsten foils first experience particle embedment and surface roughening prior to erosion, leading to a large incubation time before a steady-state ero-

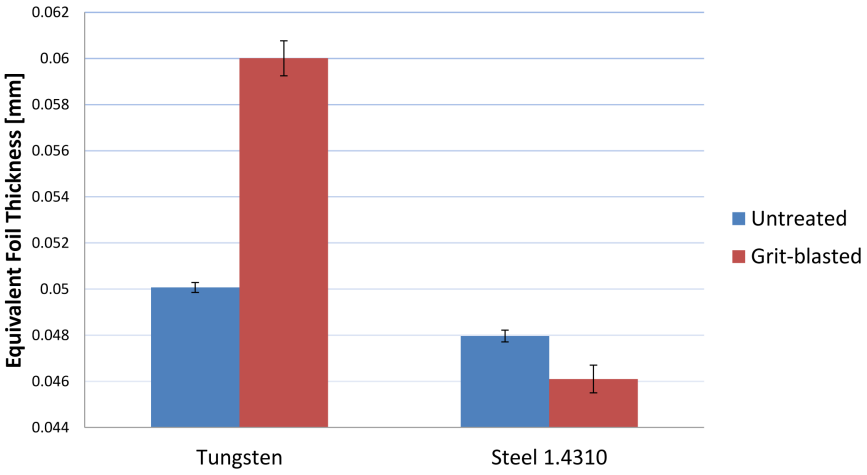

Figure 2.21: A mass gain was found for tungsten after the grit blasting treatment, due to grit embedment. The mass gain can be converted to equivalent foil thicknesses, which describe the pure foil thickness required to achieve the same mass.

sion rate can be achieved. The particle velocity at which plastic deformation occurs is given by Equation 2.2 [47]:

$$v_c \propto \frac{J^2 \cdot H_t^{2.5}}{\sqrt{\rho}} \tag{2.2}$$

$$J = \frac{1-\nu_t^2}{E_t} + \frac{1-\nu_p^2}{E_p} \tag{2.3}$$

The subscripts indicate the material, where t indicates the target material and p indicates the particle material. This shows that target materials with lower hardness, H_t, will have a lower velocity limit, such that plastic deformation will occur at an earlier stage than for harder materials. Also with an increase in Poisson's ratio ν or Young's Modulus E the critical velocity v_c will decrease. The presence of grit particles was shown by means of Energy Dispersive Spectroscopy analysis (EDS) and secondary electron imaging and backscatter imaging was done on two of the unabraded and two of the grit blasted tungsten foils. Analysis was done with a LEO 1450 15 keV Scanning Electron Microscope (SEM). By focusing an electron beam on the target material characteristic X-rays will be generated, indicating the elemental composition of the target.

Figure 2.22 shows respectively the backscattering images of the unabraded and the grit blasted foils. In the figure the darker marks indicate materials with lower densities. The unabraded foil showed a small quantity of impurities/inclusions with low densities.

EDS analysis of the clean unabraded tungsten surface indicated the presence of carbon, oxygen and germanium, which can be ascribed to the initial impurity of the industrial-grade tungsten foil. Similar analysis for the inclusion showed the presence of a large quantity of carbon, oxygen, zirconium, cobalt and titanium. These were also ascribed to initial impurities. The presence of the zirconium can be disputed, due to the similarity in characteristic energy levels for tungsten and zirconium. Figure 2.22 shows one of the

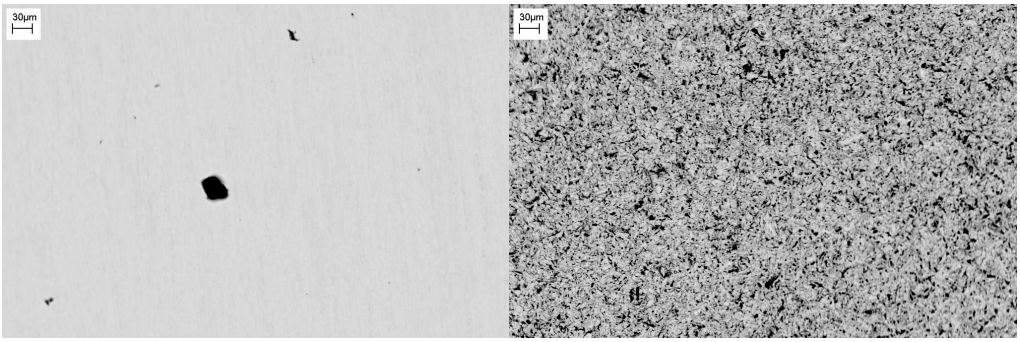

(a) (b)

Figure 2.22: Backscattering image (a) of an unabraded tungsten foil, showing a small inclusion/impurity with a smaller density and (b) of a grit blasted tungsten foil, showing a large quantity of embedded particles. The scale bar indicates a distance of 30 µm.

larger impurities in the unabraded foil. The impurities were rare and located at large distances from each other, as can be seen from the secondary electron scattering image of Figure 2.23.

Figure 2.23: Secondary electron imaging of the unabraded tungsten foil, showing almost no impurities/inclusions. The lines/scratches were ascribed to handling errors. The scale bar indicates a distance of 30 µm.

Table 2.8 shows the typical analysis of white F100 Duralum alumina grit. These elements were expected to be found embedded into the tungsten after grit blasting.

EDS of the larger inclusions, shown in Figure 2.24, in the grit blasted foil showed the presence of germanium, carbon, oxygen and zirconium, as was found in the inclusions of the untreated foil. However, in this case also small quantities of calcium, nitrogen, sodium, aluminum and sulfur were found. The aluminum and sodium were ascribed to the grit particles. However, the nitrogen, calcium and sulfur must originate from a

Chemical	Composition [%]
Al_2O_3	99.77
Na_2O	0.20
SiO_2	0.02
Fe_2O_3	0.01

Table 2.8: Typical analysis of white F100 Duralum alumina grit

different source.

Investigation of the smaller inclusions showed an even more diverse elemental spectrum, containing chlorine, magnesium, iron, zinc and potassium. Large peaks for both aluminum and oxygen were found, such that the presence of embedded alumina particles was confirmed. The particles that could neither be attributed to the tungsten foil impurities nor the grit blasting particles were ascribed to an external source, such as contaminations from previously-used and recycled grit.

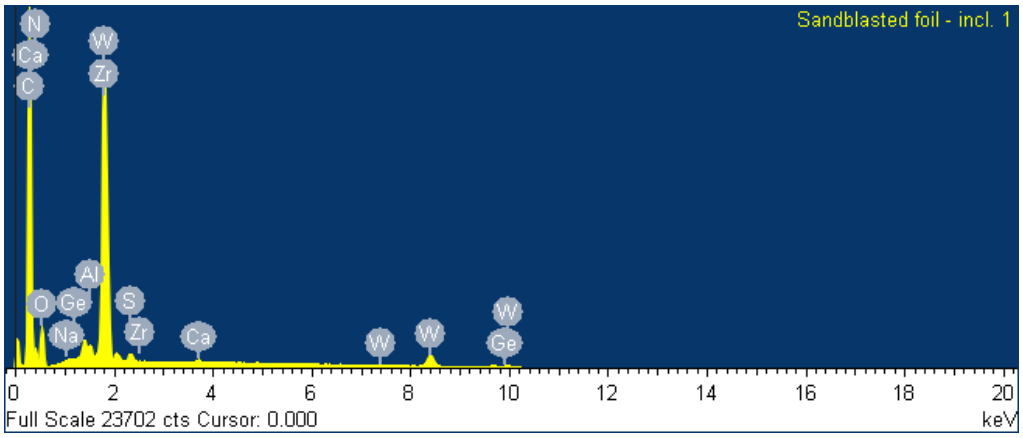

(a)

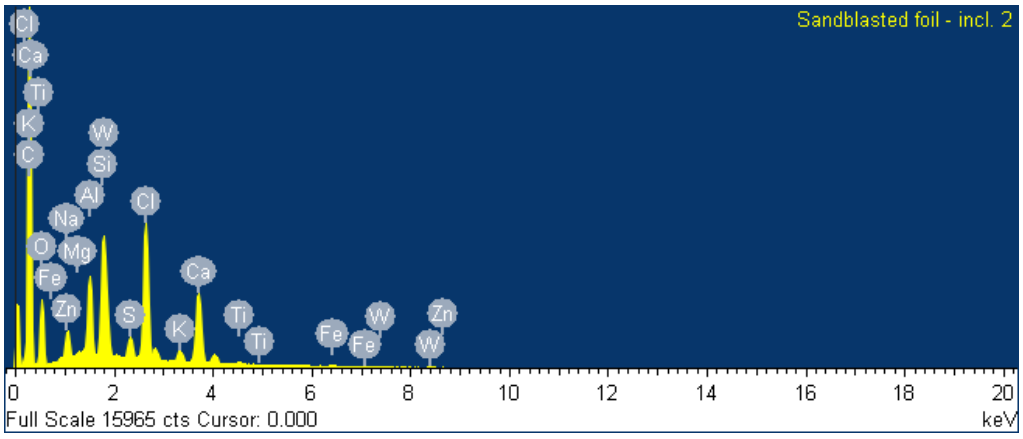

(b)

Figure 2.24: Energy dispersive spectroscopy (a) of a larger inclusion in the grit blasted foil, containing large quantities of carbon and oxygen and (b) of a smaller inclusion, showing large quantities of both aluminum and oxygen.

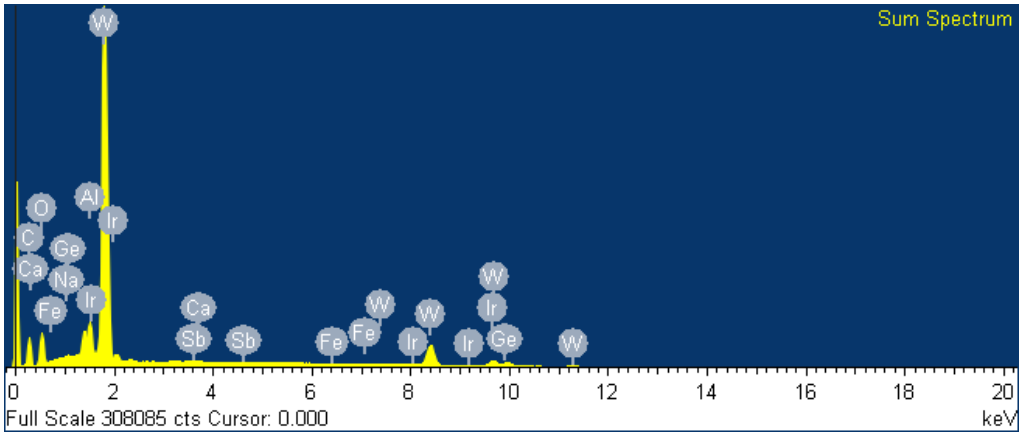

Figure 2.25: Energy dispersive spectroscopy of the elemental map for the grit blasted foil. The presence of both tungsten and alumina were observed.

An elemental map of a surface was created, giving the distribution of different elements for the entire area, where the individual elements are highlighted in their respective locations. The EDS analysis and elemental map of the larger area are shown in Figures 2.25 and 2.26 respectively. The map shows the locations for respectively tungsten, carbon, oxygen and aluminum. EDS analysis, shown in Figure 2.25, showed large quantities of tungsten and significant quantities of carbon, calcium, oxygen, sodium and aluminum. All of these elements can either be found in the original tungsten foil or in the alumina grit. The locations of the aluminum correspond to the locations of the oxygen, as can be seen from the red indicators. The larger inclusions were again found to be carbon, which is shown in blue.

Due to the mass gain and uncontrollability the grit blasting treatment was dismissed for further research. Costly parametric investigation of the grit blasting parameters would be required to limit the grit embedment. As such the one-minute chemical etching proved to be the best choice.

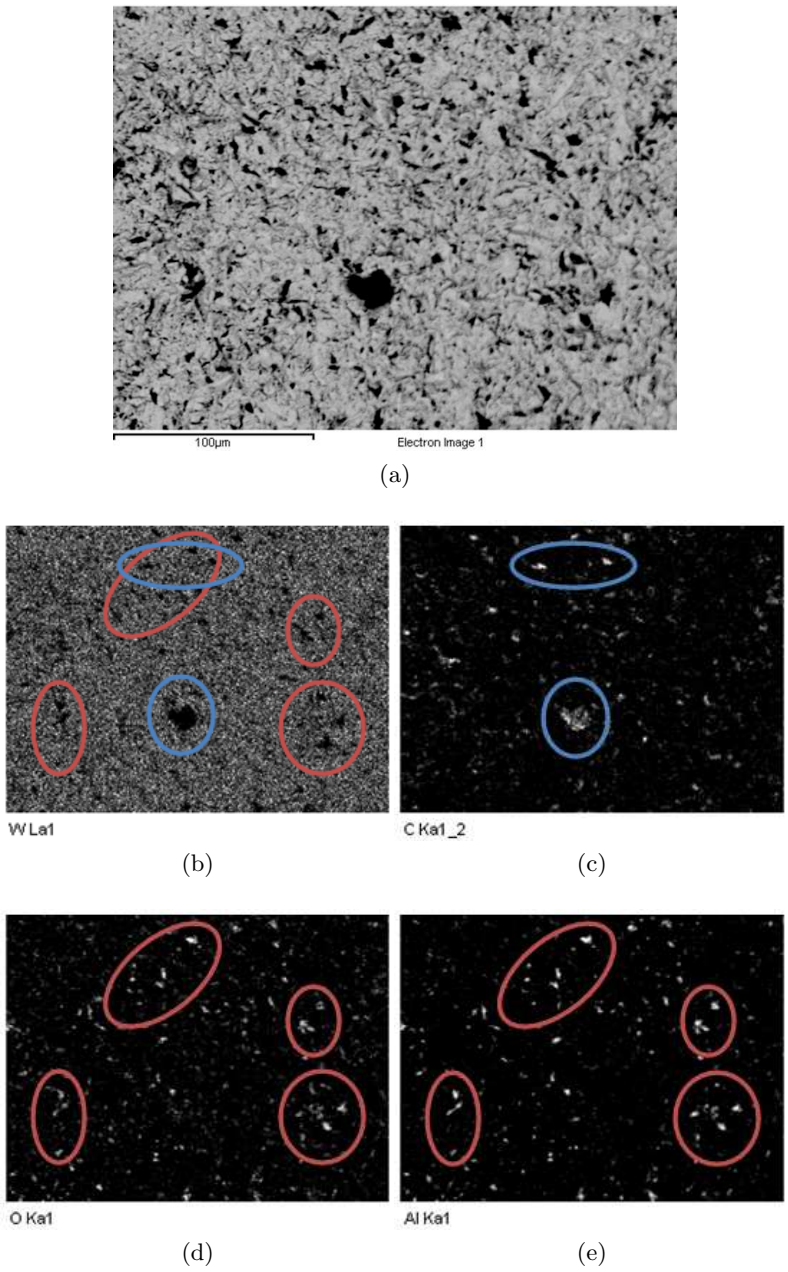

(a)

(b) (c)

(d) (e)

Figure 2.26: (a) Backscattering image of the measured area and areal elemental mapping of a grit blasted tungsten foil for respectively (b) tungsten, (c) carbon, (d) oxygen and (e) aluminum. White spots indicate the presence of the respective element. The red shapes indicate the corresponding locations of aluminum and oxygen, such that the assumption was made that alumina is embedded at those locations.

Chapter 3

Design Methodology

The objective of the design method is to optimize the top panel of an electronics housing structure, with respect to mass, as was shown in black in Figure 1.1. In order to do so a design methodology needs to be generated. The proposed design methodology is discussed in this chapter.

The panel can be described as a laminate with simply-supported edges. The to be optimized laminate is subject to a large number of constraints. The overall model is shown in Figure 3.1.

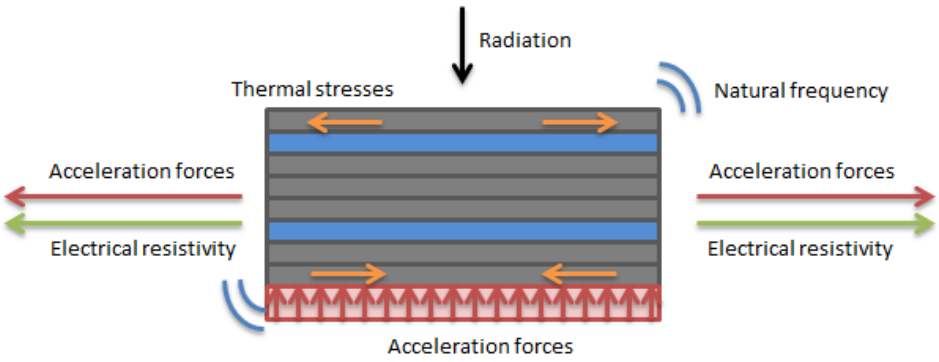

Figure 3.1: The laminate model of the top panel, which is subject to a number of constraints.

This chapter describes the optimization routine and treats the theoretical models that were applied. Furthermore a validation of the theoretical models was provided by means of testing. Section 3.1 summarizes the constraints and objective functions, whereas Section 3.2 describes the overall optimization routine. Thereafter the individual constraints are discussed and an analysis of the theoretical models is made, based on obtained test results. The constraints are discussed in order of assessment during the optimization process.

3.1 Optimization Problem Statement

For the optimization procedure, where the mass of an electronics housing structure panel is minimized, a set of constraints are given. The objective function of the minimization of the mass m can described as a function of the overall configuration vector x_c. The configuration vector consists of the number of layers, their respective properties and the stacking sequence in which they are placed.

$$\min m(x_c) \tag{3.1}$$

A secondary objective is the induced shape distortion $\Delta\Pi$, which is a function of both the overall configuration vector x_c and the lay-up orientation vector x_l. This objective function is discussed in more detail in Section 3.8. The lay-up orientation vector x_l consists of the lay-up angles of the anisotropic carbon fiber plies.

$$\min \Delta\Pi(x_c, x_l) \tag{3.2}$$

The objective functions are subject to the following constraints:

- Practical limitations
  - The material choice is limited by availability and costs.
  - The outer layers are required to be composed of composite materials, for manufacturing reasons.
  - The application of adhesives is discarded in order to limit the number of materials and manufacturing steps.
  - The fiber lay-up angles are limited to multiples of 15°.
- Radiation attenuation
  - The Total Ionizing Dose and Non-Ionizing Dose in 300 µm silicon should be smaller behind the to be designed shielding than for 2 mm of Al-2024-T3, for both LEO and GEO.
  - The application of steel and gadolinium is restricted. Steel is never placed behind tungsten and gadolinium is never placed in front of tungsten, for design purposes.
- Natural frequency
  - The transmissibility ratio (also response-input ratio) should be smaller than unity in order to avoid vibrational resonance.
- Structural integrity
  - The maximum deflection in z-direction as a result of the acceleration load in z-direction is required to be smaller than would be found for 2 mm of Al-2024-T3.

  - A positive Margin of Safety is required under acceleration loads, in x-, y- and z-directions.

- Electrical resistivity
  - The panel is required to provide a to be determined electrical conductivity in x-, y- and z-directions.

The solution space is limited by a number of manufacturing and design limitations. Note that the discarding of the application of adhesives intrinsically means that the metallic layers could not be placed directly abreast.

3.2 Optimization Routine

The optimization routine consists of two sequential minimization functions for mass and induced shape distortions and will be discussed in more detail in this section. The minimization for induced shape distortions can be done in two ways, depending on the optimization problem and will both be discussed in this section.

Due to the large computation time for each of the analysis modules the total solution space was limited to a restricted subspace. A smart optimization process was required to include all relevant solutions in the solution's subspace. The evaluation of the first objective function is shown in Figure 3.2. In the first phase of the optimization process the radiation attenuation properties are assessed. First the GEO constraints regarding the TID and NID are checked, after which the LEO constraints are assessed. The radiation attenuation properties are independent of the lay-up orientation vector x_l and are therefore assessed before the other constraints. While limiting the computation time, this method does *not* affect the solution space.

For manufacturing reasons the outer layers are required to be composite material. As such the most lightweight solution consists of a single carbon fiber composite ply, which is used as initial guess for x_c. Whenever the radiation constraints are not satisfied the next configuration, sorted by the areal density, is evaluated. Note that the increase in mass for different configurations can be attributed to either an increase in total number of layers or to the interchanging of materials.

After the first optimization loop the configuration vector is set, resulting in a mass-minimized configuration. With the first objective function being satisfied the structural and electrical constraints are analyzed and evaluated for the initial guess of the lay-up orientation vector x_l. For all composite plies that are introduced in the process an initial lay-up orientation x_l is assumed to consist of alternating 90° and 0° layers, symmetric around the midplane (discarding the metallic layers for the moment), such that the structure starts out with reasonable strength and stiffness in both principle in-plane axes. As a result, in case the number of carbon fiber layers is not a multiple of four, the majority of layers is oriented in y-direction, which is chosen to have the largest dimension.

The analysis and evaluation of the different constraints consists of a number of subsequent steps:

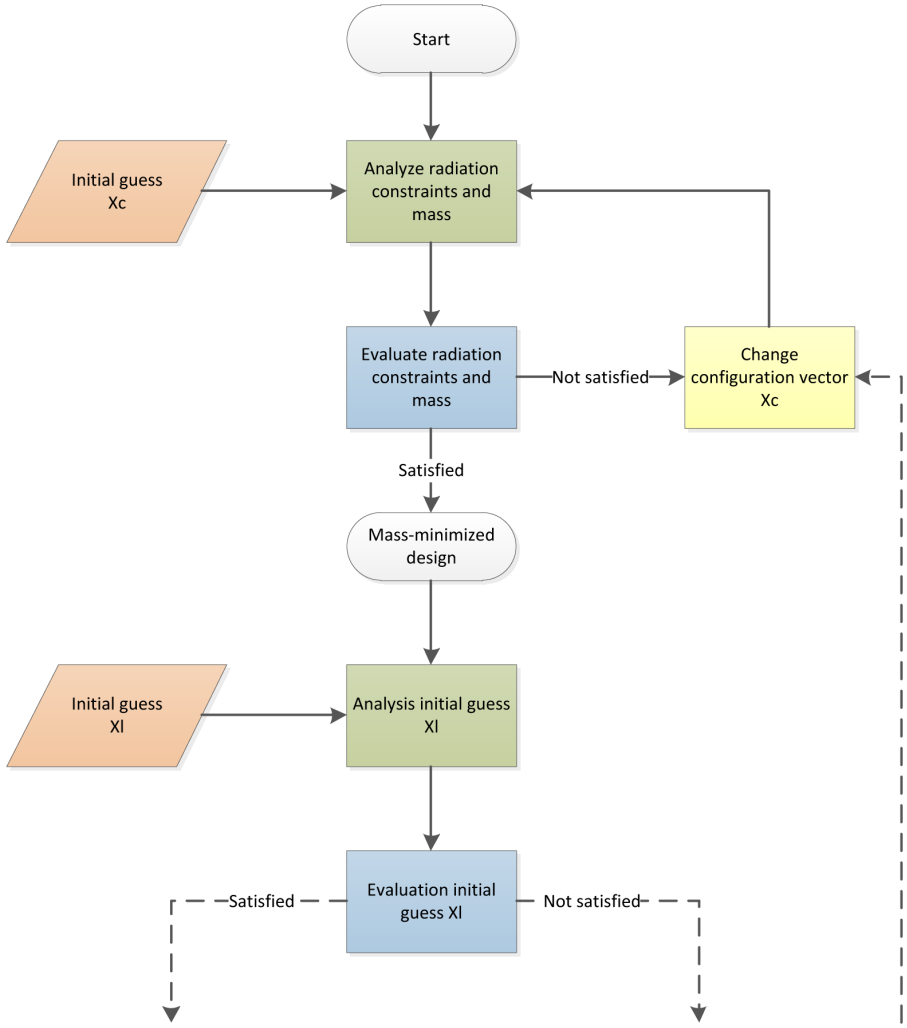

Figure 3.2: The applied mass-minimization routine

- Natural frequency
- Deflections as a result of acceleration loads in z-direction
- Structural integrity as a result of acceleration loads in x-, y- and z-direction
- Electrical resistivity in x-, y- and z-direction

If all constraints are satisfied by the laminate with the initial guess for x_l the structure is assumed to be overdimensioned. In this case large freedom is gained w.r.t. the fiber lay-up angles, such that the structure can be optimized w.r.t. induced shape distortions to a large extent and the deformation optimizer can be initiated directly. If not all constraints are satisfied this freedom in lay-up orientation vector is not obtained and the solution space will be restricted. The different optimization methods for the minimization of induced shape distortions for both cases will be discussed in the coming sections.

3.2.1 General Structures

If the configuration with the initial guess for the lay-up orientation vector x_l does not satisfy all the constraints the structure is assumed to be a general structure. The minimization of the induced shape distortions and the large set of constraints might have contradicting objectives w.r.t. the lay-up orientation vector. Therefore the fiber lay-up cannot be altered as freely as in the overdimensioned case. First another set of steps, as shown in Figure 3.3, is required before the deformation optimizer can be applied.

In order to ensure that the constraints will be satisfied the lay-up orientation vector x_l is first adjusted such that the constraints are met. If the constraint under investigation is not satisfied a change in lay-up orientation vector x_l is required. The way in which the lay-up vector is altered depends on the constraint. If an alteration in lay-up vector is made the entire set of constraints, which are dependent on x_l, are reassessed. In case it proves to be impossible to satisfy the constraints by changing only the lay-up orientation vector also a change in the overall configuration vector x_c is required, inherently changing the mass, and the whole routine starts all over again.

Since the structure was assumed to be vibration-critical the natural frequency is assessed first. The bending stiffness and thus the natural frequency is most affected by the layers located furthest away from the center line, such that if the natural frequency constraint is not satisfied the outer layers are changed first. If the constraints are still not satisfied the layers closer to the center line are altered, to maximize the natural frequency. This process is referred to as layerwise optimization [48].

Similarly the structural integrity is assessed. First the deflections in z-direction, as a result of acceleration loads in z-direction, are assessed. Since this parameter is coupled to the out-of-plane stiffness, just like the natural frequency, it is checked subsequently. The same layerwise optimization routine is applied.

For the load responses, if a negative Margin of Safety is found and hence the structure would fail under the acceleration loading, the critical layer is turned 15° more in the principle load direction. If this alteration is proven insufficient additional changes are made to the overall lay-up orientation vector. The structural response to the loading is analyzed and evaluated in all three principle axes.

The electrical resistivity is independent of the location of the individual plies in z-direction. If necessary more composite material layers are turned in the required direction. If the electrical resistivity is not sufficient after adjusting the fiber lay-up orientation to the maximum extent a different overall configuration and hence a change in x_c is required. In order to avoid contradicting objectives with the out-of-plane constraints, the internal layers are rotated first for the electrical resistivity constraints.

Once all constraints are satisfied the second objective function can be minimized. Due to residual thermal stresses asymmetric laminates may experience post-cure shape distortions, due to a release of strain energy. This is discussed in more detail in Section 3.8. The extent to which the laminate experiences shape distortions should be minimized for assembly reasons. For the general case a steepest descent method is proposed. Figure 3.4 shows a schematic representation of the minimization routine of the second objective function.

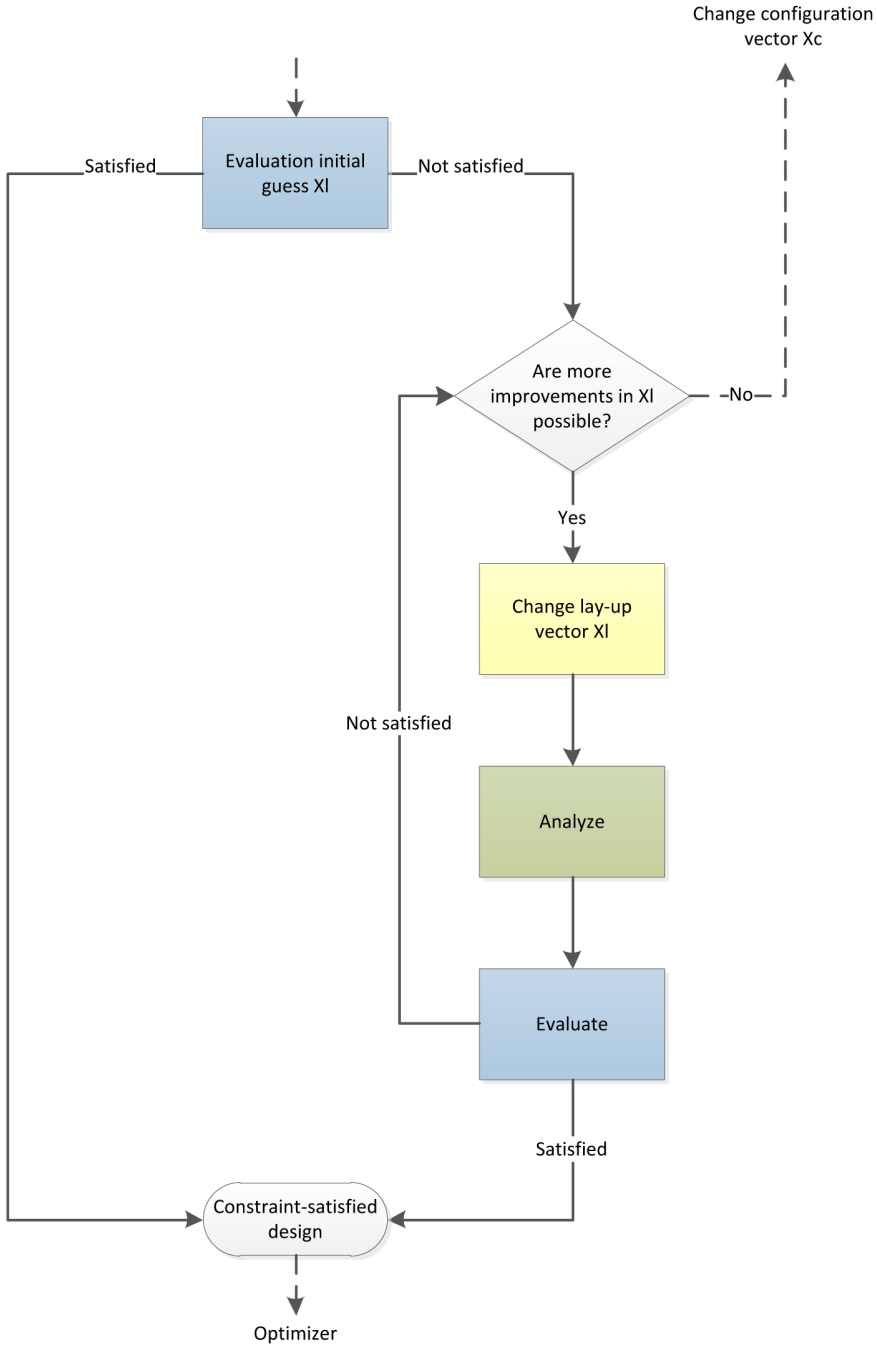

Figure 3.3: The influence of the initial guess on the applied steps of the routine.

The optimizer starts off with the lay-up orientation vector of the constraint-satisfying design. Each layer is rotated individually to all possible configurations. This is done separately for each individual layer, such that a total of k (number of composite layers) times b (number of possible ply angles) combinations are assessed for their potential energy decrease, for each input vector (or parent). The modified solutions (or children) have their own potential energy decrease w.r.t. the reference curing shape, which is assumed to be

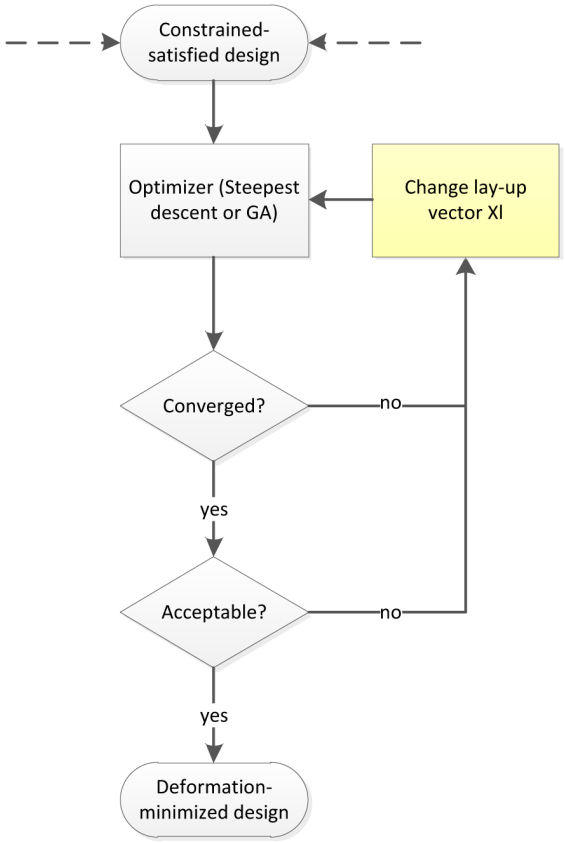

Figure 3.4: The applied optimization routine for the minimization of induced shape distortions.

the measure for the induced shape distortions.

For the steepest descent method only the solution with the best fitness value will become a parent for the next generation, limiting the amount of parents in each generation to one. The constraints will be analyzed and evaluated for the child with the best fitness value. In case the constraints are not fulfilled the child with the next best fitness value will be investigated, until a child which satisfies all constraints is found. This child then becomes the parent for the next generation. As soon as the fitness value does not improve any further for the subsequent generation of solutions, without having to dissatisfy any constraints, a deformation-minimized design is found.

3.2.2 Overdimensioned Structures

In case all constraints are already met by the initial guess for the fiber lay-up vector x_l, the vector is assumed to be highly variable, without necessarily exceeding any constraints. This freedom can be used for the reduction of induced shape distortions even further than for the steepest descent method, as was proposed in Section 3.2.1. For the overdimensioned case a new optimization routine was proposed. As a result of the large number of local minima general optimization methods are not very effective in finding good solutions. Gradient descent methods look for the steepest gradient and as such get stuck in

one of the many possible local minima. Therefore the proposed method investigates *all* solutions, which have a negative gradient.

The proposed optimization routine commences with the initial guess for x_l. This solution is the parent in the first generation of solutions. For all parents the same layerwise lay-up change is applied as for the steepest descent method, resulting in k times b children. Every child that has a better fitness function (and hence experiences less warping) than its respective parent survives and becomes a parent for the next generation of solutions. If the opposite is true it dies and as such will not become a parent.

Since every parent could have up to $k \times b$ children the number of parents largely increases with each generation. However, each branch of the family tree dies out as soon as a local minimum is found, reducing the total number of children in later generations. Furthermore only unique parents are investigated, such that the potential doppelgangers are discarded. Also the fiber orientation conjugates are eliminated since it would result in similar potential energies, based on the symmetry of the plate in two directions. Once all family branches have died out the local minima are compared and the configuration with the best fitness function is chosen. In order to verify the found solution is also the global minimum a full investigation of the total b^k solutions would be required.

The potential energy is determined by numerically solving for the 28 unknowns, as is discussed in Section 3.8. As initial guess for the numerical solver the values for the displacement coefficients of the previously-assessed child are used, highly reducing the computation time. Whenever the solver finds a maximum or gets stuck in a local minimum a new set of 28 coefficients are chosen randomly with values ranging between -1 and 1.

After assessment of the induced shape distortions the solutions are sorted by their respective fitness values. The large number of constraints are analyzed and evaluated for the solutions with the best fitness values and hence the smallest amount of shape distortions. If any of the constraints is dissatisfied the next best solution is analyzed and evaluated, until a solution is found, which satisfies all constraints.

The advantage of this optimization routine is the high quality of the obtained solution. The optimization routine evaluates a large number of possible combinations for their respective shape distortions and avoids a large amount of local minima. However, the proposed gradient-based genetic algorithm routine is not applicable to general structures, since a change in lay-up vector x_l will most likely cause a dissatisfaction of one of the constraints. With the large computation times for each of the analysis modules, the large amount of possible configurations which have to be investigated until a constraint-satisfying design is found, can no longer be analyzed and evaluated within a reasonable time frame.

3.3 Material Selection

The mass optimization of the structural panel is restricted by a set of practical limitations, such as material availability and costs. In order to limit the entire solution space a material selection was made before the optimization. The selection was based on structural and thermal properties, as well as costs. The material trade-off is discussed in this section.

3.3.1 High-Z Material

For optimum radiation attenuation a combination of materials with high and low atomic numbers Z was required, as was discussed in section 2.1.4. In the high-Z domain nine metals are found, with atomic numbers ranging from 72 to 80. All high-Z metals are solid, apart from mercury, at standard conditions. A further four materials (rhenium, osmium, iridium and platinum) were eliminated based on foil availability. Foils of sufficient dimensions for the practical application for electronics housing structures were required. Furthermore hafnium, which is known for its good neutron absorption, is only found in nature in combination with zirconium. Due to their chemical resemblance the materials are hard to separate, leading to large impurities in hafnium foils.

The remaining high-Z materials (tantalum, tungsten and gold) were compared based on mechanical and thermal properties. For vibration-critical panels the ratio $E^{1/3}/\rho$ is the most important factor, whereas the specific strength (σ/ρ) and specific stiffness (E/ρ) are important for in-plane strength and vibration characteristics [49]. These factors were normalized with respect to the material's density to minimize the mass. Furthermore the linear coefficient of thermal expansion α is of importance for residual post-cure shape distortions. From Table 3.1 it becomes clear that tungsten outperforms gold and tantalum in all critical properties.

Parameter	Unit	Value		
Material		Tantalum	Tungsten	Gold
Specific strength, σ_{ult}/ρ	$\text{MPa g}^{-1}\text{ cm}^3$	16.58	50.78	6.21
Specific stiffness, E/ρ	$\text{GPa g}^{-1}\text{ cm}^3$	11.17	20.73	4.00
Vibrational stiffness, $E^{1/3}/\rho$	$\text{GPa}^{1/3}\text{ g}^{-1}\text{ cm}^3$	0.34	0.38	0.22
Thermal Expansion, α	10^{-6} K^{-1}	6.3	4.5	14.4

Table 3.1: High-Z material properties. Data obtained from [46].

Two novel concepts are proposed in Section 3.4, featuring additional layers of other materials. For the first novel design concept gadolinium was included. Gadolinium is the element with the largest neutron absorption cross section σ. The cross section is a measure of the likelihood of an interaction between two particles. Secondary neutrons are generated upon the impact of protons. The neutron cross section of gadolinium is $2.11 \cdot 10^5$ times larger than that of aluminum and hence the most effective material for stopping secondary neutrons.

3.3.2 Mid-Z Material

For the other novel concept a mid-Z layer is introduced for the improvement of gamma absorption in high-energy electron-rich environments. For the mid-Z layers steel 1.4310 foil was used, based on direct foil availability. Since this concept has not previously been investigated in literature a general mid-Z layer was sufficient to validate the performance. As was done for the high-Z material a trade-off could be made for the mid-Z material: For atomic numbers 39 to 71 the elements with higher atomic numbers were too abundant and hence too costly. Based on costs and mechanical and thermal properties the application of

molybdenum was proposed for future studies. Molybdenum is, just as tungsten, a group 6 element, which are known for their high melting points.

3.3.3 Low-Z Material

With the investigation of radiation attenuation properties of composites being the main goal of the SIDER project composite materials were used as low-Z materials. The application of composites for radiation attenuation has already proven to lead to potential weight savings [1, 5, 31]. Based on the previous AED-studies the electronics housing structure was assumed to be vibration-critical, such that the ratio $E^{1/3}/\rho$ was maximized.

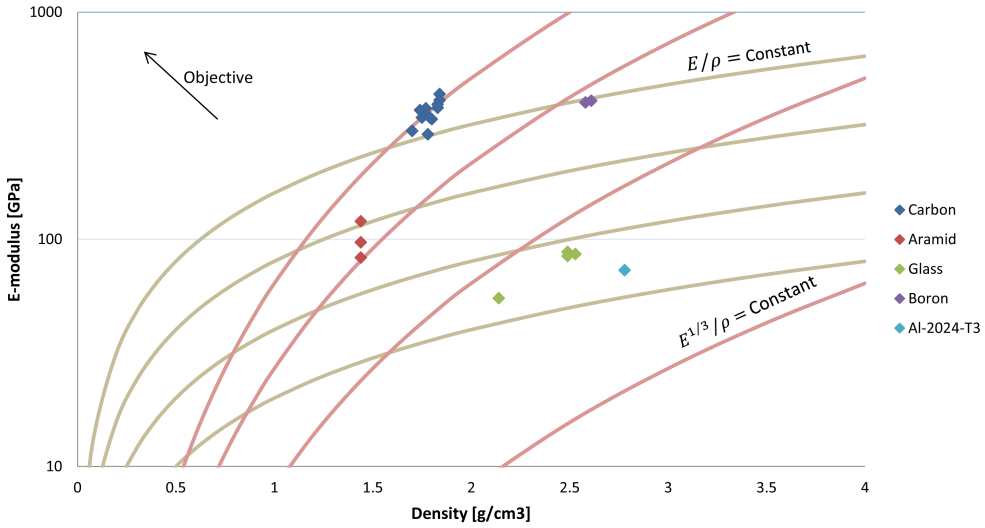

Figure 3.5: Performance characteristics of different fibers for specific stiffness and vibrational stiffness. Data obtained from [50].

The highest out-of-plane stiffness was obtained with high-E carbon fibers, while at the same time limiting the costs and having a good specific strength (of approximately 2.5 GPa g^{-1} cm^3). The high performance of carbon fibers can be seen from Figure 3.5, where the solid lines indicate isoperformance lines.

It can be seen from Figure 3.6 that material costs rapidly increase with elastic modulus. In order to obtain an economically viable design solution ultra-high modulus carbon fibers ($E > 440$ GPa) were omitted (indicated by 'HM' in Figure 3.6). Based on stiffness properties, costs and prepreg availability a M40J carbon fiber with MTM57 epoxy matrix composite prepreg was selected.

The fiber areal density $\bar{\rho}_f$ was given to be 300 g m^{-2}, resulting in a fiber mass fraction of 68%. The material data of both the prepreg and the metallic layers are presented in Appendix B. The cured layer thickness of the composite ply t_{ply}, was determined, as a function of the fiber volume fraction $\hat{v}_f$ and areal density $\bar{\rho}_f$. In Equation 3.3 subscripts f and m indicate the material properties of the M40J fiber and the MTM57 matrix,

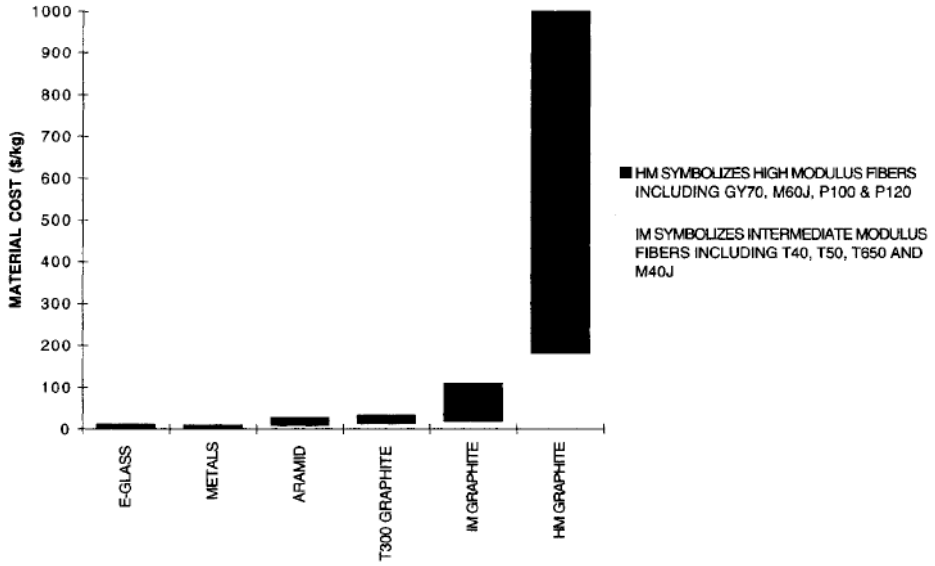

Figure 3.6: Costs of various composite materials. After [51].

respectively. The mass fraction is given by $\hat{m}$.

$$\hat{v}_f = \frac{\frac{\hat{m}_f}{\rho_f}}{\frac{\hat{m}_f}{\rho_f} + \frac{\hat{m}_m}{\rho_m}} = 0.59 \tag{3.3}$$

$$t_{ply} = \frac{\bar{\rho}_f}{\rho_f \cdot \hat{v}_f} = 0.285 \cdot 10^{-3} \text{ m} \tag{3.4}$$

The available plies for the optimized structure are summarized in Table 3.2. For the optimizer the ideal thicknesses and areal densities are used, since the grit blasting procedure, which led to nonideal properties, was discarded from the manufacturing process. The selected materials were only available in specific thicknesses, reducing the optimization routine to a discrete optimization problem.

Material	Thickness t [µm]	Areal Density $\bar{\rho}$ [g cm^{-2}]
M40J/MTM57	285.2	0.0441
Tungsten	50.0	0.0965
Tungsten	100.0	0.1930
Steel 1.4310	50.0	0.0395
Gadolinium	25.0	0.0198
Gadolinium	75.0	0.0593

Table 3.2: The available materials for the optimization routine.

3.4 Radiation Analysis

Due to the high complexity of the radiation attenuation processes, as was discussed in Section 2.1, it is of importance to validate the accuracy of the radiation analysis, by means of radiation testing. First the radiation causes are discussed, after which the test results are given. The dose that is absorbed by the 300 µm silicon semiconductors behind the shielding, given in rad(Si), should be less than would be found behind 2 mm of Al-2024-T3 shielding. The thickness of the silicon semiconductors is based on typical thicknesses of commonly applied diodes, whereas the shielding thickness was based on the typical applied thicknesses for conventional electronics housing structures.

The angular dependence of the radiation attenuation is not taken into account, reducing the radiation analysis to the 2D-case. The incident particles are modeled as parallel beams normal to the surface, thus limiting the particles' effective traversed distance through the material.

3.4.1 Radiation Causes

The shielding effectiveness of the structure is dependent on the incident particles and as such a theoretical background is given on the shielding considerations for different particles.

Heavy Particles

The collisional stopping power of heavy particles (heavier than electrons) can be calculated using the Bethe-Bloch equation. Equation 3.5 describes the stopping power, which is the loss in energy per unit distance, as a function of different particle and target parameters: Relative particle velocity ($\beta = v/c$), Lorentz factor ($\gamma = c/\sqrt{c^2 - v^2}$), electron and incident particle mass m_e and m_p, the maximum kinetic energy to be passed on by the incident electron E_{kmax}, mean excitation energy I, electron radius r_e, charge number z, Avogadro's number N_A, the density correction factor δ, the shell correction factor C, the higher-order Bloch correction factor L_1 and the Barkas polarization correction factors L_2.

$$S(E) = \frac{ZKz^2}{A\beta^2}\left[\frac{1}{2}\ln\frac{2m_e c^2\beta^2\gamma^2 E_{kmax}}{I^2} - \beta^2 - \frac{\delta(\beta\gamma)}{2} + \frac{C(\beta)}{Z} + zL_1(\beta) + z^2L_2(\beta)\right] \tag{3.5}$$

$$K = 4\pi N_A r_e^2 m_e c^2 \tag{3.6}$$

$$E_{kmax} = \frac{2m_e c^2\beta^2\gamma^2}{1 + \left(\frac{2\gamma m_e}{m_p}\right) + \left(\frac{m_e}{m_p}\right)^2} \tag{3.7}$$

In material-science materials are commonly grouped by their atomic number Z and atomic weight A. Proton energy attenuation is proportional to the ratio Z/A, such that low-Z

materials tend to attenuate protons more effectively per unit areal density [26]. The charge deposition varies with energy. At lower energies (and hence lower particle velocities) the incident particles have more time per unit distance to deposit their charge, such that the charge deposition increases. The charge deposition is commonly described as the Linear Energy Transfer Coefficient (LET). As the incident particle traverses the target material the LET increases to approximately 1 MeV/nucleon, which is referred to as the Bragg peak, after which it rapidly decreases, as is seen from Figure 3.7.

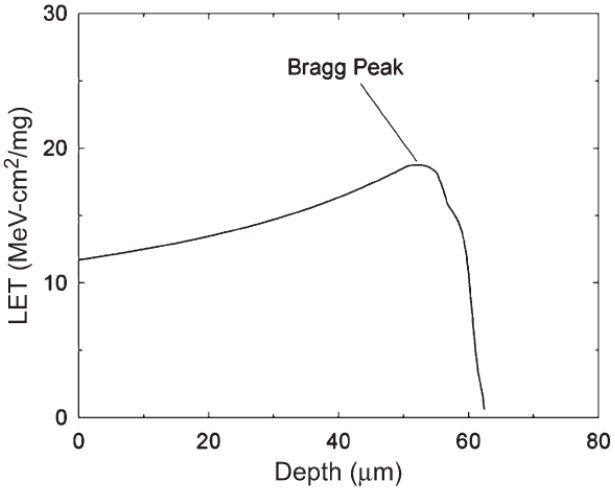

Figure 3.7: The Linear Energy Transfer coefficient (LET) versus depth, showing the Bragg peak at reduced energies. After [2].

Due to the large mass of protons they are not easily deflected and will as such not generate large quantities of gamma radiation. This means that the proton radiation attenuation is relatively straightforward and can be estimated with simple tools. Since protons are attenuated more effectively by low-Z materials the application of low-Z materials is beneficial in the proton-rich LEO. Note that if the thickness of the shielding material is constrained and the effectiveness is normalized by density, rather than areal density, high-Z materials become more effective, due to their larger density.

Beta Particles

Due to the small mass of electrons ($m_e = 9.11 \cdot 10^{-31}$ kg) these are easily deflected by the target material's protons. Therefore the stopping power of electrons consists of two contributions: The collisional and the radiative stopping power. The collisional stopping power can be estimated by an alternative Bethe-Bloch relation, where ϵ_0 is the vacuum permittivity and g is the Fermi density correction factor.

$$S_C(E) = \frac{2\pi e^4 N_A Z}{(4\pi\epsilon_0)^2 m_e v^2}\left(\ln\frac{m_e v^2 E}{2I^2(1-\beta^2)} - g(\beta)\right) \tag{3.8}$$

$$S_R(E) = \frac{N_A E Z(Z+1)e^4}{137 m_e^2 c^4}\left(4\ln\frac{2E}{m_e c^2} - \frac{4}{3}\right) \tag{3.9}$$

For low energies, where the electron energy E_e is smaller than the critical energy E_c collisional processes are dominating. Ionization will take place upon interaction with the target atom. If $E_e > E_c$ electrons are most likely to lose energy by means of Bremsstrahlung (German for braking radiation) [52].

$$E_c \approx \frac{610}{Z + 1.24} \text{ MeV} \tag{3.10}$$

When electrons are deflected and decelerated by the target nucleus the kinetic energy is converted into a gamma-ray, based on the law of conservation of energy, see Figure 3.8.

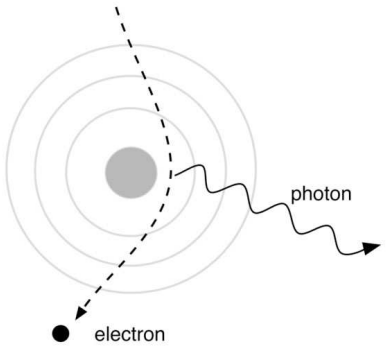

Figure 3.8: The bremsstrahlung generation mechanism, where kinetic energy is converted into a photon. After [53].

The generated photon can have energies in the range of 0 keV up till the energy of the incident electron, depending on the amount of deceleration. In accordance with Planck's equation, where h is Planck's constant and f is the frequency, the photon will have a corresponding wavelength λ.

$$E = hf = \frac{hc}{\lambda} \tag{3.11}$$

The number of photons of a specific energy is inversely proportional with the photon energy, such that low-energy photons will be generated more frequently than high-energy photons. The generation of bremsstrahlung is proportional to EZ^2/A and as such high-Z materials in general generate more photons [18, 26]. However, electron energy is attenuated in the process and as such high-Z materials are more effective for electron attenuation than their low-Z counterparts. This means high-Z materials will be very effective in the electron-rich GEO. A second photon generation mechanism is X-ray fluorescence, when an incident electron knocks out an electron from its shell, leaving a vacancy in its place. Electron knock-out is only possible if the incident particle energy exceeds the electron binding energy. An electron from an outer shell may take its place, generating a characteristic X-ray in the process. The photon energy is determined by the difference in binding energy of the respective shells.

The generated photons can lose energy by three different mechanisms, depending on their cross sections σ. The mechanisms are shown schematically in Figure 3.9. The Beer-Lambert law (Equation 3.12) gives the gamma ray intensity I after attenuation as a

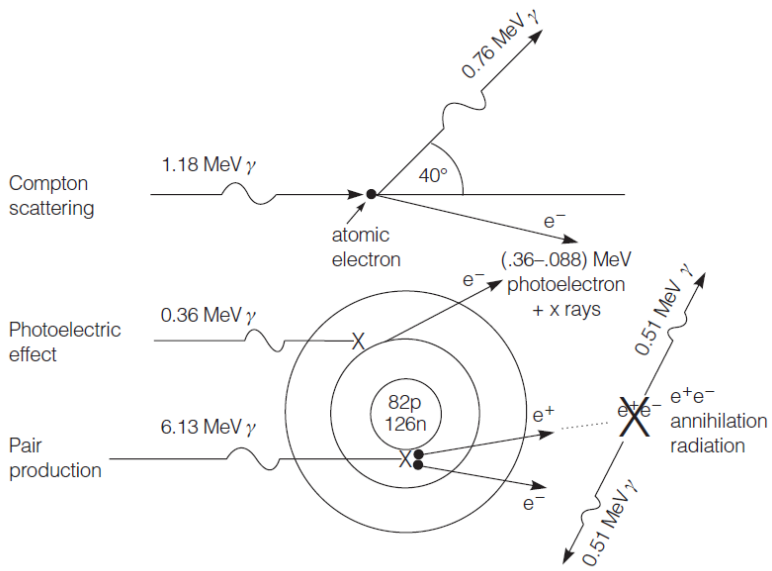

Figure 3.9: Photon Absorption Mechanisms. After [54].

function of the specific attenuation coefficient μ and the target thickness t. The specific attenuation coefficient is in its turn the sum of all attenuation contributions, given as a function of the cross section for the respective energy-loss mechanisms.

$$I = I_0 e^{-\mu t} \tag{3.12}$$

$$\mu = \sum_{i=1}^{3} \frac{\sigma_i \rho N_A}{A} \tag{3.13}$$

The first energy-losing mechanism, which dominates in the high-energy region (above $1,022$ keV) is pair production, see Figure 3.10. The photon is absorbed for the creation of a pair of positrons and negatrons. A threshold value at which pair production can occur is $1,022$ keV, based on the mass-energy equivalence equation ($E = mc^2$). Any remaining energy is converted in the generated particles' kinetic energy. The generated positron is quickly annihilated after recombination with an electron, leading to a new photon pair. The specific attenuation coefficient of pair production is proportional to Z^2/A [55].

The second method, dominating in the mid-energy region (around 1 MeV) and proportional to Z/A is Compton scattering. The gamma ray collides with and ejects an electron of the target material's atom. The gamma ray continues with decreased energy, based on the laws of conservation of energy and momentum.

The third photon energy loss mechanism is the photoelectric effect, which dominates the low-energy region and is proportional to $Z^4/\left(AE^{3.5}\right)$. In this mechanism the photon collides with a target electron and ejects it from its atom. The photon is absorbed and the electron will have the same kinetic energy as the incident photon, deduced with the required binding energy.

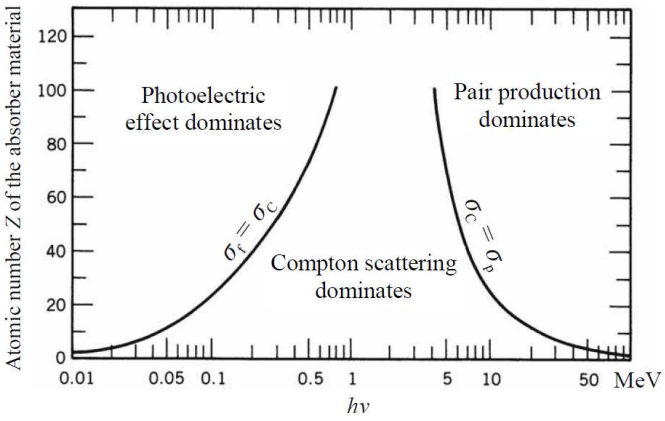

Figure 3.10: Gamma irradiation cross sections vary with photon energy. After [56].

Figure 3.11 shows the mass attenuation coefficient of tungsten. In the photoelectric-dominated low-energy region sharp absorption edges can be identified, which are a result of the characteristic binding energies and photofluorescence. When the photon energy is slightly higher than the binding energy of a specific shell the electrons in that specific shell might be ejected. In case the photon energy is below this threshold this cannot occur, resulting in a sudden fall in attenuation coefficient for lower energies.

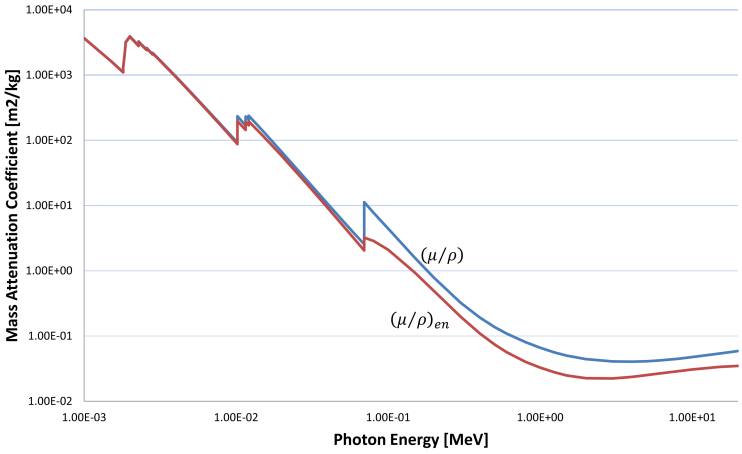

Figure 3.11: Mass attenuation coefficient (blue) and mass absorption coefficients (red) of tungsten. The photons are fully absorbed at low energies, whereas at higher energies attenuation might occur. Data obtained from [57].

3.4.2 Validation of Particle Attenuation Prediction

For the validation of the particle simulation tools an initial proton irradiation test was performed, using a parallel monoenergetic beam of 20 MeV. The tested laminate configurations, the manufacturing and the results are given in this section.

Test Configurations

Twenty test samples were manufactured for initial proton irradiation testing. The samples varied in number of metallic layers, materials (steel 1.4310 or tungsten foils), number of composite material layers (six or eight) and the location of the metallic layer(s). A detailed description of the test samples is given in Table 3.3. Since the radiation attenuation is independent on the fiber lay-up orientation vector x_l the configurations are presented with numbers for the number of carbon fiber layers and an S and W for respectively steel and tungsten layers of 50 µm. E.g. Sample 4, with configuration 2W4, has two carbon fiber plies placed external of the tungsten foil and four composite layers placed behind the foil. In the fourth column of Table 3.3 the corrected areal density is given, due to grit embedment during grit blasting of the metallic foils, as was explained in Section 2.2.3.

Trilayer Based on the literature the trilayer concept was tested, which is very effective in mixed proton-electron environments. The implementation of a high-Z layer in between two low-Z layers highly improves the effectiveness for electron attenuation ($\propto Z^2/A$), whereas it has only minor detrimental effects on proton attenuation ($\propto Z/A$). The configuration is shown schematically in Figure 3.12.

(a) (b) (c)

Figure 3.12: Concept design proposals. (a) A conventional trilayer with a high-Z layer (blue) between the low-Z composite material, (b) a pentalayer with a mid-Z layer (orange) in front of the high-Z layer and (c) a pentalayer with a Gadolinium layer (green) placed aft of the high-Z layer were proposed. In this figure the radiation comes from the top.

In the external low-Z layer the generation of unwanted gamma rays is limited in the high-energy domain. Another advantage of having an external low-Z layer is dispersion. Upon impact secondaries will be dispersed over an angle from the normal plane, such that their effective apparent distance through the remainder of the target is increased. The small amount of gamma rays are absorbed most effectively by a high-Z layer. In the photo-electric absorption process a secondary electron is ejected from its shell, which is in turn attenuated by the internal low-Z layer. In the low-energy domain the collisional stopping power is the dominating effect, such that the selection of a low-Z layer is beneficial.

Pentalayer Two novel design concepts were proposed; both being a variation of a pentalayer design, featuring five layers. Mangeret et al. researched configurations featuring five layers of dissimilar materials, but their research was limited to the application of only high-Z and low-Z materials [26].

For the first design proposal a mid-Z layer was introduced. In case a high-energy electron-rich environment is traversed the generation of gamma rays should be limited as much

as possible. In the external low-Z layer the collisional stopping power is maximized, as for the trilayer. Nonetheless, due to the large electron energies still a significant amount of high-energy photons is generated. In order to attenuate the gamma rays effectively by means of pair production a high-Z material is required, whereas the generation of more photons should be limited. The contradicting set of objectives leads to the selection of a mid-Z material for the second layer.

An intermediate low-Z layer is applied behind the mid-Z layer, for the optimization of the Compton scattering ($\propto Z/A$) and for limiting the generation of photons. In this research the intermediate low-Z layer was also applied for manufacturing reasons. Metallic layers will not adhere to each other without the application of adhesives. The application of adhesives was rejected in order to limit the number of materials and manufacturing steps. Hence an intermediate composite layer was required to bond the metallic layers. In the low-energy region, aft of the third layer, the generation of gamma rays is inherently limited, such that a high-Z material can be applied for photon absorption in the subsequent layer. Secondary electron attenuation is achieved in the final internal low-Z layer. Even if the concept was not tested for high-energy electrons the adverse effects on proton attenuation also required investigation.

Another pentalayer concept was proposed, featuring a gadolinium layer for the absorption of secondary neutrons. This configuration however was not tested during proton testing. For the applied optimization routine the application of steel and gadolinium was restricted. Steel was initially included for high-energy photon absorption and, when used in combination with tungsten, was always placed in front of the tungsten layer. The gadolinium was included for secondary neutron absorption and when combined with tungsten was always placed aft of the tungsten layer.

Manufacturing And Testing

The test samples were manufactured in two batches. One laminate of six composite layers $(0/45/-45)_{se}$ and one laminate of eight composite layers $(0/45/-45/90)_{se}$ were manufactured. Metallic foils of 20×20 mm were implemented in their respective positions during the lay-up process, after having been grit blasted. The grit blasting procedure was discussed in Section 2.2. The grit blasting procedure was found to cause grit embedment, such that the grit particles would remain in the tungsten, leading to an effective mass gain. After curing, the laminates were cut in samples of 10×10 mm, using a Proxxon Fet diamond-coated cutter. One of the samples is shown in Figure 3.13.

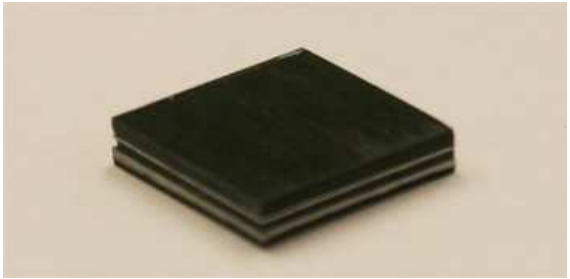

Figure 3.13: One of the 20 proton irradiation test samples.

Preliminary proton testing was done, at partner-company CSL, for 20 different configurations, consisting of carbon fiber plies and tungsten and steel foils, to validate the Geant4 and Mulassis particle simulation tools. A monoenergetic parallel proton beam of 20 MeV was used, based on the limitations of the particle accelerator. Due to the non-linearity of the LET, as was seen in Figure 3.7, the shielding effectiveness is higher in the low-energy domain, which should be taken into account. Therefore the mass efficiency of the samples was calculated by comparison with the equivalent aluminum areal density, required to attenuate the same amount of energy.

Results and Discussion

The results, given in Figure 3.14 and Table 3.3, show the measured energy of the protons behind the shielding. Note that the decrease in proton energy is not the same as the deposited energy in the shield, since secondary particles are generated in the process, which carry part of the energy, as can be seen from Equation 3.14.

$$E_{initial} - E_{deposited} = E_{proton} + E_{electron} + E_{neutron} \tag{3.14}$$

Also the Geant4 and Mulassis simulation results are given and the required equivalent aluminum areal density. In accordance with the literature the configurations featuring relatively the largest quantity of low-Z materials, gave the highest efficiencies. The pure composite configuration achieved the highest efficiency (mass reduction of approximately 22%), followed by the configurations featuring a single steel foil. The position of the metallic foils did not have a significant effect on the proton attenuation. Note that the efficiencies given here are w.r.t. the uncorrected areal densities.

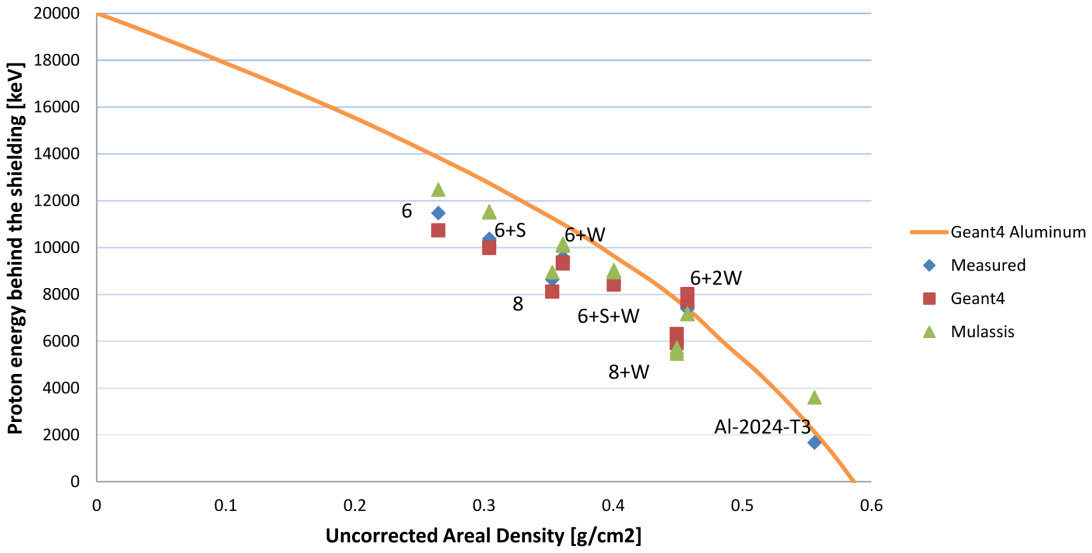

Figure 3.14: Proton irradiation results. The Geant4 simulations show good correspondence to the measured values. Geant4 data was provided by SensorCenter Oy and Yuzhnoye. The configurations are grouped by their respective number of carbon fiber plies and number of metallic layers (S or W).

From the test results the Geant4 simulation tool was fine-tuned, such that the attenuated energy error was on average 2.1%. The error could be ascribed to the experienced manufacturing problems of particle embedment. However, the computation time is very large and can therefore not be applied on large scale. Thus also a Mulassis simulation tool was validated for all test samples. The input of the Mulassis tool was based on stoichiometric elemental fractions for the composite material and the metallic layers. The composite material was given to be composed of $10-25\,\%$ $C_{18}H_{20}O_3$ and $5-10\,\%$ $C_{40}H_{48}O_7$. Given that the fiber mass fraction is 68% the epoxies were estimated to contribute to the total mass for 22% and 10% respectively. Variations to the assumed compound fractions might lead to deviations between the theoretical and the measured values.

The mass gain of the tungsten foil was included and purely ascribed to aluminum oxide, resulting in an effective thickness of 98.35 µm. Also the mass loss of the steel foil, as was discussed in Section 2.2, was taken into account. The stoichiometric fractions for the materials are given in Appendix B. The Mulassis tool obtained an average error of 6.3%, where the attenuation effectiveness of the samples in most cases was underestimated, as can be seen from Figure 3.14. Similar underestimation was found for the Al-2024-T3 sample. As such it was assumed that for comparative analysis, as was needed for the optimization routine, the Mulassis tool was sufficiently accurate.

3.4.3 Validation of Gamma Radiation Attenuation Prediction

For the validation of the effectiveness of composite laminates in electron-rich environments, where secondary gamma rays are generated, an initial gamma irradiation test was performed, as is discussed in this section. Note that the analysis was not performed with the Mulassis tool, since the applied cobalt source could not be modeled. As such this analysis is meant for the validation of the effectiveness of laminates only.

Manufacturing and Testing

In similar fashion as the proton samples one electron/gamma irradiation sample was manufactured. A $(0/45/-45/90/W^{50})_{so}$ sample of 50×50 mm was cut out of a 100×100 mm laminate. Gamma irradiation testing was done at partner company CSL. The 3" × 3" NaI(Tl) Ortec 905-4 scintillator was placed coaxially at 2 mm distance from the 1.17 µCi standard ^{60}Co source, as shown in Figure 3.15 [58].

The cobalt source emits beta particles of 0.31 MeV through beta decay, resulting in excited nickel nuclei, which consecutively emit gamma rays of $1,173$ and $1,332$ keV.

$$^{60}_{27}\mathrm{Co} \rightarrow {}^{60}_{28}\mathrm{Ni} + \beta^- + \gamma_{1,173} + \gamma_{1,332} \tag{3.15}$$

Figure 3.16 shows the gamma spectroscopy response function of the NaI(Tl) scintillator for a measuring time of 300 s. The response function gives the number of counts per energy channel of the detector. Two photopeaks (indicated in Figure 3.16 by e and f) at photon energies of $1,173$ and $1,332$ keV were found as expected. These photons are absorbed in the scintillator directly. However, also Compton scattering takes place in the scintillator itself. The amount of transferred energy, by means of Compton scattering,

No.	Config.	$\bar{\rho}$ [g cm^{-2}]	$\bar{\rho}_{\mathrm{corr}}$ [g cm^{-2}]	Measured [keV]	Geant4 [keV]	Mulassis [keV]	$\mathrm{Al}_{\mathrm{eq}}$ [g cm^{-2}]	Mass red. [%]
1	Al-2024-T3	0.5560	0.5560	1663	-	3596	-	-
2	6	0.2647	0.2647	11466	10725	12470	0.3559	25.6
3	8	0.3529	0.3529	8625	8113	8947	0.4404	19.9
4	2W4	0.3612	0.3804	9314	9314	10079	0.4209	14.2
5	3W3	0.3612	0.3804	9427	9313	10074	0.4177	13.5
6	4W2	0.3612	0.3804	9438	9331	10069	0.4174	13.5
7	5W1	0.3612	0.3804	9582	9351	10154	0.4134	12.6
8	2S4	0.3042	0.3027	10278	9974	11518	0.3937	22.7
9	3S3	0.3042	0.3027	10373	9990	11501	0.3910	22.2
10	4S2	0.3042	0.3027	10071	9988	11504	0.3995	23.9
11	5S1	0.3042	0.3027	10267	9995	11541	0.3940	22.8
12	4W4	0.4494	0.4686	5914	5914	5472	0.5001	10.1
13	6W2	0.4494	0.4686	6082	5997	5589	0.4967	9.5
14	7W1	0.4494	0.4686	6009	6300	5727	0.4982	9.8
15	3W1W2	0.4577	0.4960	7406	7710	7183	0.4701	2.6
16	4W1W1	0.4577	0.4960	7382	8006	7154	0.4706	2.7
17	3S1W2	0.4007	0.4183	8424	8407	8943	0.4458	10.1
18	4S1W1	0.4007	0.4183	8581	8482	9036	0.4416	9.3
19	2S2W2	0.4007	0.4183	8583	8420	8944	0.4416	9.3
20	3S2W1	0.4007	0.4183	8470	8460	9016	0.4447	9.9

Table 3.3: Description and results of proton test samples. Geant4 simulations were performed by partner-companies SensorCenter Oy and Yuzhnoye.

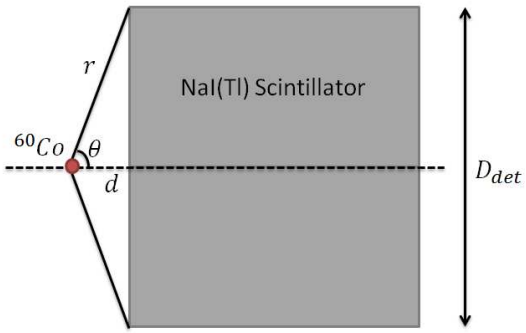

Figure 3.15: Schematic overview of the gamma irradiation test setup.

is a function of the scattering angle ϕ, leading to a distribution of photon energies: The Compton plateau or continuum (b).

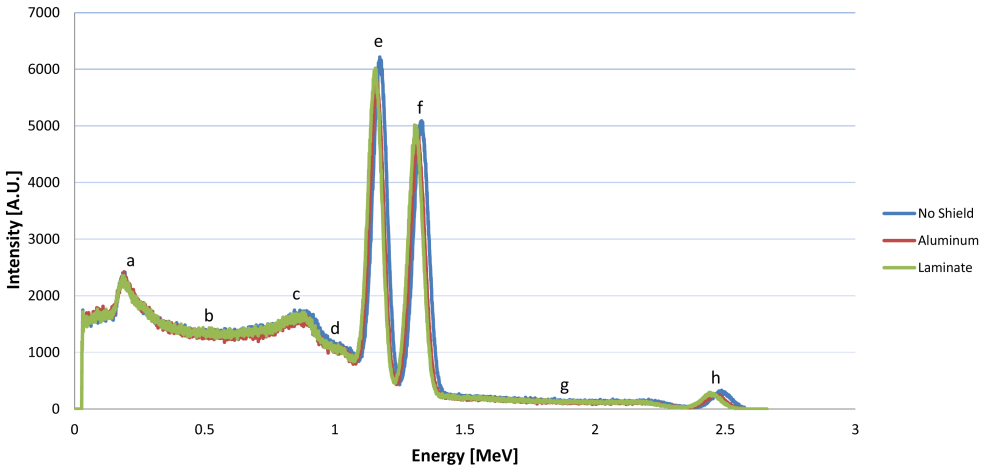

Figure 3.16: Gamma irradiation energy spectrum, showing the Compton continuum (b), the two characteristic photopeaks (e and f) and the sum-peak (h).

Maximum energy is transferred to the electron E_e if the photon is scattered back in the direction of the incident photon ($\phi = 180°$), giving rise to the Compton edge (c), which is limited by the laws of conservation of energy and momentum. The Compton edge was found to be located at 845 keV whereas theory predicts a value of 960 keV.

$$E_e = E_\gamma - E'_\gamma = E_\gamma \left\{ 1 - \frac{1}{\left[1 + \frac{E_\gamma (1 - \cos\phi)}{m_0 c^2} \right]} \right\} \tag{3.16}$$

The scattered photons, with energy E'_γ, were also absorbed in the detector, leading to the backscatter peak (a) at $E'_\gamma|_{\phi=180°}$. The scattered photons might also have been scattered into material surrounding the detector, reducing their energy even further, before being absorbed, leading to a bump in the low-energy region.

The response found in between the Compton edge and the first photopeak (d) was ascribed to the occurrence multiple Compton events. In the case of multiple subsequent Compton scatterings more energy is transferred to the scintillator electrons than by single Compton scattering, which leads to the response at energies higher than the Compton edge.

In case two photons arrive at the detector simultaneously, these will be counted as a single count. By summation of the photons, energies larger than the photopeak energies were found in the so-called pulse pile-up region (g). Subsequent gamma emission of the $1,173$ and $1,332$ keV photons can also lead to summing in the detector, resulting in the true coincidence summing peak (h), located at $2,505$ keV [55].

Results and Discussion

The net photopeaks were found by subtracting the background continuum from the response function. The background continuum was assumed to be trapezoidal at the respective peaks, as is shown in Figure 3.17 [59].

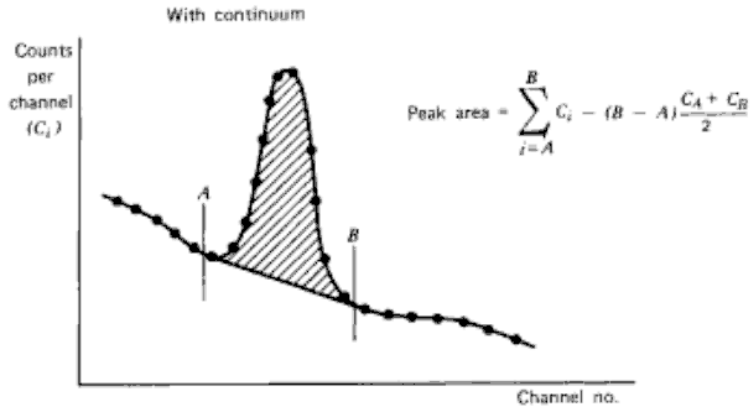

Figure 3.17: The net peak count was determined by subtraction of the respective trapezoidal areas below the peaks. After [59].

After subtraction two Gaussian peaks at respectively 1,173 and 1,332 keV were left. The photopeaks overlapped, such that a single double-Gaussian fit was applied over the entire region of interest, as is shown in Figure 3.18. The Gaussian fit is described by equation 3.17, where b_i is the mean μ and coefficient c_i is a function of the standard deviation σ: $c_i = \sqrt{2}\sigma_i$ for the considered photopeak. In similar fashion a single Gaussian curve is fitted to the net sum-peak.

$$f(E) = a_1 e^{-\left(\frac{E-b_1}{c_1}\right)^2} + a_2 e^{-\left(\frac{E-b_2}{c_2}\right)^2} \tag{3.17}$$

Note that the detector had 1,500 channels/MeV (n_{ch}), such that the integral of the curves as function of energy was multiplied by 1,500 to achieve the net count number. The integral for the individual Gaussian distributions is given as:

$$\sum \gamma_i^{ph} = n_{ch} \int_0^\infty a_i e^{-\left(\frac{E-b_i}{c_i}\right)^2} \mathrm{d}E = n_{ch} \cdot a_i \sqrt{c_i^2 \pi} \tag{3.18}$$

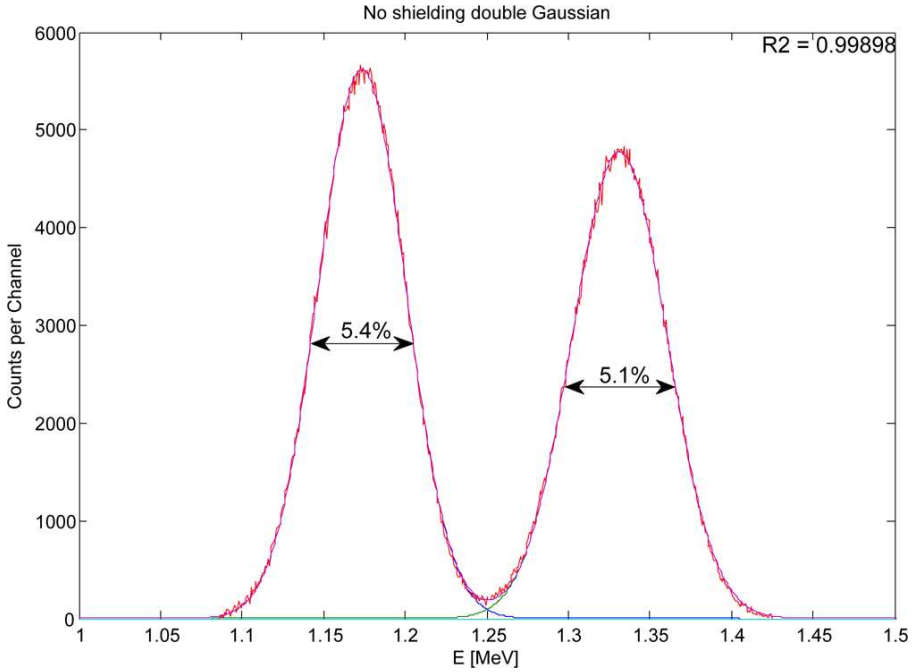

Figure 3.18: Double Gaussian fit through the gamma photopeaks for the no-shielding configuration, after subtraction from the trapezoidal count area below the peak.

The resolution R of the detector was obtained from the fraction of the Full Width Half Maximum (FWHM) value, which is the width of the peak where the Gaussian distribution is at half of its amplitude, over the photon energy E_γ. The resolutions for the two photopeaks were calculated to be respectively 5.4% and 5.1%.

$$\text{FWHM} = 2c_i\sqrt{\ln 2} \approx 2.355\sigma \tag{3.19}$$

$$R = \frac{\text{FWHM}}{E_\gamma} \cdot 100\% \tag{3.20}$$

Validation of Source Activity The peak intensities were estimated by equation 3.21, where A is the (radio)activity in disintegrations per second, η is the gamma decay fraction (being approximately 1 for both the 1,173 and 1,332 keV photons), t is the measurement time, g is the geometrical efficiency, ϵ is the intrinsic detector efficiency, f is the photofraction, W is an angular correction factor (≈ 1.02) and L_t is a time resolution factor [60]. In the remainder of this thesis the radioactivity of the source will be referred to as *activity*. The counts in the coincidence sum-peak were estimated in similar fashion, using equation 3.22.

$$\sum \gamma_i^{ph} = Atg\eta(E_i)\epsilon(E_i)f(E_i)\left(1 - \epsilon(E_j)gW\right)L_t \tag{3.21}$$

$$\sum \gamma^{sp} = Atg^2\eta(E_1)\epsilon(E_1)f(E_1)\eta(E_2)\epsilon(E_2)f(E_2)L_t + N_c \tag{3.22}$$

The geometric efficiency g is the ratio of photons that reach the detector over the number of photons emitted by the source. For a point source the intensity complies with the inverse-square law, such that the intensity was normalized with the spherical surface $4\pi r^2$ at distance r. The angle subtended by the detector is called the solid angle Ω. The solid angle of the cone was estimated as a function of apex angle (2θ).

$$\Omega \approx \int_0^{2\pi} \int_0^{\theta} \sin\theta \mathrm{d}\theta \mathrm{d}\phi = 2\pi(1-\cos\theta) \tag{3.23}$$

$$g = \frac{\Omega r^2}{4\pi r^2} = \frac{\Omega}{4\pi} = \frac{1-\cos\theta}{2} \tag{3.24}$$

The intrinsic efficiency ϵ, being the fraction of number of photons interacting with the detector over the number of photons reaching the detector, was logarithmically interpolated from the given absolute total efficiencies for the Ortec 905-4 detector. The photofraction f, describing the number of counts found in the photopeak over the number of total counts, was given for 3" × 3" NaI(Tl) scintillators by Heath [61]. In Equation 3.25 coefficients c_1 and c_2 are empirical values of respectively 0.9270 and 0.4807 and photon energy E_γ is given in MeV.

$$f(E_\gamma) = 1 - c_1 e^{\frac{-c_2}{E_\gamma}} \tag{3.25}$$

The time-resolution factor L_t is a function of the resolving time ($2\tau = 0.5\,\mu s$) and the total coincidence-sum corrected count number N_t and can be estimated by Equation 3.26. The resolving time is the time interval between the particles that will permit them to be detected separately.

$$L_t = 1 - \frac{2\tau N_t}{t} \tag{3.26}$$

$$N_t = A\eta t \left\{ \left(\epsilon(E_1) + \epsilon(E_2)\right) g - \left(\epsilon(E_1)\epsilon(E_2) g^2 W\right) \right\} \tag{3.27}$$

Full-energy peak efficiencies (FEPE $= g \cdot \epsilon \cdot f$) and the total net number of counts in the photopeaks are given in Table 3.4. Due to the emission of multiple gamma energies the relative measured number of counts in a specific photopeak is normalized with respect to the expected number of gamma rays of that energy reaching the detector.

$$f_{\mathrm{norm}}(E_1) = f(E_1) \frac{\epsilon(E_1) + \epsilon(E_2)}{\epsilon(E_1)} \tag{3.28}$$

Since the source was not an ideal point source the true subtended angle was reduced, leading to a lower geometrical efficiency. Moreover secondaries were emitted from the source's casing, resulting in lower photofractions, due to the additional noise in the low-energy regions. This is shown in Figure 3.19. Also the beta emission by the source causes additional low-energy counts.

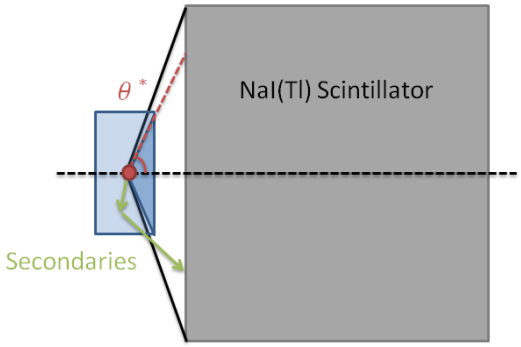

Figure 3.19: Gamma radiation test results were affected by the nonideal test conditions. The source casing led to directionality of the source, reducing the subtended solid angle. Secondaries, generated by the casing, increased the amount of data noise further.

Energy	1,173 keV		1,332 keV	
	theoretical	measured	theoretical	measured
Photofraction	0.3855	0.2849	0.3542	0.2724
FEPE	0.0856	0.0437	0.0756	0.0402
Net peak count	$8.61 \cdot 10^5$	$5.67 \cdot 10^5$	$7.52 \cdot 10^5$	$5.21 \cdot 10^5$

Table 3.4: Unshielded gamma test results

Shielding Effectiveness of Absorbers For the configurations where an absorber was placed in between the source and the scintillator detector similar analysis was possible. However, due to the nonideal test setup the analysis was limited to qualitative analysis between the different configurations only. The two absorbers, aluminum and the laminate, were compared with the unshielded configuration.

The theoretical mass attenuation coefficient of the $(0/45/-45/90/W^{50})_{\text{so}}$ laminate was determined by the constituent mass fractions $\hat{m}_i$ and individual mass attenuation coefficients μ/ρ [62]. The individual mass attenuation coefficients were logarithmically interpolated from the values found in the literature [63]. The rule of compounds, given by Equation 3.29, applies to both ply level, where the mass fraction of the different elements are used, and to laminate level, for which the fractions of carbon fiber composite and metallic layers are used.

$$\left(\frac{\mu}{\rho}\right)_{eq} = \sum_{i=1}^{n} \hat{m}_i \left(\frac{\mu}{\rho}\right)_i \tag{3.29}$$

Similar Gaussian fits were applied to the net peaks for the configurations with absorbers as for the reference test, all having $r^2 > 0.998$. The mass attenuation coefficient of the absorbers was determined by rewriting the Beer-Lambert equation. In this case I_0 and I

are the peak intensity for the unshielded and shielded configuration, respectively.

$$\frac{\mu}{\rho} = \frac{\ln\left(\frac{I}{I_0}\right)}{\rho t} \tag{3.30}$$

Figure 3.20 gives the comparison of theoretical and measured mass attenuation coefficients. From the results it can be seen that the theoretical values are 2-3 times lower than the measured results, which was ascribed to the nonideal conditions. However, the inverse relation between energy and mass attenuation was verified. Even though it can be seen that the mass attenuation coefficients of the laminate and the aluminum reference were of the same order of magnitude the laminate showed lower mass attenuation values than the aluminum, whereas the reverse was expected. This could be caused by variations in the material composition.

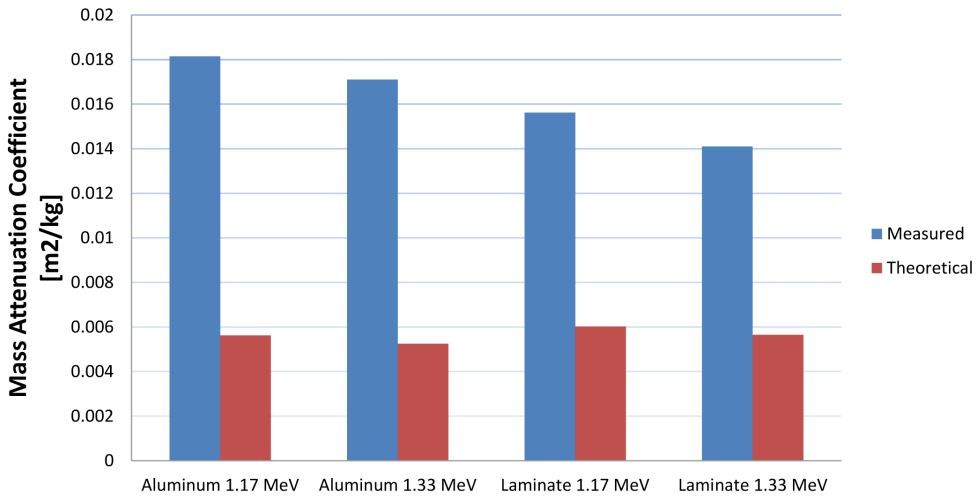

Figure 3.20: The theoretical and measured mass attenuation coefficients for both gamma peaks for aluminum and the laminate. It can be seen that the measured value highly overestimate the attenuation properties, due to the nonideal testing conditions.

3.5 Natural Frequency Analysis

The natural frequency of the panel is required to be larger than 150 Hz. This requirement was given in the AED-project and was based on the theory of vibration isolation [7, 64, 65]. Resonance with the spacecraft body should be avoided and as such the vibrational response should be smaller than the input. This was translated into a transmissibility ratio R_T (response-input ratio), which should be smaller than unity. The transmissibility ratio is given by Equation 3.31. In this equation Ω is the input frequency, ω_n is the

component's undamped frequency and ζ is the damping ratio.

$$R_T = \sqrt{\frac{1 + \left(\frac{2\zeta\Omega}{\omega_n}\right)^2}{\left(1 - \left(\frac{\Omega}{\omega_n}\right)^2\right)^2 + \left(\frac{2\zeta\Omega}{\omega_n}\right)^2}} \tag{3.31}$$

In order to obtain a Transmissibility ratio smaller than unity the relation $\Omega/\omega_n < \sqrt{2}$ should hold [65]. With the conservative assumption that the spacecraft's body has a frequency of 100 Hz a frequency limit for the components is set to 150 Hz [64].

With the panel being part of the complete box structure the edges of the panel are assumed to be simply-supported. Moreover a conservative approach is applied with respect to the effect of the wedge locks and the PCBs.

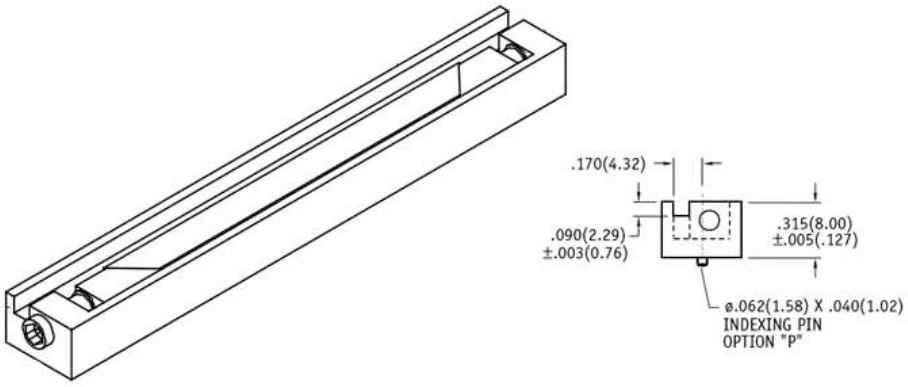

Figure 3.21: The V340 VME Wedge-Tainer wedge lock design

The used wedge lock, of type V340 VME Wedge-Tainer, is made out of Al-6061-T6 alloy and is shown in Figure 3.21 [66]. The wedge lock dimensions ($w \times h \times l$) were given to be $13.46 \times 8.00 \times 246.5$ mm. The wedge locks are modeled as equispaced rectangular bars of the aluminum alloy, located at respectively 20%, 40%, 60% and 80% of the length in y-direction and running over the entire length in x-direction. However, due to the presence of holes the height h is adjusted such that the given length density of 265 g m^{-1} for the wedge lock is achieved. The resulting height is 7.29 mm. By reducing the height rather than the width w the Steiner term for out-of-plane stiffness is limited and as such a conservative value is found.

Also four PCBs were modeled. The PCBs, of 0.475 kg each, are attached to both the bottom and the top panel of the box structure and as such only half the mass is carried by the top panel [7]. Since the PCBs are only attached to the wedge locks by friction forces the stiffening effect of the PCBs is ill-defined. Furthermore the time-dependence of the stiffening effect is unknown. Again a conservative approach is applied and the stiffening effect of the PCBs is neglected, as is shown in Figure 3.22. However, the mass of the PCBs is included, effectively reducing the natural frequency. The PCB dummy mass is introduced by multiplying the density of the wedge locks with a mass correction factor, such that the simulated wedge lock has the mass of both wedge lock and the attached

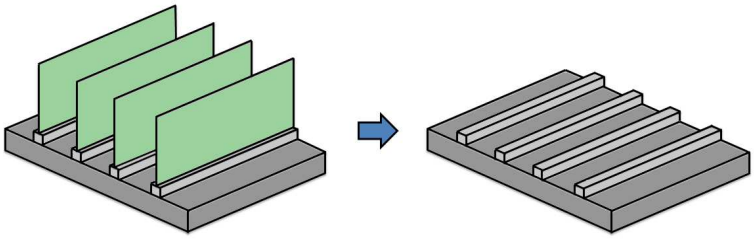

Figure 3.22: The structural model. For out-of-plane analysis the wedge locks are included, whereas the PCBs are modeled as dummy masses in the wedge locks, effectively increasing their density.

PCB. The natural frequency is then assessed using the ESAComp tool. ESAComp makes use of the CLT for the stress and strain calculations.

3.6 Structural Analysis

Structural integrity needs to be provided for the housing structure, such that it can withstand the large acceleration loads. The structural calculations were performed within the ESAComp environment.

3.6.1 Structural Model

For the assessment of the structural integrity of the top panel a simulation model is created for both the geometry and accelerations. A positive Margin of Safety (MoS) is required, such that the failure load of the structure exceeds the design load in x-, y- and z-direction. For the optimization process this is defined by the Reserve Factor (RF), which should be larger than unity.

$$\begin{aligned} \text{MoS} &= \left\{ \frac{\text{Failure load}}{\text{Design load} \cdot \text{Safety Factor}} \right\} - 1 \\ &= \text{Reserve Factor} - 1 \end{aligned}$$

The Von Mises failure criterion is used for the homogeneous metallic layers. Fiber-failure (FF) and inter-fiber failure (IFF) are investigated independently with the Coulomb-Mohr-based Puck2D criteria, applied to the brittle carbon fiber composites. As common practice prescribes a Safety Factor (SF) of 2 is used for the composite materials, unless stated otherwise.

For the in-plane loading response only the flat plat is considered. From a conservative approach the wedge locks are assumed to be non-load carrying and as such are excluded from the loading response. For the out-of-plane loading the wedge locks *are* included, due to their stiffening effects and their resultant change in panel mode shapes. The loads in x-, y- and z-direction are obtained from Newton's second law: $F = m \cdot a$, where m is the mass, a is the acceleration and F is the force. The mass of the panel is obtained from the summation of the individual ply masses and the four attached wedge locks and PCBs.

3.6.2 Acceleration Model

The accelerations were given in three directions in the AED-studies [64]. A power spectral density (PSD) for random vibrations (given in Figure 3.23) was obtained from flight data, which was transformed to a statistical probability of occurrence. Miles' equation defines n_r values for the n most important modes and were multiplied with their effective mass terms to obtain the contributions to the overall interface force F by the mode at the respective frequency. The root-sum square (RSS) of the mode contributions F_i were taken.

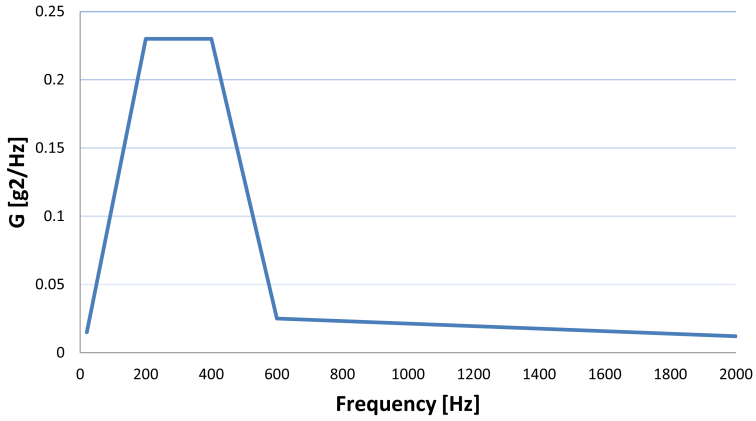

Figure 3.23: Power spectral density for random vibrations.

$$n_r = \sqrt{\frac{\pi}{2} \cdot Q \cdot f_n \cdot PSD} \tag{3.32}$$

$$F(RSS)_{1\sigma} = \sqrt{\sum F_i^2} = \sqrt{\sum (n_i \cdot m_{eff})^2} \tag{3.33}$$

In Equation 3.32 Q is the transmissibility factor, commonly assumed to be $\sqrt{f_n}$ for PCBs, with f_n being the natural frequency. For housing structures the transmissibility factor was assumed to be $0.5\sqrt{f_n}$. The 1σ probability was multiplied by a factor of 3 to achieve a 3σ statistical value, which occurs 4.33% of the time, and divided by the unit rigid body mass m_r to obtain the probabilities of accelerations.

$$a_{3\sigma} = \frac{3 \cdot F(RSS)_{1\sigma}}{m_r} \tag{3.34}$$

In accordance with NASA SSP-52005 low-frequency vibrations were also taken into account [67]. The maximum qualification sine level, used for the AED-studies was 20g, which was assumed to be 1.5 times the acceptance level, where g is the gravitational acceleration. The two contributions are combined and give accelerations of 25.6g, 53.3g and 29.3g in respectively x-, y- and z-directions.

$$a_{comb-3\sigma} = \sqrt{a_{3\sigma}^2 + \left(\frac{20g}{1.5}\right)^2} \tag{3.35}$$

3.7 Electrical Resistivity Analysis

Electrical resistivity ρ is a measure of the ease at which an electric current can flow through a material and is the reciprocal of the conductivity σ. The resistivity is independent of sample size and is as such a material property. For isotropic materials the resistivity is the same in all three directions, whereas for anisotropic materials the resistivity vector entries may have different values.

3.7.1 Theory

Even if the tungsten provides good electrical conductivity ($\sigma = 1.77 \cdot 10^7$ S m^{-1}), the composite material has a high transverse electrical resistivity, due to the resin's dielectricity. Typical conductivity values for electrical potting grade resins are in the range of $\sigma_m = 10^{-13}$ S m^{-1}, whereas the M40J fiber has a conductivity of $\sigma_f = 10^5$ S m^{-1}. Therefore the majority of the electrical current will flow through the thin metallic layer(s). The electrical conductivity in fiber and transverse directions are estimated with the rule of mixtures. With $\sigma_f \gg \sigma_m$ it is shown that in longitudinal direction the electrical conductivity is fiber-dominated, whereas the transverse conductivity is matrix-dominated, resulting in a low conductivity.

$$\sigma_l = \hat{v}_f \cdot \sigma_f + (1 - \hat{v}_f) \cdot \sigma_m \approx \hat{v}_f \cdot \sigma_f \tag{3.36}$$

$$\sigma_t = \frac{\sigma_f \cdot \sigma_m}{(1 - \hat{v}_f) \cdot \sigma_f + \sigma_m \cdot \hat{v}_f} \approx \frac{\sigma_m}{1 - \hat{v}_f} \tag{3.37}$$

If the fibers are placed under an angle θ w.r.t. the principle coordinate system, the contribution of the transverse conductivity becomes negligible ($\sigma_l \gg \sigma_t$).

$$\sigma_1 = \sigma_l \cdot \cos^2(\theta) + \sigma_t \cdot \sin^2(\theta) \approx \sigma_l \cdot \cos^2(\theta) \approx \sigma_f \cdot \hat{v}_f \cdot \cos^2(\theta) \tag{3.38}$$

$$\sigma_2 = \sigma_l \cdot \sin^2(\theta) + \sigma_t \cdot \cos^2(\theta) \approx \sigma_l \cdot \sin^2(\theta) \approx \sigma_f \cdot \hat{v}_f \cdot \sin^2(\theta) \tag{3.39}$$

For the total in-plane resistivity (in x- and y-directions) the laminae are modeled as a set of parallel resistances. For parallel resistances the electrical conductance of all n number of plies can be summed to obtain the equivalent conductance, based on the dimensions of their individual cross-sectional areas A_i and lengths l_i. The length is always taken in the direction of the resistivity, whereas the cross-sectional area is in the normal-plane of the length-vector [68].

$$G_{\text{eq}} = \sum_{i=1}^{n} G_i = \sum_{i=1}^{n} \sigma_i \cdot \frac{A_i}{l_i} \tag{3.40}$$

$$\rho_{\text{eq}}^{ip} = \frac{1}{G_{\text{eq}}} \cdot \frac{A_{\text{tot}}}{l_{\text{tot}}} \tag{3.41}$$

Analogously the through-thickness resistivity is determined by modeling the laminae as resistances placed in series, such that the individual resistances R_i are summed to obtain the equivalent resistance R_{eq}.

$$R_{\text{eq}} = \sum_{i=1}^{n} R_i = \sum_{i=1}^{n} \frac{1}{\sigma_i} \cdot \frac{l_i}{A_i} \tag{3.42}$$

$$\rho_{\text{eq}}^{tt} = R_{\text{eq}} \cdot \frac{A_{\text{tot}}}{l_{\text{tot}}} \tag{3.43}$$

3.7.2 Manufacturing and Testing

Four configurations were manufactured and tested. Two reference configurations, ER1 and ER2, were expected to have the same resistivity in longitudinal and transverse directions ($\rho_1 = \rho_2$). The two other configurations were tested to show the influence of the fiber direction on the in-plane resistivities. Also the influence of the implementation of metallic foils was shown. The tested configurations and the theoretical electrical resistivities are given in Table 3.5.

Sample	Stacking Sequence	ρ_1	ρ_2	ρ_3
ER1	$(0/45/-45/90)_{se}$	$3.37 \cdot 10^{-5}$	$3.37 \cdot 10^{-5}$	$4.06 \cdot 10^{12}$
ER2	$(0/45/-45/90/S^{50})_{so}$	$1.69 \cdot 10^{-5}$	$1.69 \cdot 10^{-5}$	$3.97 \cdot 10^{12}$
ER3	(0_8)	$1.68 \cdot 10^{-5}$	$4.06 \cdot 10^{12}$	$4.06 \cdot 10^{12}$
ER4	$(0_4/S^{50})_{so}$	$1.13 \cdot 10^{-5}$	$3.33 \cdot 10^{-5}$	$3.97 \cdot 10^{12}$

Table 3.5: Theoretical values for the electrical resistivity tests, given in [Ω m].

The samples featuring the same lay-up angles were manufactured in the same laminate, introducing a steel foil in only half of the laminate. The two laminates were cut into a total of four samples, with dimensions of 72 $\times$ 72 mm, as is shown in Figure 3.24. Cutting was done using a diamond-coated cutter and was subsequently abraded using sandpaper, exposing the fibers in the process. Copper wires were attached in the corners with Resinlab SEC1233 silver epoxy. The epoxy was allowed to cure for 24 hours, to obtain a volume resistivity of 0.0016 Ω cm. The silver provides a good conducting surface over the entire thickness between the copper wire and the laminate [69, 70]. In order to minimize noise in the results the samples were placed on an isolating rubber surface during testing.

The laminates' resistivity vectors were determined by means of a Van Der Pauw's four-point probe method. Four electrodes were placed on the corners of the flat rectangular laminate. A direct current was applied over one edge of the sample, using an EA-PS 3032-10B power supply, while the voltage was measured over the opposite edge. From Ohm's law ($R = V/I$) the resistance was obtained. The same was done in secondary direction. With the two orthogonal resistances measured the in-plane components of the resistivity vector were obtained.

For all four samples a total of eight measurements were required, in accordance with the standard Van der Pauw method. The calculation of the resistance in longitudinal and

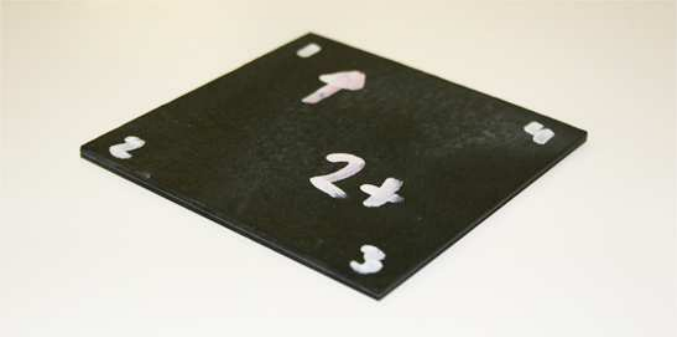

Figure 3.24: Electrical resistivity test sample. The corners were numbered in counterclockwise direction. At the four corners copper wires were attached using silver epoxy.

lateral direction is given in the Equations 3.45 and 3.46. In these equations the resistance $R_{AB,CD}$ is the resistance measured when a current is applied from A to B and the voltage is measured over C to D. The corners were numbered in counterclockwise direction, as is shown in Figure 3.24. The reciprocity theorem requires:

$$R_{AB,CD} = R_{CD,AB} \tag{3.44}$$

A set of reversed polarity measurements was needed for the exclusion of possible voltage offset effects. In order to increase the accuracy a total four measurements were done for the determination of the resistance in each direction and thereafter averaged:

$$R_1 = \frac{R_{12,34} + R_{34,12} + R_{21,43} + R_{43,21}}{4} \tag{3.45}$$

$$R_2 = \frac{R_{23,41} + R_{41,23} + R_{32,14} + R_{14,32}}{4} \tag{3.46}$$

3.7.3 Results and Discussion

A method to determine the electrical resistivity vectors for anisotropic materials was proposed by Montgomery [71]. A mathematical model is given in Appendix A.2 [71, 72]. A set of eight equations was solved numerically for eight unknowns: Electrical resistivities in three orthogonal directions (ρ_1, ρ_2, ρ_3), equivalent isotropic dimensions (l_1, l_2, l_3), the equivalent isotropic resistivity (ρ) and the effective thickness (E^*). The equivalent isotropic dimensions are a representation of the anisotropic material, as if it were isotropic. This set of equations, however, does not provide a unique solution and therefore the calculated resistivities were found to be highly dependent on the initial guess for the numerical solving routine. Since the exact electrical properties of the MTM57 resin are unknown no exact solution could be determined.

However, the qualitative analysis still holds. The mean measured resistances are given in Figure 3.25. The error bars indicate the standard deviations, calculated for the four measurements in both directions. For configuration ER1 the resistivity was estimated to

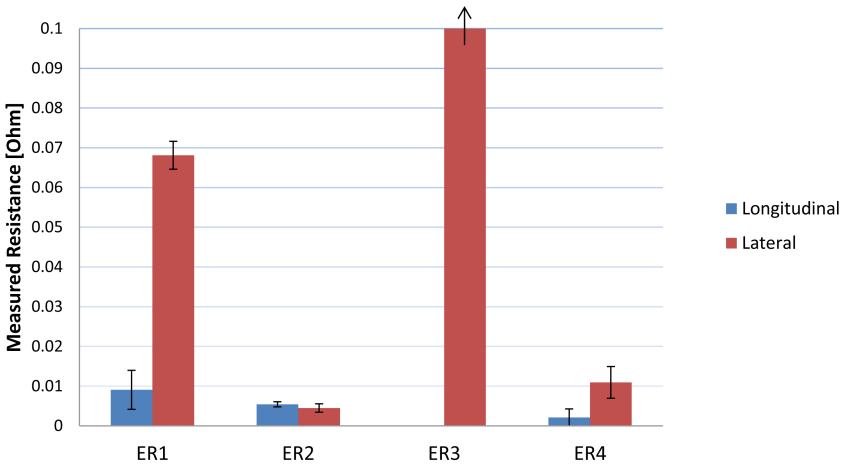

Figure 3.25: Measured electrical resistances, showing the mean values of the four measurements in both directions.

be the same in both directions. However, the measured resistance in lateral direction was found to be 7.5 times larger than the resistance in longitudinal direction. This difference is most likely caused by a combination of manufacturing errors, such as fiber misalignment and electrode misplacements.

Configuration ER2, which included a steel foil, compensates for the fiber misalignments errors. Since the steel is isotropic and carries the largest current, fiber misalignments have a smaller effect on the total conductance. The difference between longitudinal and lateral conductance was almost non-existing. The implementation of a metallic foil furthermore reduced the total resistance in both directions. In parallel circuits the more resistances are added the smaller the equivalent total resistance of the circuit becomes, as can be seen from equation 3.47.

$$\frac{1}{R_{eq}} = \frac{1}{R_1} + \frac{1}{R_2} + \frac{1}{R_3} + \cdots \tag{3.47}$$

Configuration ER3, which featured only composite plies in longitudinal direction, showed a large resistance in the resin-dominated lateral direction, whereas the resistance in longitudinal direction was too small to measure. Note that the true lateral resistance ($96.52 \pm 3.98\Omega$) exceeds the values in Figure 3.25. In comparison to configuration ER1, the resistance in longitudinal direction was smaller, whereas the resistance in lateral direction was larger, as was predicted by theory.

Finally, configuration ER4 had an improved resistance in lateral direction w.r.t. ER3, due to the presence of the conducting steel foil. The difference in longitudinal and lateral resistance was reduced significantly. However, when compared to ER2 the influence of the composite layers is observed. The lateral resistance exceeds the value as was found for ER2, whereas electricity is better conducted in longitudinal direction.

In summary, even if the electrical conductivities could not be determined exactly, the qualitative behavior of laminates featuring metallic foils was shown. The influence of the

metallic foil improves the isotropicity of the laminate, while providing a conduction path for electric currents in in-plane direction. The theory of parallel circuits was assumed to be applicable to metal-composite laminates. Since the exact electrical resistivities could not be determined further analysis was based on the theoretical values.

3.8 Induced Shape Distortion Analysis

For the optimization routine the stacking sequence of the plies is kept variable, hence possibly resulting in asymmetric laminates. Due to the asymmetric laminate lay-up and the elevated cure temperatures the laminates experience post-cure shape distortions due to residual stresses. For assembly reasons the energy required to force the panels into their original shape, taken at the reference curing temperature of 120 °C, should be minimized.

3.8.1 Theory

Due to the asymmetry of the elastic properties with respect to the geometric midplane, post-cure warping may occur. Thermal loading during the curing process leads to build-up of residual stresses, resulting in a deformation of the laminate. Due to the large deflections and hence geometric nonlinearities the standard Classical Lamination Theory (CLT) is no longer applicable. An extension to the standard CLT was proposed by Dano [73]. The CLT is well-documented in literature and is therefore omitted from this thesis [74–76]. The alternative Rayleigh-Ritz method is based on the minimization of potential energy for general laminates. From Figure 3.26 the difference in stable modes for the two methods can be seen.

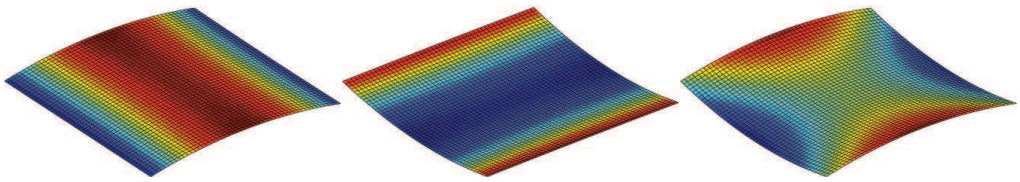

(a) (b) (c)

Figure 3.26: Warpage due to lay-up asymmetry and thermal loading. (a and b) Using the Dano-approach two stable cylindrical modes were found for a square 200×200 mm $90_2/0_2$ M40J/MTM57 laminate for a temperature decrease of 100 °C. (c) The CLT predicts a single anticlastic saddle shape.

The stable shape(s) of a laminate depend on the materials, dimensions, lay-up and temperature difference. The CLT usually predicts an anticlastic saddle-shape for flat thin asymmetric laminates, such that the principle curvatures are expected to be in opposite direction [77]. However, for laminates with sufficient dimensions and thermal loads different stable shapes are found. The discrepancies between the standard CLT predictions and reality are based on the interlaminar stresses at the free edges and should be accounted for [78].

For unsymmetric laminates bifurcation or trifurcation may occur, such that the laminates might have two stable cylindrical shapes and possibly a third stable saddle solution [78].

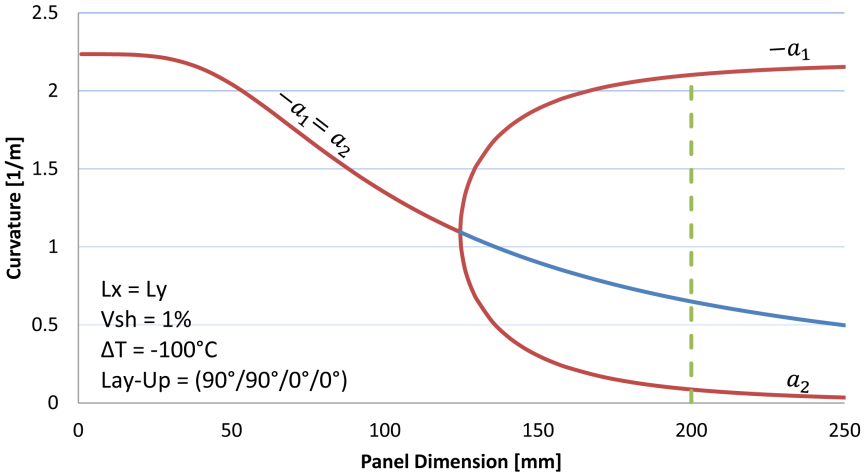

Figure 3.27: Principle curvatures versus laminate dimensions. For a $90_2/0_2$ lay-up bifurcation occurs at $124.6\,\mathrm{mm}$, such that two stable cylindrical shapes are found rather than a single stable saddle-shape.

Snap-through from one stable mode to another is achieved by applying a sufficiently large external moment to the laminate. Figure 3.27, shows the two principle curvatures for a square cross-ply laminate, for a temperature difference ΔT of $-100\,^{\circ}\mathrm{C}$ to room temperature. For square $90_2/0_2$ laminates, with dimensions larger than $124.6\,\mathrm{mm}$, bifurcation is experienced. The two found stable shapes are curvature conjugates, such that the same curvature is found, but in opposite directions. Apart from the two stable cylindrical shapes also a third unstable saddle shape was found, as is indicated in blue. For general laminates more complicated shapes were expected and were assumed to be of the form:

$$w^0(x,y) = \frac{1}{2}\left(a_1 x^2 + a_2 y^2 + a_3 xy\right) \tag{3.48}$$

The midplane strains were assumed to be third-order polynomial, resulting in a total of 28 displacement coefficients. For the determination of the stable shape(s) a Rayleigh-Ritz approach was applied for minimization of the potential energy, as was proposed by Hyer and Dano [73, 79, 80]. The mathematical background is discussed in Appendix A.1. By setting the first derivatives of the potential energy, with respect to the displacement coefficients, to zero the extremities were found, whereas the stability was assessed by the positive definiteness of the second variation: If all eigenvalues of the Hessian were positive the solution was stable and a local minimum was found, rather than a maximum. The proposed method is a non-linear extension to the CLT and as such gives a reasonably accurate analytical expression for the expected shape deformations. The equations were solved numerically within the Matlab environment.

Volumetric cure shrinkage of the epoxy material during curing also has an effect on warpage. The chemical shrinkage can reach values of up to 10% [81]. For initial analysis a volumetric cure shrinkage of 5% was assumed. The resin experiences three states during curing: The viscous, the visco-elastic and the elastic state. Up till the gelation point the resin behaves as a viscous liquid and is unable to build up any stresses. Thereafter it

changes into a rubbery substance, such that the resin modulus starts to increase, as it is in its visco-elastic state. Once the vitrification point has been reached and the resin is in its final glassy elastic state the temperature is reduced. With the assumption that 60% of the cure shrinkage occurs before the gelation point and 20% during its low-modulus rubbery state only 20% of the volumetric cure shrinkage v_{sh} leads to significant stress build-up, such that effectively only a cure shrinkage of 1% is experienced. The chemical cure shrinkage was introduced as an additional term to the resin's Coefficient of Thermal Expansion (CTE) and as such has an effect on the warpage [82].

$$\Delta\alpha_m = \frac{v_{\text{sh}}}{3\Delta T} \tag{3.49}$$

3.8.2 Manufacturing and Testing

For validation of the analytical tool a $90_2/0_2$ laminate of 200×200 mm was manufactured. The dimension selection was based on Figure 3.27, from which it can be seen that, assuming a volumetric cure shrinkage of 1%, two cylindrical shapes were expected to be found, rather than the anticlastic shape as was predicted by the CLT. Even without cure shrinkage these shapes were expected, as shown in Figure 3.28.

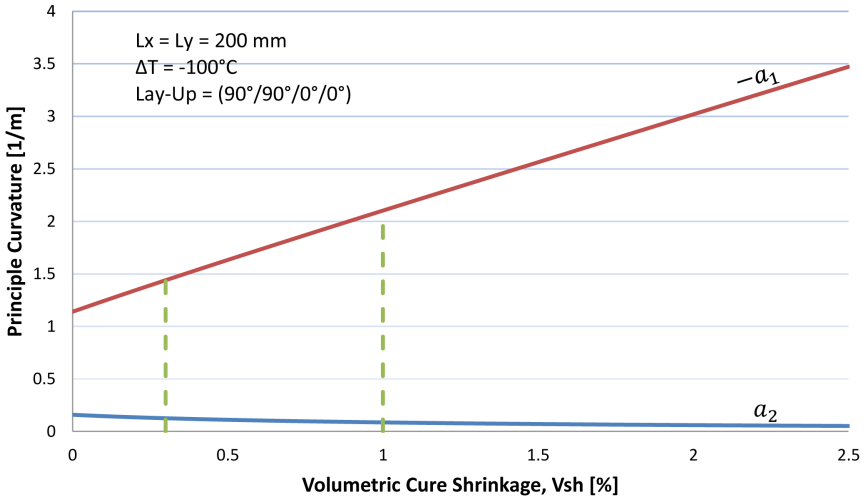

Figure 3.28: Principle curvatures versus volumetric cure shrinkage. It was shown that even without cure shrinkage cylindrical shapes are obtained for the $90_2/0_2$ laminate of 200×200mm.

3.8.3 Results and Discussion

The deflections were measured at the four corners and in the middle of each side, as is indicated by the red dots in Figure 3.29. It was found that the corners were all deflected to the same amount, such that the third curvature coefficient a_3 was assumed to be zero-valued. The curvatures of the two sides in both directions were averaged to obtain the remaining principle curvatures. The results are given in Table 3.6.

Principle Curvature [m^{-1}]	Mode I		Mode II	
	Theoretical	Measured	Theoretical	Measured
a_1	-1.44	-1.50	-0.13	-0.23
a_2	0.13	0.30	1.44	1.37
a_3	0	0	0	0

Table 3.6: Theoretical and measured principle curvatures for a 200×200 mm $90_2/0_2$ laminate, assuming a volumetric cure shrinkage of 0.3%.

The measured principle curvatures almost correspond to the expected values, when assuming a volumetric cure shrinkage of 0.3%. Figure 3.29 shows the real shape distortion as was found for the 200×200 mm laminate and the expected shape at the calculated cure shrinkage of 0.3%. The cure shrinkage was fine-tuned based on the major principle curvatures, to minimize the effect of measurement errors. However, it can be seen that the measured minor principle curvature for both stable modes was larger than estimated. This can be attributed to part-tool interaction, where the difference in thermal expansion coefficient of the laminate and the aluminum mold causes additional residual thermal stresses.

The difference in potential energy (or strain energy) between the stable shape and the original shape during curing equals the required energy to force the laminate into its original flat shape again during assembly. Thus the difference in potential energy is a good indicator of the induced shape distortion and was therefore introduced as a secondary objective function. Note that there is a fine balance between the in-plane and out-of-plane stiffness, such that the out-of-plane shape distortions are not per definition proportional to the potential energy difference.

For the manufacturing of flat radiation test samples the fiber lay-up orientation is not of any importance, since the radiation properties are independent of the lay-up orientation vector x_l. Thus for this special case the in-plane strains and their resulting fiber misalignments are non-critical and hence only the out-of-plane curvatures need to be restricted. Rather than using the original cure shape as the potential energy reference, a flat shape, having the in-plane deflections coefficients as free variables, can be set as reference. The reference shape will have the same in-plane displacement coefficients, whereas the out-of-plane coefficients are set to zero.

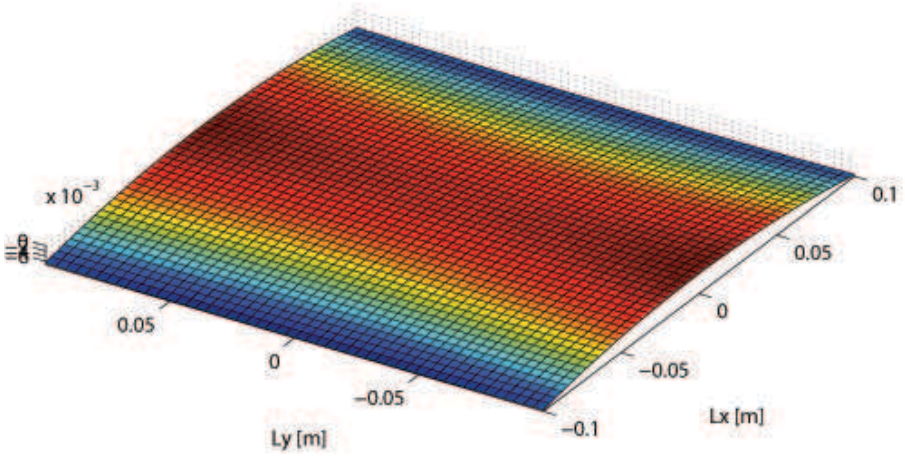

(a)

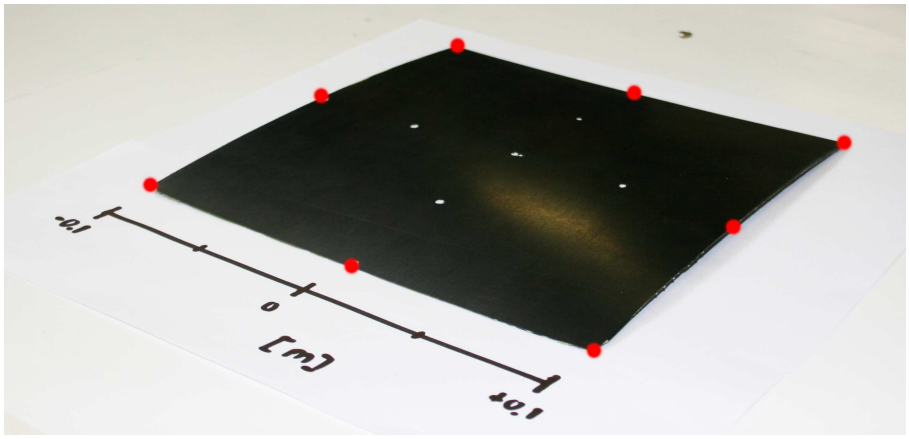

(b)

Figure 3.29: Comparison of the theoretical and measured shape distortion for a $200 \times 200\,\mathrm{mm}$ plate. Subfigure (a) indicates the theoretical shape assuming a volumetric curing shrinkage of 0.3%, whereas (b) shows the true shape after curing.

Chapter 4

Results

In this chapter the practical application of the proposed design methodology for composite space enclosures is shown. The design method was applied to the proposed SIDER missions (GEO and LEO), while assuming a structure as was used in the AED-studies. The constraints are quantified and summarized in Section 4.1. Section 4.2 gives the final results of the optimization routine, after which a comparison is made w.r.t. an aluminum reference structure.

4.1 Constraint Quantification

A top panel of an electronics housing structure was optimized using the method as was described in Chapter 3. The panel was assumed to be simply-supported on all sides and to have four aluminum alloy wedge locks attached to it. PCBs were modeled as dummy masses. The panel's dimensions were given to be 246.5 and 412 mm in x- and y-direction respectively. The panel is shown in Figure 4.1, with the wedge locks running in x-direction over the entire length.

For the proposed missions and dimensions the following set of constraints as a function of the configuration vector x_c and lay-up vector x_l were applied. Note that the radiation-based constraints and the deflection constraints were obtained from a comparison to 2 mm of Al-2024-T3:

$$TID_{\text{GEO}}(x_c) \leq 1.93 \cdot 10^5 \text{ rad(Si)} \tag{4.1a}$$
$$TID_{\text{LEO}}(x_c) \leq 4.46 \cdot 10^4 \text{ rad(Si)} \tag{4.1b}$$
$$NID_{\text{GEO}}(x_c) \leq 5.19 \text{ rad(Si)} \tag{4.1c}$$
$$NID_{\text{LEO}}(x_c) \leq 4.94 \text{ rad(Si)} \tag{4.1d}$$
$$f_n(x_c, x_l) \geq 150 \text{ Hz} \tag{4.1e}$$
$$\delta_{\max}(x_c, x_l) \leq 0.139 \text{ mm} \tag{4.1f}$$
$$RF(x_c, x_l) \geq 1 \quad \text{in } x\text{-, } y\text{- and } z\text{-direction} \tag{4.1g}$$

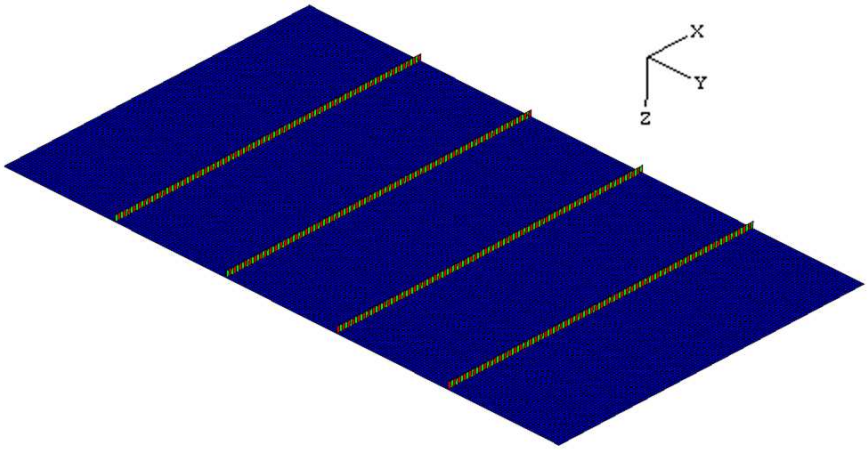

Figure 4.1: The overall configuration of the panel with four wedge locks running over the entire length in x-direction.

The induced shape distortion was introduced as a secondary objective function. It would be possible to manufacture the panels such that after curing the panels would be flat, by using non-flat molds. However, costly molds would have to be manufactured for each individual panel. Therefore, ideally, the panels are flat by design.

Since no specifications were given with respect to the electrical resistivity for neither the AED-studies, nor the SIDER project these requirements were omitted for this practical application. However, the values will be presented for completeness of the analysis.

4.2 Optimization Results

Both objective functions that were discussed in Chapter 3 were applied and are treated in this section.

4.2.1 Minimization of the Mass

For radiation attenuation evaluation the Mulassis particle simulation tool was used. For the proposed orbits 100,000 particles were simulated for all radiation sources and for all stacking configurations. Note that due to the high particle energies the Bragg peak will occur behind the shielding and no significant increase in dose is found for increased depths. Figure 4.2 shows the optimization results for different combinations of laminates, when only considering the four radiation attenuation constraints. When only applying composite material 15 layers were required to achieve an equivalent dose as the Al-2024-T3 reference for both GEO and LEO. In the proton-rich LEO the pure composite configuration would be optimal, but due to the GEO constraints additional carbon fiber plies were required. As a result a mass increase of 19% was found w.r.t. the reference material.

When adding tungsten layers to the laminate a mass reduction of 18% could be achieved. From a radiation point of view there was no indication that the application of either steel or gadolinium for this specific combination of GEO and LEO would be beneficial. The best

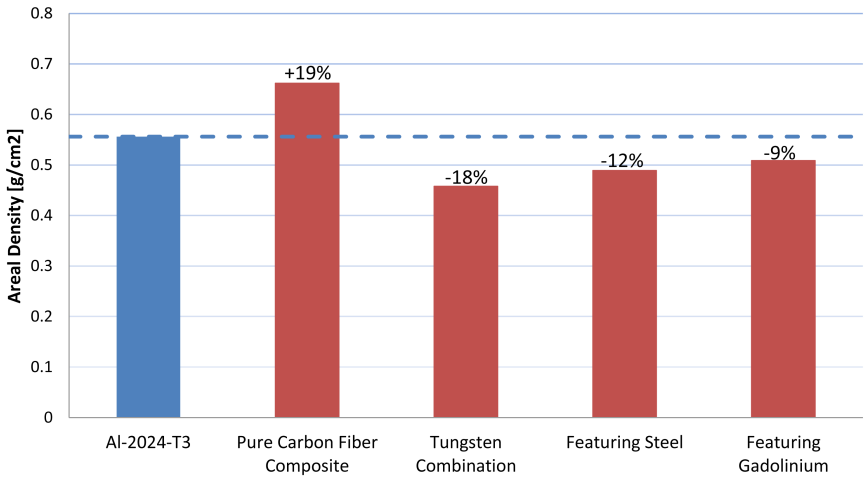

Figure 4.2: Radiation constraint assessment. By applying multiple tungsten foils a mass reduction of 18% can be achieved w.r.t. an Al-2024-T3 reference. The application of steel or gadolinium showed no beneficial effect.

configuration featuring a steel foil was $(5/S^{50}/2/W^{50}/1)$, whereas for the gadolinium case multiple configurations with equal mass were found to be optimum. The most lightweight solution out of all, featuring tungsten foils, was of the sequence $(1/W^{50}/3/W^{50}/2)$. Note that in these configurations the numbers indicate the number of carbon fiber plies, rather than the lay-up angles.

From the structural constraint evaluation it was found that the panel, in its initial configuration featuring alternating 90° and 0° layers, was structurally highly overdimensioned. The natural frequency was found to be 509.16 Hz and for the loading in x-, y- and z-direction the reserve factors were found to be 166.4, 80.8 and 12.5 respectively. The potential energy difference w.r.t. the reference shape was -0.4588 J. For the mass optimization only the GEO and the LEO constraints were active.

4.2.2 Minimization of the Induced Shape Distortions

Since the structure was structurally highly overdimensioned great freedom was gained regarding the fiber lay-up orientation x_l. As such the gradient-based genetic algorithm for the minimization of the induced shape distortions was implemented. By limiting the induced shape distortions smaller forces are required to force the panel into shape during assembly. Furthermore by limiting the deflections no additional costly molds are required for each individual panel.

After investigation of 1,700 unique parents and their individual 72 children, found over a total of 18 generations, the deformation-minimized solution was found to be of the form $(-75/W^{50}/0/60/15/W^{50}/-30/90)$. For the optimized solution a shape distortion of -0.3758 J was found, which equals a reduction of 18.1% w.r.t. the initial guess of -0.4588 J.

Note that due to thermal expansion a shape distortion would even be found for symmetric laminates, w.r.t. the 120 °C reference curing temperature. The energy required to force

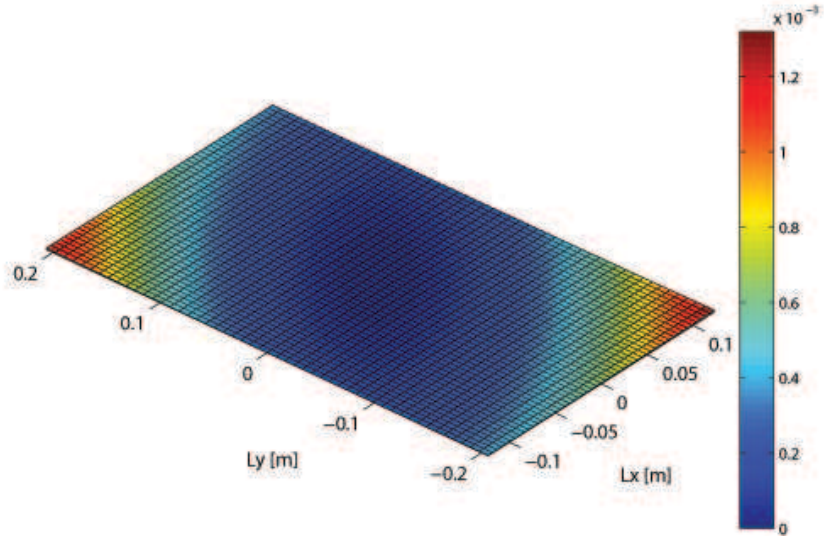

Figure 4.3: Induced shape distortions of the optimized panel.

the panel just into a flat shape was calculated to be 0.0042 J. The obtained post-cure shape is presented in Figure 4.3. Only small deflections of up to 1.3 mm could be identified at the corners.

The natural frequency was calculated to be 518.68 Hz, which is larger than for the initial guess and the Al-2024-T3 reference and significantly larger than the required 150 Hz. The first eigenmode is shown in Figure 4.4. Note that Figure 4.4 is shown with the internal side up, to show the influence of the wedge locks.

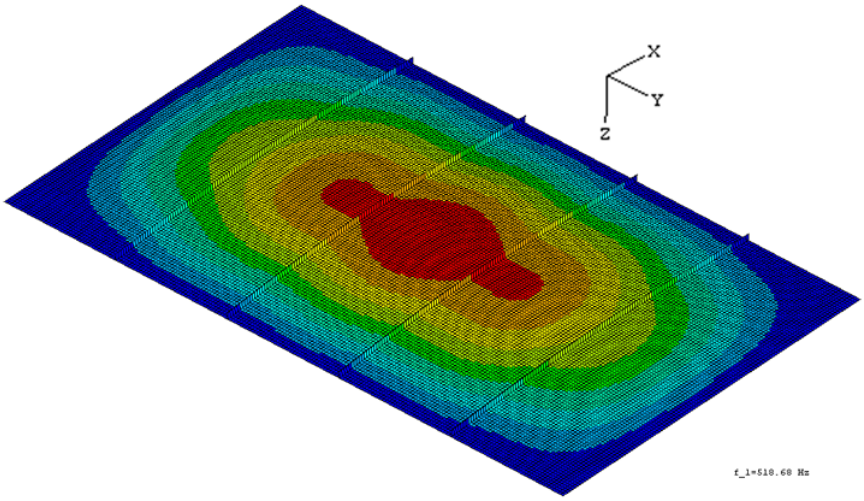

Figure 4.4: First eigenmode of the optimized panel, with a natural frequency of 518.68 Hz.

As a result of the load in z-direction the maximum deflection of the panel is 0.134 mm. This deflection is smaller than was found for the Al-2024-T3 reference (0.139 mm) and only a small fraction of the dimensions in x- and y-direction. The resulting shape is shown in Figure 4.5.

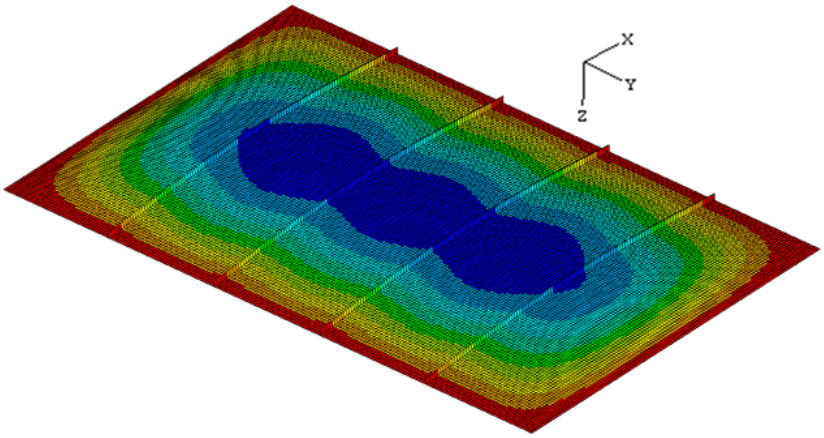

Figure 4.5: Deflections in z-direction as a result of the pressure load for the optimized panel. Maximum deflections of $0.134\,\mathrm{mm}$ were found, indicated in blue. At the simply-supported edges the deflections were zero-valued.

The structural integrity of the panel was assessed too. The in-plane loads N_x and N_y were modeled as line loads of 1021.3 and 3554.2 N/m respectively, as a result of Newton's second law of motion. The out-of-plane load was modeled as a uniform pressure load p_z of $4.7422\,\mathrm{kPa}$.

The response to the pressure load in z-direction is shown in Figure 4.6. It can be seen that the panel, including the aluminum wedge locks, is critical around the edges of the interface between the panel and the wedge locks. However, also for the load in z-direction a reserve factor larger than unity was found (16.2). In Figure 4.6 the values are plotted as $1/RF$, for clarity, such that the critical points are highlighted better.

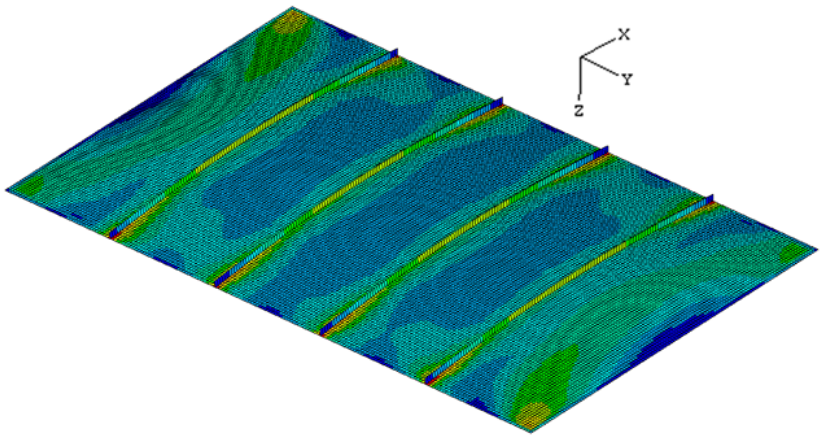

Figure 4.6: The pressure load response for the optimized panel. The critical points, located at the edges of the interface between the wedge locks and the panel, are indicated by red ($1/RF = 0.0616$). Non-critical points are indicated in blue ($1/RF = 0.00353$).

The response to the in-plane loads the stress-strains states were obtained. For the line load in x-direction first ply failure occurred in the second tungsten layer, whereas for

the load in y-direction the first tungsten layer was critical. However, for both loading cases a reserve factor larger than unity was obtained. As such the structural integrity as a response to the in-plane loads was ensured. The reserve factors were found to be 154.0 and 51.0 for respectively N_x and N_y. The values of the reciprocal of the reserve factor ($1/RF$) are plotted for all layers as a function of thickness, for both load cases in Figures 4.7 and 4.8. The angles and the materials of the plies are shown on the left-hand side in Figures 4.7 and 4.8. Letters a and b are layers of respectively M40J/MTM57 composite and tungsten. Clearly, the tungsten, which has the largest value for $1/RF$, is critical in both load cases, reaching its yield stress before failure would occur in the composite plies. It can be noted that for this case no structural constraint were active.

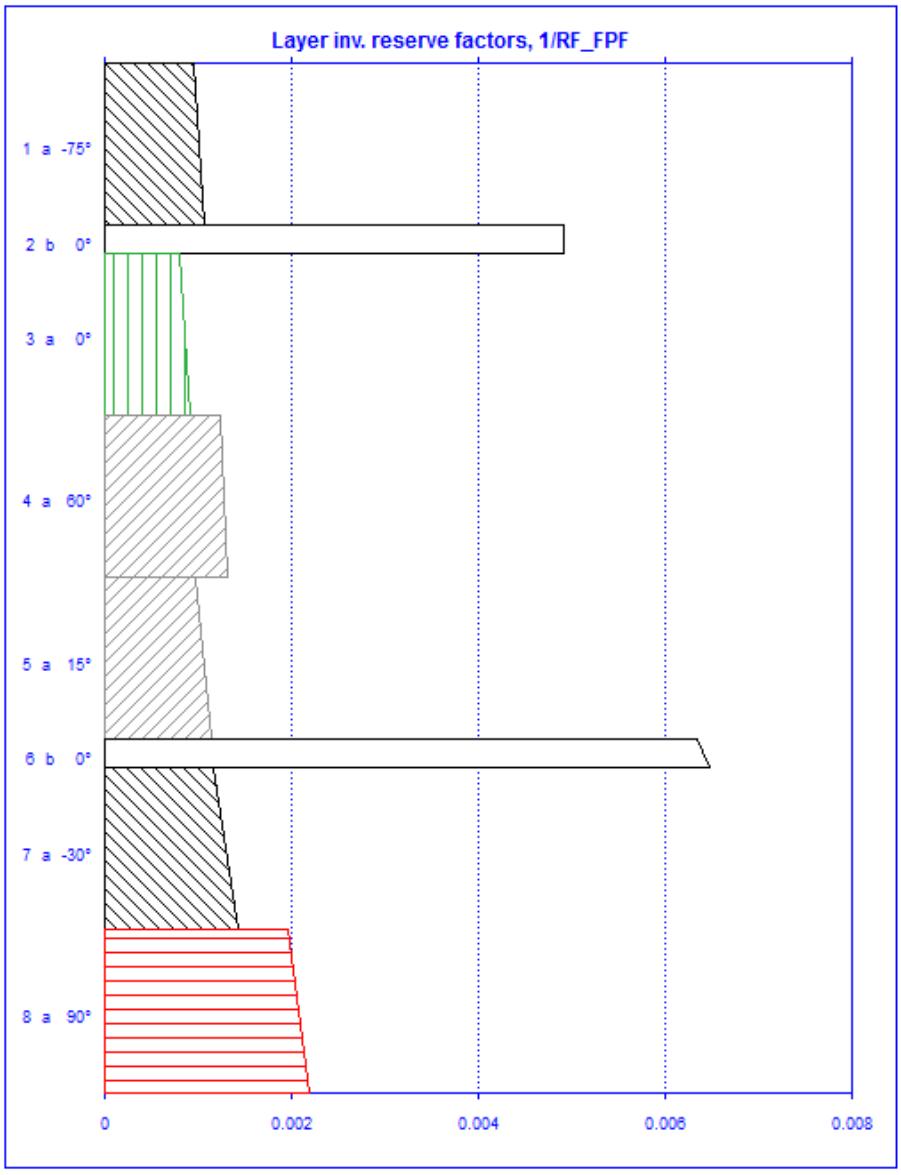

Figure 4.7: The response to the applied line load in x-direction for the optimized panel. For each layer the reciprocal of the reserve factor is plotted as a function of thickness. The tungsten layers are critical.

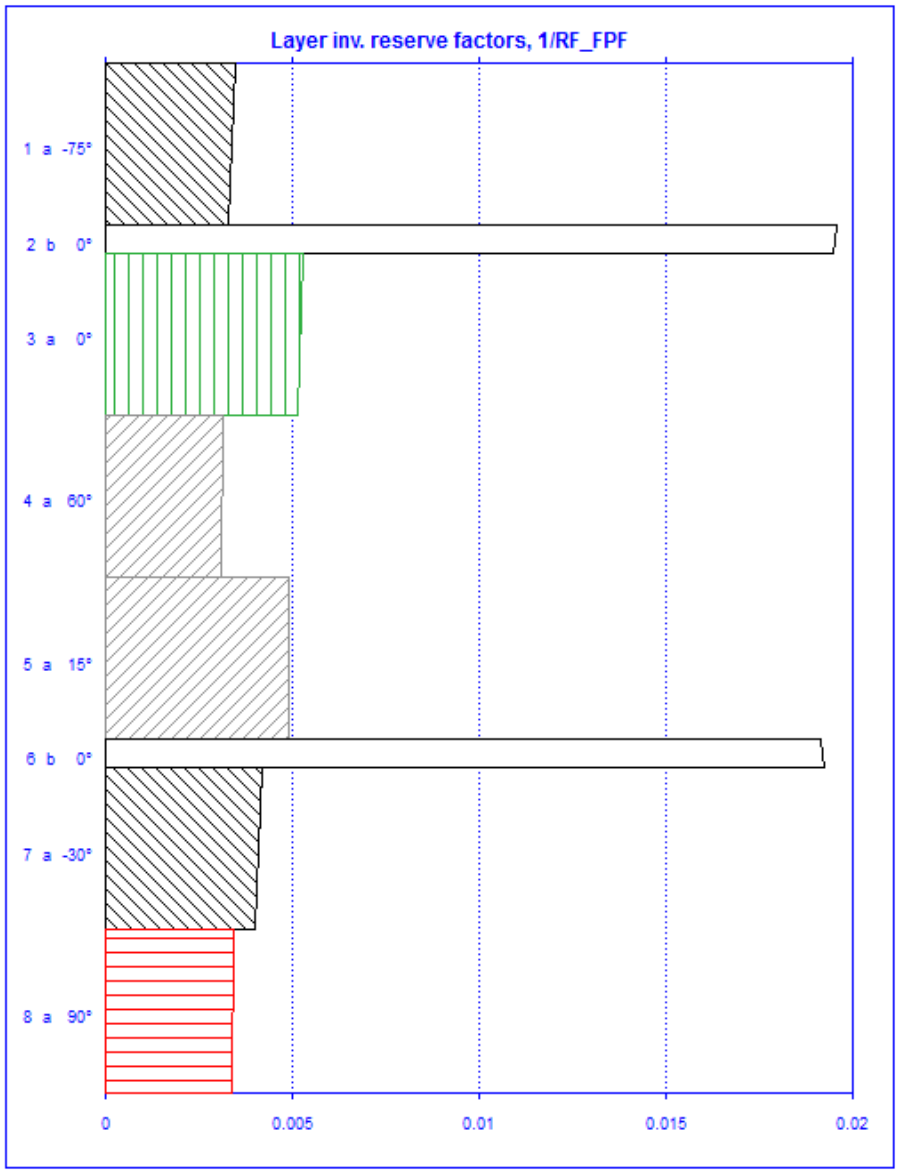

Figure 4.8: The response to the applied line load in y-direction for the optimized panel. Again the tungsten layers are critical.

The electrical resistivity of the panel was also assessed. The resistivity was found to be 994.73 nΩ m in both x- and y-direction. The resistivity in z-direction was much larger: 3.833 TΩ m. In comparison with the Al-2024-T3 reference (58.2 nΩ m) the resistivity was significantly larger in all directions, due to the dielectric properties of the epoxy material. If the electrical resistivity would be set as a hard constraint large quantities of metallic foils would be required.

4.3 Comparison Study

When comparing the optimized laminate with the aluminum it should be noted that different forces were applied to the aluminum as for the laminate, due to the difference in mass. Furthermore for the loading cases a Safety Factor of 1.5 was used for the Al-2024-T3, whereas design standards prescribe a Safety Factor of 2 for composite materials, as were used in the laminate. The optimized configuration was of the form $(-75/W^{50}/0/60/15/W^{50}/-30/90)$.

Parameter	Detail	Al-2024-T3	Composite
Mass m [kg]		0.5647	0.4648
TID [rad(Si)]	GEO	$1.93 \cdot 10^5$	$1.24 \cdot 10^5$
	LEO	$4.46 \cdot 10^4$	$4.46 \cdot 10^4$
NID [rad(Si)]	GEO	5.19	3.21
	LEO	4.94	4.53
Shape distortion $\Delta\Pi$ [J]		0	0.3578
Energy to flatten [J]		0	0.0042
Natural frequency f_n [Hz]		476.60	518.68
Deflection $\delta_{\max}$ [mm]	z	0.139	0.134
Reserve factor RF [−]	x	425.1	154.0
	y	122.2	51.0
	z	34.3	16.2
Electrical resistivity ρ [Ω m]	x	$5.82 \cdot 10^{-8}$	$9.95 \cdot 10^{-7}$
	y	$5.82 \cdot 10^{-8}$	$9.95 \cdot 10^{-7}$
	z	$5.82 \cdot 10^{-8}$	$3.83 \cdot 10^{12}$

Table 4.1: Performance comparison w.r.t. the aluminum reference

For the optimized laminate the mass is reduced by 18% w.r.t. the aluminum. This was achieved, while at the same time reducing the absorbed radiation dose in GEO, for typical diodes. The natural frequency for the laminate was higher than for the aluminum and as such vibrational resonance was avoided. The strength of the optimized laminate is smaller than the aluminum reference, due to the implementation of the tungsten layers for radiation attenuation. The tungsten foils were the critical layers for the different loading cases. However, the reserve factors were still significantly larger than unity, as was required. Part of the difference in strength is explained by the difference in applied Safety Factors.

The second objective function on the shape distortion was minimized for the optimized structure and was reduced by 18% w.r.t. the initial guess. The aluminum does not have any shape distortions, since its reference temperature was taken at the operating temperature. The deflections due to loading in z-direction were smaller than for the aluminum case, whereas the electrical resistivity of the optimized laminate was significantly higher than for the aluminum, due to the large quantity of dielectric resin. The electrical resistivity, however, was not set as a constraint.

Chapter 5

Conclusions and Recommendations

For the application of laminates, consisting of metallic foils and composite materials, the bonding strength is an important prerequisite. Lap shear tests were done for multiple laminates, consisting of tungsten and the composite material. The tungsten was treated with different surface treatments, as were found in the literature. The grit blasting procedure was found to lead to grit embedment where the alumina particles got stuck in the tungsten layer, introducing large amounts of impurities. A Diamond-like Carbon coating treatment was found to result in too large residual stresses, such that the tungsten would fail almost immediately. The last investigated treatment was chemical etching. An adverse relation between etching time and bonding strength was found. This was explained by the presence of unknown impurities around the etched grooves in the foil. As such the chemical etching treatment, with a one-minute etching time, was proposed for future practical applications.

Secondly a design methodology for composite space enclosures was created. A multidisciplinary optimization routine, where the mass was minimized, was proposed. Since radiation attenuation is independent of fiber lay-up angles of the carbon fiber plies these properties were assessed first, using a Mulassis particle simulation tool. Once these constraints were satisfied the induced shape distortions, which are a result of post-cure residual thermal stresses, were minimized by changing the lay-up orientations of the carbon fiber composite plies. The natural frequency was assessed in order to avoid vibrational resonance with other satellite components. Thereafter out-of-plane deflections and the structural integrity were checked for different load cases, resulting from acceleration loads during launch. Moreover the electrical resistivity was assessed in the three principle directions.

For validation of the applied analysis tools multiple tests were performed for induced shape distortions, radiation attenuation, bonding strength and electrical resistivity. The theory was validated and the theoretical models were fine-tuned, based on the test results.

The proposed design methodology was applied to an old design case of an electronics housing structure. Two missions, one LEO and one GEO mission, were proposed. In LEO a large quantity of high energy protons are found, whereas in GEO a electron-rich

environment is traversed. Different combinations of high-Z and low-Z materials were assessed for radiation attenuation purposes, consisting of carbon fiber composites and metallic foils.

The mass of the designed laminate was minimized and compared to a 2 mm Al-2024-T3 reference. The panel, with dimensions of 246.5 and 412 mm in respectively x- and y-direction, was required to attenuate the radiation to the same extent as the aluminum reference would. Furthermore it was required to be able to withstand acceleration loads of 25.6g, 53.3g and 29.3g in respectively x-, y- and z-directions, while at the same time having a natural frequency above 150 Hz to avoid vibrational resonance.

The optimized structure consisted of six M40J/MTM57 carbon fiber composite layers, with two 50 µm thin tungsten foils co-cured, behind respectively the first and the fourth composite layers. The structure was found to be 18% lighter than the aluminum reference and was structurally highly overdimensioned. As such the only active constraints were radiation-based. With the structural overdimensioning large freedom was gained with respect to the fiber lay-up orientations. The minimization routine for the induced shape distortions was applied, resulting in a reduction of strain energy of 18%.

Based on the difficulties experienced with the bonding of the tungsten foils with the carbon fiber prepreg further investigation is proposed. The vast number of parameters regarding the grit blasting procedure and the chemical etching should be parametrically investigated and optimized. In order to improve the etching treatment the influence of the initial abrading should be investigated. Furthermore the exact failure mode of the Diamond-like Carbon coating should be investigated in more depth. An investigation of the DLC thickness on the bonding strength is advised. Also other test methods, such as cracked lap shear tests and pull-off tests are recommended to validate the difference in adhesion for the different surface treatments.

Moreover it should be noted that this optimization routine was applied for a single flat panel only. The investigation of a full 3D model, including the different satellite components is recommended. With the implementation of other components and hinges and holes in the box structure different radiation processes will take place and a large quantity of secondaries will be generated. Furthermore the angular dependence of the attenuation properties of the laminate should be investigated further. Other improvements of the method w.r.t. thermal and electrical conductivity are also advised.

For the validation of the proposed design method other test cases should be assessed. For single-mission electronics housing structures an even larger mass reduction is expected. However, the application of the proposed design method should be validated for shorter or lower-energy missions, where less material is required to shield the electronics. This will have a significant effect on the structural behavior.

References

[1] Garcia, F. and Kurvinen, K., "Radiation Shielding Study of Advanced Data and Power Management Systems (ADPMS) Housing Using Geant4," *2006 IEEE Nuclear Science Symposium Conference*, 2006.

[2] Dodd, P., "Physics-Based Simulation of Single-Event Effects," *IEEE Transactions on Device and Materials Reliability*, Vol. 5, No. 3, September 2005, pp. 343–357.

[3] Bedingfield, K. and Leach, R., "Spacecraft System Failures and Anomalies Attributed to the Natural Space Environment," Tech. Rep. 1390, NASA, 1996.

[4] Katajisto, H. and Brander, T., "Structural and Thermal Analysis of Carbon Composite Electronics Housing of a Satellite," NAFEMS Seminar: Component and System Analysis using Numerical Simulation Techniques, 2005.

[5] Brander, T. and Gantois, K., "CFRP Electronics Housing for a Satellite," *European Conference on Spacecraft Structures, Materials and Mechanical Testing*, 2005.

[6] Jussila, J. and Brander, T., "Manufacture and Assembly of CFRP Electronics Housing," *Proceedings of the European Conference on Spacecraft Structures, Materials and Mechanical Testing*, No. ESA SP-581, May 2005.

[7] de Vriendt, K. and Dayers, L., "AED Qualification Vibration Test Report," Tech. rep., Verhaert, 2004, AED-RP-015-VE.

[8] Anon., "SIDER, Radiation Shielding of Composite Space Enclosures," online, Available at: http://www.sider-project.eu.

[9] Barak, J. and Levinson, J., "Direct Processes in the Energy Deposition of Protons in Silicon," *IEEE Transactions on Nuclear Science*, Vol. 43, No. 6, December 1996, pp. 2820–2826.

[10] Titus, J., "Single-Event Burnout of Power Bipolar Junction Transistors," *IEEE Transactions on Nuclear Science*, Vol. 38, No. 6, December 1991, pp. 1315–1322.

[11] Brews, J. and Allenspach, M., "A Conceptual Model of Single-Event Gate-Rupture in Power MOSFET's," *IEEE Transactions on Nuclear Science*, Vol. 40, No. 6, December 1993, pp. 1959–1966.

[12] Dressendorfer, P., "Basic Mechanisms for the New Millenium," *IEEE Conference on Nuclear and Space Radiation Effects*, Newport Beach, CA, USA, 1998.

[13] Pinyagin, V. and Carapelle, A., "Radiation Shielding of Composite Space Enclosures - Mission Analysis and Requirements," Tech. Rep. SIDER-CSL-D2.1, EU, June 2011.

[14] Van Allen, J., "The Earth and Near Space," *Bulletin of the Atomic Sciences*, Vol. 17, No. 5, May 1961, pp. 218–222.

[15] Van Allen, J. and Ludwig, G., "Observations of High-Intensity Radiation by Satellites 1958 Alpha and Gamma," *Jet Propulsion*, Vol. 28, 1958, pp. 588.

[16] Galland-Kivelson, M. and Bagenal, F., *Encyclopedia of the Solar System*, chap. 28 Planetary Magnetospheres, Academic Press, San Diego, CA, USA, 2007, pp. 519–540.

[17] Anon., "Space Environment," Tech. Rep. ECSS-E-ST-10-04C, European Cooperation for Space Standardization, Noordwijk, The Netherlands, 2008.

[18] Holmes-Siedle, A. and Adams, L., *Handbook of Radiation Effects*, Oxford University Press, 2nd ed., 2002.

[19] Benton, E. and Benton, E., "Space Radiation Dosimetry in Low-Earth Orbit and Beyond," *Nuclear Instruments and Methods in Physics Research Section B: Beam Interactions with Materials and Atoms*, Vol. 184, No. 1-2, 2001, pp. 255–294.

[20] Bourdarie, S. and Xapsos, M., "The Near-Earth Space Radiation Environment," *Nuclear Science, IEEE Transactions on*, Vol. 55, No. 4, aug. 2008, pp. 1810–1832.

[21] Bragg, W. and Kleeman, R., "On the Alpha Particles, and their Loss of Range in Passing through Various Atoms and Molecules," *Philosophical Magazine*, Vol. 6, No. 10, 1905, pp. 318–340.

[22] Shea, M. and Smart, D., "A comparison of Energetic Solar Proton Events during the Declining Phase of Four Solar Cycles," *Advances in Space Research*, Vol. 16, No. 9, 1995, pp. 37–46.

[23] Cole, S. and Hendrix, S., "NASA Spacecraft Observes New Characteristics of Solar Flares," Press Release, 2011, NASA 11-291.

[24] Simpson, J., "Composition and Origin of Cosmic Rays," *NATO ASI Series C: Mathematical and Physical Sciences*, 1983.

[25] Wertz, J. and Larson, W., *Space Mission Analysis and Design*, Kluwer Academic, Dordrecht/Boston/London, 1991.

[26] Mangeret, R. and Carriere, T., *IEEE Transactions on Nuclear Science*, Vol. 43, No. 6, December 1996.

[27] Fan, W. and Drumm, C., *IEEE Transactions on Nuclear Science*, Vol. 43, No. 6, December 1996.

[28] Norman, R. and Badavi, F., "A Deterministic Electron, Photon, Proton and Heavy Ion Radiation Transport Suite for the Study of the Jovian System," *IEEE Aerospace Conference*, 2011.

[29] Thayer, G., "Structural Composite Radiation Shielding Materials," *11th International Symposium on Materials in a Space Environment*, 2009.

[30] Spieth, B. and Qassim, K., *IEEE Transactions on Nuclear Science*, Vol. 45, No. 6, December 1998.

[31] Abusafieh, A. and Trembly, G., "The Development of Lightweight Radiation Shielding Composite for Electronic Enclosures," *44th Internation SAMPE Symposium*, 1999.

[32] Anon., *Standard Test Method for Lap Shear Adhesion for Fiber Reinforced Plastic (FRP) Bonding*, American Society for Testing and Materials, 2008.

[33] Anon., *ACG MTM57 Series Prepreg System*, Advanced Composite Group Ltd., 2011.

[34] Anon., *BR 6747-1 Water-Based Adhesive Bonding Primer System Technical Data Sheet*, Cytec Industries Inc.

[35] Guttmann, W., *Concise Guide to Structural Adhesives*, Reinhold, NY, USA, 2004.

[36] Ebnesajjad, S. and Ebnesajjad, C., *Surface Treatment of Materials for Adhesion Bonding*, William Andrew Publishing, Norwich, NY, USA, 2006.

[37] Lassner, E. and Schubert, W.-D., *Tungsten: Properties, Chemistry, Technology of the Element, Alloys and Chemical Compounds*, Kluwer Academic, 1999.

[38] Anon., *Diamond and Nanocomposite Coatings for Wear Resistant and Low Friction Applications*, Diarc Technology Inc.

[39] Sheeja, D. and Tay, B., "Effect of Film Thickness on the Stress and Adhesion of Diamond-like Carbon Coatings," *Diamond and Related Materials*, Vol. 11, 2002, pp. 1643–1647.

[40] Peckham, D., *Mittal Festschrift on Adhesion Science and Technology*, VSP, 1998.

[41] Prolongo, S. and Rosario, G., "Study of the Effect of Substrate Roughness on Adhesive Joints by SEM Analysis," *Journal for Adhesion Science and Technology*, Vol. 20, No. 5, 2006, pp. 457–470.

[42] Shin, K. and Lee, J., "A Study on the Lap Shear Strength of a Co-Cured Lap Joint," *Journal for Adhesion Science and Technology*, Vol. 14, No. 1, 2000, pp. 123–139.

[43] Freller, H. and Hempel, A., "Influence of Intermediate Layers and Base Materials on Adhesion of Amorphous Carbon and Metal-Carbon Coatings," *Diamond and Related Materials*, Vol. 1, No. 5-6, 1992, pp. 563.

[44] Peng, X. and Clyne, T., "Mechanical Stability of DLC films on Metallic Substrates. Part II - Interfacial Toughness, Debonding and Blistering." *Thin Solid Films*, Vol. 312, 1998, pp. 219–227.

[45] Holbery, J. and Consiglio, R., "Characterisation of Thin Film Adhesion with the Nano-Scratch Tester (NST)," *Adhesion Measurements of Films and Coatings*, edited by K. Mittal, Vol. 2, VSP BV, 2001.

[46] Anon., *Online Materials Information Resource - MatWeb*, 2011, Available at: http://www.matweb.com.

[47] Hutchings, I. M., "Ductile-Brittle Transitions and Wear Maps for the Erosion and Abrasion of Brittle Materials," *Journal of Physics D: Applied Physics*, Vol. 25, 1992, pp. 2–11.

[48] Narita, Y., "Layerwise Optimization for the Maximum Fundamental Frequency of Laminated Composite Plates," *Journal of Sound and Vibration*, , No. 263, 2003, pp. 1005–1016.

[49] Ashby, M., "Multi-Objective Optimization in Material Design and Selection," *Acta Materials*, 2000, pp. 359–369.

[50] Starr, T. and Lovell, D., *Carbon and High Performance Fibers Directory and Databook*, Springer London, 1994.

[51] Schwan, F., "Design of Structure with Composites," *Handbook of Composites*, Chapman and Hall, 2nd ed., 1998.

[52] Grieder, P., *Extensive Air Showers*, Vol. 1, Springer, 2011.

[53] Lin, M., *High Resolution X-Ray Microscopy using Digital Subtraction Angiography for Small Animal Functional Imaging*, Ph.D. thesis, Duke University, 2008.

[54] Shapiro, J., *Radiation Protection - A Guide for Scientists, Regulators and Physicians*, Harvard University Press, 4th ed.

[55] Gilmore, G., *Practical Gamma-Ray Spectroscopy*, John Wiley And Sons Ltd., 2nd ed., 2008.

[56] Krane, K., *Introductory Nuclear Physics*, John Wiley and Sons, Inc., 1988.

[57] Anon., "NIST National Institute of Standards and Technology," Online, 2005, Available at: http://www.nist.gov.

[58] Anon., "Space Product Assurance," Tech. Rep. ECSS-Q-ST-70-53C, European Cooperation for Space Standardization, Noordwijk, The Netherlands, 2008.

[59] Knoll, G., *Radiation Detection and Measurement*, Hamilton Printing Company, 4th ed., 2010.

[60] Bikit, I. and Nemes, T., "Simple Method for Absolute Activity Measurement of 60Co Source," *Nuclear Instruments and Methods in Physics Research Section A: Accelerators, Spectrometers, Detectors and Associated Equipment*, Vol. 603, No. 3, May 2009, pp. 333–336.

[61] Heath, R., "Scintillation Spectrometry, Gamma-Ray Catalogue 1 and 2," Tech. Rep. IDO-16880, USAEC, 1964.

[62] Evans, R., *The Atomic Nucleus*, McGraw Hill Publishing, 1955.

[63] Hubbell, J. H. and Gimm, H. A., "Pair, Triplet and Total Atomic Cross Sections (and Mass Attenuation Coefficients) for 1 MeV-100 GeV Photons in Elements Z = 1 to 100," *Journal of Physical and Chemical Reference Data*, Vol. 9, No. 4, 1980, pp. 1023–1148.

[64] Katajisto, H., "Derivation of Random Load Factors, RLFs," Tech. rep., Componeering Oy, October 2004.

[65] Ontac, S., "Finite Element Analysis of a Micro Satellite Structure under Vibration Induced Loads during Launch," 2008.

[66] Anon., *Series V340 VME Wedge-Tainer Three- or Fivepiece*, APW Electronic Solutions.

[67] Anon., *Payload Flight Equipment Requirements and Guidelines for Safety-Critical Structures*, NASA, 2002, SSP-52005.

[68] Newnan, D., *Fundamentals of Engineering*, Kaplan AEC Education, 2004.

[69] Todoroki, A. and Yoshida, J., "Electrical Resistance Change of Unidirectional CFRP due to Applied Load," *JSME International Journal: Series A*, Vol. 47, No. 3, 2004, pp. 357–364.

[70] Zhang, S.-U. and Kumar, A., "Resistivity of Carbon Fiber Composite Structures," *Journal of Engineering Materials and Technology*, Vol. 133, January 2011.

[71] Montgomery, H., "Method for Measuring Electrical Resistivity of Anisotropic Materials," *Journal of Applied Physics*, Vol. 42, June 1971, pp. 2971–2975.

[72] Logan, B. and Rice, S., "Series for Computing Current Flow in a Rectangular Block," *Journal of Applied Physics*, Vol. 42, 1971, pp. 2975–2980.

[73] Dano, M.-L., "SMA-Induced Deformations in General Unsymmetric Laminates," April 1997.

[74] Jones, R., *Mechanics of Composite Materials*, Scripta Book Company, 1975.

[75] Tsai, S. and Hahn, H., *Introduction to Composite Materials*, Technomic Publishing Company, 1980.

[76] Staab, G., *Laminar Composites*, Butterworth-Heinemann, 1999.

[77] Schlecht, M. and Schulte, M., "Advanced Calculation of the Room-Temperature Shapes of Thin Unsymmetric Composite Laminates," *Composite Structures*, Vol. 32, 1995, pp. 627–633.

[78] Wolff, E., *Introduction to the Dimensional Stability of Composite Materials*, DEStech Publications, Inc., 2004.

[79] Hyer, M. and Jilani, A., "Predicting the Deformation Characteristics of Rectangular Unsymmetrically Laminated Piezoelectric Materials," *Smart Materials and Structures*, Vol. 7, 1998, pp. 784–791.

[80] Hyer, M., "The Room-Temperature Shapes of Four-layer Unsymmetric Cross-Ply Laminates," *Journal of Composite Materials*, Vol. 16, No. 4, 1981, pp. 318–340.

[81] Albert, C., "Spring-In of Angled Thermoset Composite Laminates," September 2001.

[82] Callister Jr., W., *Materials Science and Engineering - An Introduction*, John Wiley And Sons Inc, 7th ed., 2007.

[83] Anon., *M40J Technical Data Sheet*, Toray Carbon Fibers America, Inc., No. CFA-014.

[84] Anon., *ACG MTM57 Series Prepreg System Data Sheet*, Advanced Composites Group, PDS1075/01.10/7.

[85] Rupnowski, P. and Gentz, M., "An Evaluation of the Elastic Properties and Thermal Expansion Coefficients of Medium and High Modulus Graphite Fibers," *Composites Part A: Applied Science and Manufacturing*, Vol. 36, No. 3, March 2005, pp. 327–338.

[86] Totry, E. and Gonzalez, C., "Mechanical Behavior of Composite Materials in Shear: Experiments and Simulations," *Anales de Mecanica de la Fractura*, Vol. 1, No. 26, 2009, pp. 187–192.

[87] Anon., *M40J Functional and Compressive Properties*, Toray Carbon Fibers America, Inc.

Appendix A

Mathematical Model

A.1 Shape Distortions

The mathematical model of the induced shape distortions of general laminates, proposed by Dano and Hyer [73, 79, 80], is an extension of the so-called Classical Lamination Theory (CLT). For a further background on the basic stress-strain relations the reader is referred to standard literature. The out-of-plane deflection w_0 was estimated to be of the form:

$$w^0 = \frac{1}{2}\left(a_1 x^2 + a_2 y^2 + a_3 xy\right) \tag{A.1}$$

The three coefficients a_i were to be determined. The midplane strains ϵ^0 were modeled as a set of complete third-order polynomials, taking into account possible non-linearities, which the standard CLT does not account for. In these equations x, y and z are the respective dimensional coordinates.

$$\begin{aligned}\epsilon_x^0 = {} & c_{00} + c_{10}x + c_{01}y + c_{20}x^2 + c_{11}xy \\ & + c_{02}y^2 + c_{30}x^3 + c_{21}x^2y + c_{12}xy^2 + c_{03}y^3\end{aligned} \tag{A.2}$$

$$\begin{aligned}\epsilon_y^0 = {} & d_{00} + d_{10}x + d_{01}y + d_{20}x^2 + d_{11}xy \\ & + d_{02}y^2 + d_{30}x^3 + d_{21}x^2y + d_{12}xy^2 + d_{03}y^3\end{aligned} \tag{A.3}$$

The in-plane deflections u_0 and v_0 were obtained by integrating the standard strains equations.

$$\frac{\partial u^0}{\partial x} = \epsilon_x^0 - \frac{1}{2}\left(\frac{\partial w^0}{\partial x}\right)^2 \tag{A.4}$$

$$\frac{\partial v^0}{\partial y} = \epsilon_y^0 - \frac{1}{2}\left(\frac{\partial w^0}{\partial y}\right)^2 \tag{A.5}$$

Integration leads to a formulation for in-plane deflections u^0 and v^0. Integrating $\partial u^0/\partial x$ to x introduces an additional term $h(y)$. Analogously a function of x was added for v^0.

$$\begin{aligned} u^0 = {} & c_{00}x + \frac{1}{2}c_{10}x^2 + c_{01}xy + \frac{1}{3}c_{20}x^3 + \frac{1}{2}c_{11}x^2y + c_{02}xy^2 \\ & + \frac{1}{4}c_{30}x^4 + \frac{1}{3}c_{21}x^3y + \frac{1}{2}c_{12}x^2y^2 + c_{03}xy^3 + h(y) \end{aligned} \tag{A.6}$$

$$\begin{aligned} v^0 = {} & d_{00}y + d_{10}xy + \frac{1}{2}d_{01}y^2 + d_{20}x^2y + \frac{1}{2}d_{11}xy^2 + \frac{1}{3}d_{02}y^3 \\ & + d_{30}x^3y + \frac{1}{2}d_{21}x^2y^2 + \frac{1}{3}d_{12}xy^4 + \frac{1}{4}d_{03}y^4 + g(x) \end{aligned} \tag{A.7}$$

The additional terms $h(y)$ and $g(x)$ were taken as third-order polynomials, whereas the first order coefficients of $h(y)$ and $g(x)$ were required to be equal, in order to eliminate rigid body rotation.

$$h(y) = p_1y + p_2y^2 + p_3y^3 \tag{A.8}$$

$$g(x) = p_1x + p_4x^2 + p_5x^3 \tag{A.9}$$

The potential energy Π was given as a function of transformed reduced stiffnesses Q_{ij}, in-plane strains ϵ_x, ϵ_y and shear strain γ_{xy}, temperature difference ΔT and thermal expansion coefficients α_x, α_y and α_{xy}.

$$\begin{aligned} \Pi = \int_{-\frac{L_x}{2}}^{\frac{L_x}{2}} \int_{-\frac{L_y}{2}}^{\frac{L_y}{2}} \int_{-\frac{H}{2}}^{\frac{H}{2}} \Big\{ & \frac{1}{2}Q_{11}\epsilon_x^2 + Q_{12}\epsilon_x\epsilon_y + Q_{16}\gamma_{xy}\epsilon_x + \frac{1}{2}Q_{22}\epsilon_y^2 + Q_{26}\gamma_{xy}\epsilon_y \\ & + \frac{1}{2}Q_{66}\gamma_{xy}^2 - (Q_{11}\alpha_x + Q_{12}\alpha_y + Q_{16}\alpha_{xy})\,\epsilon_x\Delta T \\ & - (Q_{12}\alpha_x + Q_{22}\alpha_y + Q_{26}\alpha_{xy})\,\epsilon_y\Delta T \\ & - (Q_{16}\alpha_x + Q_{26}\alpha_y + Q_{66}\alpha_{xy})\,\gamma_{xy}\Delta T\Big\}\,\mathrm{d}z\mathrm{d}y\mathrm{d}x \end{aligned} \tag{A.10}$$

A total of 28 unknowns were introduced: c_{ij}, d_{ij}, a_i and p_i. In order to find the shape with the minimum potential energy the first derivatives of the potential energy to all unknowns were required to be equal to zero. This set of equations was solved in the Matlab environment. Stability was assessed by checking the positive definiteness of the second derivatives. If and only if all eigenvalues of the Hessian matrix were positive stability was achieved and a minimum was found.

A.2 Electrical Resistivity

In accordance with the Van der Pauw method four resistance measurements were done for both in-plane principle directions and averaged. The obtained resistances R_1 and R_2 are combined into one parameter: The resistance ratio R_2/R_1. With the resistance ratio the equivalent isotropic length ratio l_2/l_1 was obtained from Figure A.1. The equivalent isotropic dimensions are calculated such that the resistivity is equal in all directions and as such an apparent isotropic material is obtained.

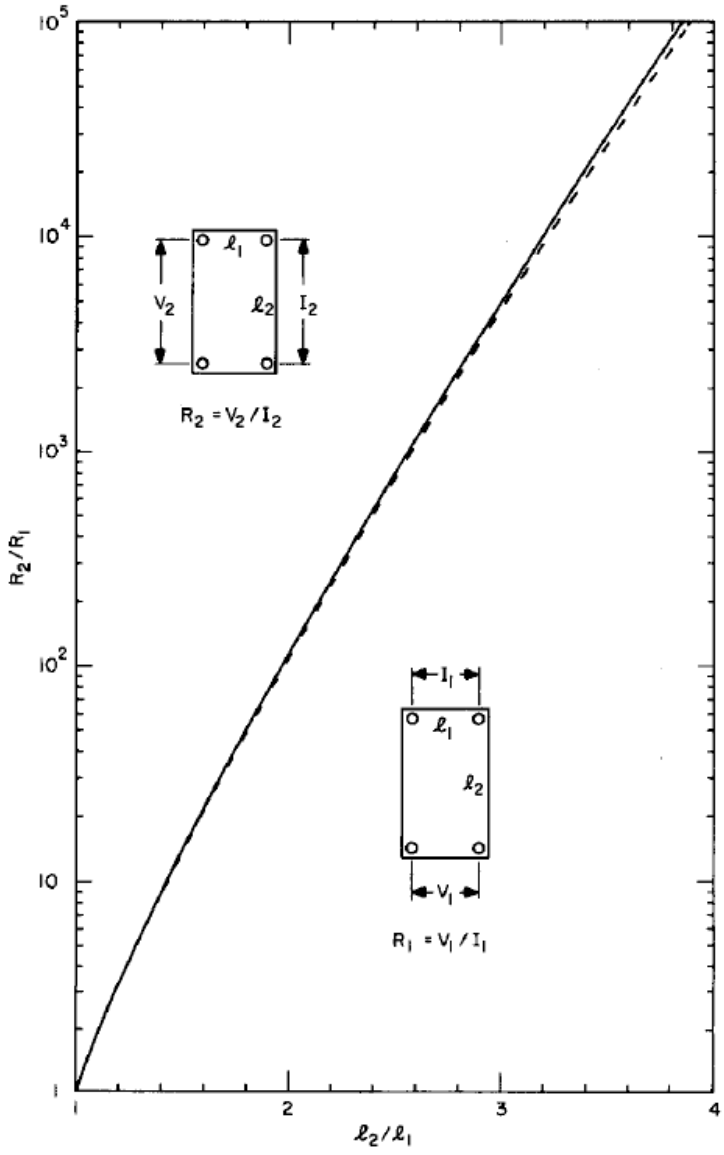

Figure A.1: Resistance ratio versus length sample dimension ratio. Solid line is for a thin sample; dashed line for a thick sample. After [71]

Based on the equivalent isotropic length ratio the normalized effective thickness $E/\sqrt{l_1 l_2}$ was obtained from Figure A.2. Since the equivalent isotropic length l_3 is much bigger

than $\sqrt{l_1 l_2}$, due to the large through-thickness resistivity, the curves were assumed to already be in the linear regime, for $l_3/\sqrt{l_1 l_2} > 3$.

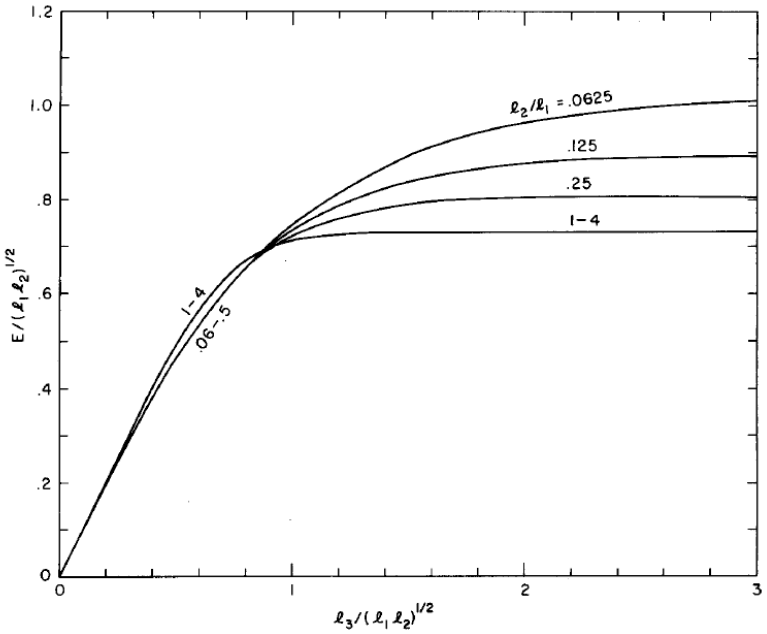

Figure A.2: Normalized effective thickness versus normalized sample thickness for various ratios of sample dimensions. After [71]

The equivalent isotropic resistivity ρ is given by the following equation:

$$\rho = HER_1 \tag{A.11}$$

In this equation H is another term, which is dependent on the equivalent isotropic length ratio [72]:

$$q = e^{-\pi \frac{l_2}{l_1}} \tag{A.12}$$

$$(cM)_0 = \ln \frac{1 + 2q + 2q^4 + 2q^9 + \cdots}{1 - 2q + 2q^4 - 2q^9 + \cdots} \tag{A.13}$$

$$H = \frac{\pi}{4(cM)_0} \tag{A.14}$$

A set of eight equations and eight unknowns is achieved, including Equations A.11, A.15, A.16, A.17, A.18 and A.19. The primed values are the true anisotropic values, whereas the unprimed variables represent the isotropic equivalents.

$$l_i = l_i' \sqrt{\frac{\rho_i}{\rho}} \text{ for } i = 1, 2, 3 \tag{A.15}$$

$$\rho^3 = \rho_1 \rho_2 \rho_3 \tag{A.16}$$

In order to take into account the sample thickness the following equations are needed.

$$\frac{l_3}{\sqrt{l_1 l_2}} = \frac{\sqrt{\rho_3}}{(\rho_1 \rho_2)^{1/4}} \frac{l_3'}{\sqrt{l_1' l_2'}} \tag{A.17}$$

$$\frac{E'}{\sqrt{l_1' l_2'}} = \frac{(\rho_1 \rho_2)^{1/4}}{\sqrt{\rho_3}} \frac{E}{\sqrt{l_1 l_2}} \tag{A.18}$$

Equation A.19 could be substituted directly into the equations, but the solver was found to converge more rapidly when this relation, inserting the obtained value for the length ratio l_2/l_1, was set as one of the to be solved equations:

$$l_2 = l_1 \frac{l_2}{l_1} \tag{A.19}$$

The set of eight equations is solved numerically using a Matlab routine for eight unknowns: Electrical resistivities in three orthogonal directions (ρ_1, ρ_2, ρ_3), equivalent isotropic dimensions (l_1, l_2, l_3), the equivalent isotropic resistivity (ρ) and the effective thickness (E'). The initial guesses for the unknowns, inserted into the solver, are equal to the theoretical expected values.

Appendix B

Material Data

For the modeling of the composite laminate the following material data was implemented in the models.

B.1 Radiation Properties

For photon radiation modeling the elemental mass fractions were required. The elemental mass fractions for each compound were multiplied with the compound mass fraction (CMF). The different contributions were summed to obtain the total elemental mass fractions (EMF) for the composite material. The composite was assumed to consist of 68% carbon fiber and 32% matrix material. For the input of the Mulassis tool the elemental stoichiometric fractions (ESF) were required. The stoichiometric fractions were obtained by dividing the mass fractions by their respective atomic weights and were thereafter normalized. For the different compounds individually the ESF was the relative number of atoms of the specific element in the considered molecule. The different elemental fractions are tabulated in Table B.1.

For the proton radiation validation the metallic foils were found to be nonideal, due to grit embedment of the aluminum oxide in the tungsten and the abrading of steel material. The abrasion was accounted for by reducing the thickness from 50 to 48.06 µm. The effective thickness of the tungsten foil was calculated to be 98.35 µm, after introduction of the aluminum oxide ($\rho = 3.96\,\mathrm{gcm}^{-3}$). Table B.2 shows the materials as they were modeled in the Mulassis tool. In the optimization process ideal thicknesses were assumed and the tungsten and gadolinium foils were modeled as the pure elements. The metallic alloys, such as the steel and the aluminum, were modeled by their respective elemental composition.

Material	CMF	Element	EMF	ESF
C	0.68	C	1.000	1.000
$C_{18}H_{20}O_3$	0.22	H	0.071	0.488
		C	0.760	0.439
		O	0.169	0.073
$C_{40}H_{48}O_7$	0.10	H	0.076	0.505
		C	0.750	0.421
		O	0.175	0.074
Total composite	1.00	H	0.023	0.223
		C	0.922	0.744
		O	0.055	0.033

Table B.1: Elemental composite properties.

Material	Element	EMF	ESF
Tungsten (ideal)	W	1.000	1.000
Tungsten (nonideal)	W	0.834	0.359
	Al	0.088	0.257
	O	0.078	0.385
Steel 1.4310	Fe	0.722	0.705
	Cr	0.175	0.184
	Ni	0.078	0.074
	Si	0.010	0.019
	Mn	0.010	0.010
	Mo	0.004	0.002
	C	0.001	0.005
	N	0.001	0.002
Al-2024-T3	Al	0.927	0.957
	Cu	0.044	0.019
	Mg	0.015	0.017
	Mn	0.006	0.003
	Fe	0.003	0.001
	Zn	0.002	0.001
	Ti	0.001	0.001
Gadolinium	Gd	1.000	1.000

Table B.2: Elemental metallic foil properties.

B.2 Structural Properties

The structural behavior of the composite material was based on the following material properties [83–87]. The composite material behavior depends on the individual contributions of the fibers and the resin, given in Table B.3.

The lamina properties are calculated via the rules of mixtures and are given in Table B.4.

The ultimate failure behavior of the composite material was given by the manufacturer.

Material Property	M40J		MTM57
Young's Modulus, E (l, t) [GPa]	377	13.4	3.35
Shear Modulus, G (lt, tt) [GPa]	20.8	3.9	1.24
Diameter, d [mm]	0.005		-
Density, ρ [g cm^{-3}]	1.77		1.22
Poisson Ratio, ν (lt, tt) [-]	0.27	0.72	0.35
Thermal Expansion, α (l, t) [10^{-6} K^{-1}]	-0.83	6.9	48
Electrical Conductivity, σ [S m^{-1}]	10^5		10^{-11}

Table B.3: Input material properties. Terms l and t indicate longitudinal and transverse direction respectively.

Material Property	M40J/MTM57	
Fiber Volume Fraction, $\hat{v}_f$ [-]	0.5943	
Fiber Mass Fraction, $\hat{m}_f$ [-]	0.68	
Fiber Areal Density, $\bar{\rho}_f$ [g m^{-2}]	300	
Density, ρ [g cm^{-3}]	1.547	
Thickness, t [mm]	0.28521	
Young's Modulus, E (x,y) [GPa]	225.41	7.60
Shear Modulus, G (12,23) [GPa]	4.95	2.46
Poisson Ratio, ν (12,23) [–]	0.30	0.54
Thermal Expansion, α (x,y) [10^{-6} K^{-1}]	-0.54	30.42
Electrical Conductivity, σ (x,y) [S m^{-1}]	$5.94 \cdot 10^4$	$2.46 \cdot 10^{-11}$

Table B.4: Calculated composite properties.

Since for the structural modeling only First-Failure is considered the First-Failure stresses and strains were estimated from these given values, given in Table B.5.

Direction	σ_{FF} [MPa]	ϵ_{FF} [%]	σ_{ult} [MPa]	ϵ_{ult} [%]
X_t	2300	1.02	2450	1.1
X_c	1200	0.53	1270	0.6
Y_t	50	0.66	53	0.7
Y_c	230	3.03	250	3.5
Shear	90	1.82	100	2.1

Table B.5: First-failure (FF) and ultimate (ult) stresses and strains. The First-failure stresses were estimated from the ultimate stresses and the strains were calculated from the estimated FF stresses.

The structural modeling of the metals is more straight-forward, since the materials were assumed to be homogeneous and isotropic. The metal data is given in Table B.6 [46]. The yield stresses for the metals were explicitly given, as shown in Table B.7.

Material Property	Tungsten	Al-2024-T3	Al-6061-T6
Young's Modulus, E [GPa]	400	73.1	68.9
Shear Modulus, G [GPa]	156	27.5	26
Density, ρ [g cm^{-3}]	19.3	2.78	2.70
Poisson Ratio, ν [–]	0.282	0.330	0.325
Thermal Expansion, α [10^{-6} K^{-1}]	4.4	22.9	23.6
Electrical Conductivity, σ [S m^{-1}]	$1.77 \cdot 10^7$	$1.72 \cdot 10^7$	$2.51 \cdot 10^7$

Table B.6: Metal material properties

Material Property	Tungsten	Al-2024-T3	Al-6061-T6
$X_t = X_c$	750	345	276
$Y_t = Y_c$	750	345	276
Shear	400	283	200

Table B.7: Metal first failure properties